MEASUREMENT OF ULTRAFAST RELAXATION TIMES IN SEMICONDUCTORS USING PICOSECOND PULSES

by

Arthur Lee Smirl

A Dissertation Submitted to the Faculty of the

COMMITTEE ON OPTICAL SCIENCES (GRADUATE)

In Partial Fulfillment of the Requirements
For the Degree of

DOCTOR OF PHILOSOPHY

In the Graduate College

THE UNIVERSITY OF ARIZONA

1 9 7 5

THE UNIVERSITY OF ARIZONA

GRADUATE COLLEGE

I hereby recommend that this dissertation prepared under my direction by Arthur Lee Smirl

entitled MEASUREMENT OF ULTRAFAST RELAXATION TIMES IN SEMICONDUCTORS USING PICOSECOND PULSES

be accepted as fulfilling the dissertation requirement of the degree of Doctor of Philosophy

W. Scully — Nov. 14, 1975
Dissertation Director — Date

After inspection of the final copy of the dissertation, the following members of the Final Examination Committee concur in its approval and recommend its acceptance:*

Frederick A. Hopf — Nov 14 '75
Richard L. Sproull — Nov 14, 75

*This approval and acceptance is contingent on the candidate's adequate performance and defense of this dissertation at the final oral examination. The inclusion of this sheet bound into the library copy of the dissertation is evidence of satisfactory performance at the final examination.

STATEMENT BY AUTHOR

This dissertation has been submitted in partial fulfillment of requirements for an advanced degree at The University of Arizona and is deposited in the University Library to be made available to borrowers under rules of the Library.

Brief quotations from this dissertation are allowable without special permission, provided that accurate acknowledgment of source is made. Requests for permission for extended quotation from or reproduction of this manuscript in whole or in part may be granted by the head of the major department or the Dean of the Graduate College when in his judgment the proposed use of the material is in the interests of scholarship. In all other instances, however, permission must be obtained from the author.

SIGNED: Arthur L. Smith

PREFACE

John C. Matter and I began our efforts to measure the nonlinear, nonequilibrium optical properties of semiconductors on a picosecond time scale in the summer of 1972. Our experimental efforts during the past three years may be broken into three distinct segments: the attempts to obtain data with the existing equipment; the redesign of the existing Nd:glass laser system in order to improve its reliability; and the first direct measurement of the intraband temperature relaxation of electrons in the conduction band of a semiconductor.

During the first year, we attempted to obtain data utilizing the already existing laser system. The acquisition of data during this period was exceedingly slow and difficult due to the lack of reliability of the mode-locked Nd:glass laser. The behavior that limited the data gathering was the presence of multiple pulse trains during a single excitation of the lasing medium and the completely random nature of the pulse train envelope.

As a result of these difficulties, we devoted approximately the next year to redesigning our laser system. During this time, we studied the literature and consulted with recognized experts searching for clues to reliable laser performance. We implemented each suggestion made to us. At various times we modified the existing laser system, designed and constructed our own system, and finally purchased a commercial laser head and power supply from Korad. All of this effort consumed

much time, effort, and money with little success. Then, in desperation, we changed our laser glass from Owens-Illinois ED2 to Owens-Illinois ED2.3S. The laser performance improved.

During the final 12 months, John Matter and I acquired most of the experimental data presented in this work. In addition, we verified and numerically evaluated the theoretical equations to obtain a comparison between the proposed model and experiment.

The success of this rather ambitious project is due to the efforts of a great many people. I am very much indebted to my advisor, Professor Marlan O. Scully, who initiated this project in 1970 with a belief that intraband relaxation times in semiconductors could be directly measured using ultrashort pulses from mode-locked lasers. I am also grateful to Dr. Hugo Weichel, Dr. Sastry Pappu, and Dr. Chandler Kennedy for designing, assembling, and operating the original laser system and for their efforts in obtaining preliminary data.

I would like to express my sincere gratitude to Dr. Ahmet Elci for his tireless effort in performing the myriad calculations associated with the theoretical evaluation of this project. Most of the calculations presented in this work were originally performed by him. Much of my knowledge of solid state physics was acquired while verifying his calculations.

I wish to thank Dr. C. V. Shank and Dr. D. H. Auston for providing us with preprints of their results, which we received during the course of these measurements, and Dr. D. Von der Linde for allowing me to visit his laboratory during the redesign of our system.

I am also indebted to Dr. F. A. Hopf for the things I learned from his courses and for his substantial contributions to my theoretical understanding of this problem and to Dr. R. L. Shoemaker for his experimental assistance. I wish to thank Dr. Murray Sargent and Professor S. F. Jacobs not only for the things I learned from their courses but for their encouragement and advice.

Also my sincerest thanks to Mr. John Poulos for providing the excellent dielectric coatings for the mirrors and optical filters used in these experiments and to Mr. Richard Sumner for the delicate grinding and polishing of the semiconductor samples.

A special word of thanks to Dr. John C. Matter who patiently shared this endeavor with me.

I am especially grateful to my wife Loraine without whose support this undertaking could not have been completed.

This project was supported in part by the National Science Foundation and the U. S. Air Force, Space and Missile Systems Organization.

TABLE OF CONTENTS

TABLE OF CONTENTS--Continued

LIST OF ILLUSTRATIONS

LIST OF ILLUSTRATIONS--Continued

LIST OF ILLUSTRATIONS--Continued

LIST OF TABLES

ABSTRACT

Measurements, on a picosecond time scale, of the nonlinear, nonequilibrium optical (1.06 μm) properties of single crystal germanium are presented. The transmission of germanium as a function of incident pulse energy is measured for two sample temperatures, 105 K and 297 K. At both sample temperatures, the germanium exhibits a condition of enhanced transmission for large pulse energies (between 10^{13} and 10^{14} quanta). The optical pulses, obtained from a mode-locked Nd:glass laser, are 5 to 10 psec in duration and are focused on the sample to a spot with a diameter of approximately 480 μm. The sample has a thickness of 5.5 μm.

The behavior of the single pulse transmission of germanium as a function of pulse energy is accounted for by direct interband transitions followed by the heating of the electron distributions. For energies less than 10^{13} quanta (sample interaction volume is approximately 10^{-6} cm^3), the transmission follows Beer's law. For intermediate pulse energies of 10^{13} to 10^{14} quanta, the transmission rises due to the saturation of the available optically coupled electronic states by means of direct absorption. Further increase in the transmission, for energies larger than 10^{14} quanta, is prevented as the electrons are heated and removed from these states by means of nonradiative plasma recombination and free carrier absorption. Similar arguments apply for the holes in the valence band.

In addition, the relative transmission of a probe pulse as a function of time delay after an energetic excitation pulse is measured for three different excitation pulse energies and two sample temperatures. The probe transmission increases with time delay for delays up to approximately 100 psec, after which time it slowly decreases. The magnitude of the increase in probe transmission is greater for a sample temperature of 105 K than for 297 K, and the magnitude increases with increasing excitation energy.

The rise and fall observed in the probe pulse transmission is due to the temperature relaxation of the electron and hole distributions by means of phonon emission. The probe pulse transmission initially increases as the electrons, heated by the excitation pulse, cool and fill the electronic states needed for absorption. Because the states that are optically coupled lie at some energy above the bottom of the conduction band, further cooling of the electron distribution will remove the electrons from these states and will result in a decrease in transmission.

CHAPTER 1

INTRODUCTION

Intense ultrashort optical pulses having durations of a few picoseconds and peak powers of many gigawatts can be readily generated by mode-locking lasers (Smith, Duguay, and Ippen, 1974, and Von der Linde, 1973). The extremely high power and short duration of pulses from these lasers make possible the study of nonlinear interactions of light with matter on a picosecond time scale (Alfano and Shapiro, 1975). In this work we wish to employ ultrashort pulses from a mode-locked Nd:glass laser to study the ultrafast relaxation processes of nonequilibrium carriers in semiconductors. The method we employ was first used on a picosecond time scale by Shelton and Armstrong (1967). First, the semiconductor sample is irradiated by a powerful light pulse of suitable frequency (excitation pulse), which generates a large density of excited carriers. Then a short time later, a second, less powerful, pulse (probe pulse) traverses the sample, and the decay of the nonequilibrium state is monitored by measuring the transmission of the probe pulse at various time delays after the excitation pulse.

Recently, the nonlinear, nonequilibrium properties of solid state plasmas in germanium have been studied employing these methods. In the first of these (Kennedy et al., 1974), we measured the nonlinear optical transmission of germanium as a function of picosecond pulse energy at 1.06 μm. In a second experiment, we monitored the transmission

of a probe pulse as a function of time delay between a strong excitation pulse and the weak probe pulse, and we observed an increase in the probe pulse transmission for delays of a few picoseconds. For some, as yet not completely determined, reason, we did not initially observe an increase in transmission for longer delays (a plausible explanation is, however, offered in Chapter 5). Auston and Shank (1974) performed similar excitation-probe measurements in reflection using ellipsometric techniques. They observed a change in refractive index for probe delays up to 50 psec. Shortly thereafter, Shank and Auston (1975) extended the excitation-probe transmission measurements to longer time delays. In addition to the sharp spike at zero delay observed by Kennedy et al. (1974), they observed an increase in probe transmission for delays as long as 100 psec. In view of these new measurements, they correctly interpreted the sharp spike at zero time delay as light scattering of the excitation beam into the probe beam due to an index grating formed by the interference of the two beams. Independently, we (Smirl et al., 1975) obtained data that confirmed the functional dependence of probe transmission on the time delay between excitation pulse and probe pulse observed by Shank and Auston (1975), although our results differed quantitatively in several respects. In addition, we measured the dependence of the relative probe pulse transmission as a function of time delay after an excitation pulse on sample temperature and excitation pulse energy.

In this work, we report the results of our studies of the nonlinear, nonequilibrium properties of germanium under irradiation by

intense, ultrashort optical pulses. In Chapter 2, we describe the experimental apparatus used in these studies and its operation. In Chapter 3, we present the results of the experimental measurements, and in Chapter 4, we propose a theoretical model that accounts for the observed behavior of germanium while interacting with picosecond pulses. Finally, in Chapter 5, we compare the results predicted by the model with those obtained from experiment.

CHAPTER 2

EXPERIMENTAL APPARATUS

The equipment associated with excitation-probe experiments of the type described in the Introduction is by now standard. No attempt will be made here to describe in detail the principles of operation of these devices; rather, in each case a single reference to the available literature describing the device will be made. Since each component of the system may vary in design from experimenter to experimenter and from manufacturer to manufacturer, care will be taken to completely identify the components employed in these experiments.

The discussion of the apparatus (Fig. 1) is easily divided into four parts: (1) the Nd:glass laser, (2) the electro-optic shutter, (3) the pulse splitting and delay optics, and (4) the pulse monitoring electronics. The laser generates a mode-locked train of approximately 100 widely separated pulses. The electro-optic shutter extracts a single pulse from this train of pulses. This pulse is then divided into two parts, and one part (probe pulse) is delayed with respect to the other (excitation pulse) by the pulse splitting and delay optics. Both parts of the pulse are then focused on a common area of a semiconductor sample mounted in a dewar. The transmitted energies of the two pulses are measured by photodiode circuits of a unique design.

In order to provide a single rigid platform, the entire system, with the exception of the laser power supply and oscilloscopes, is

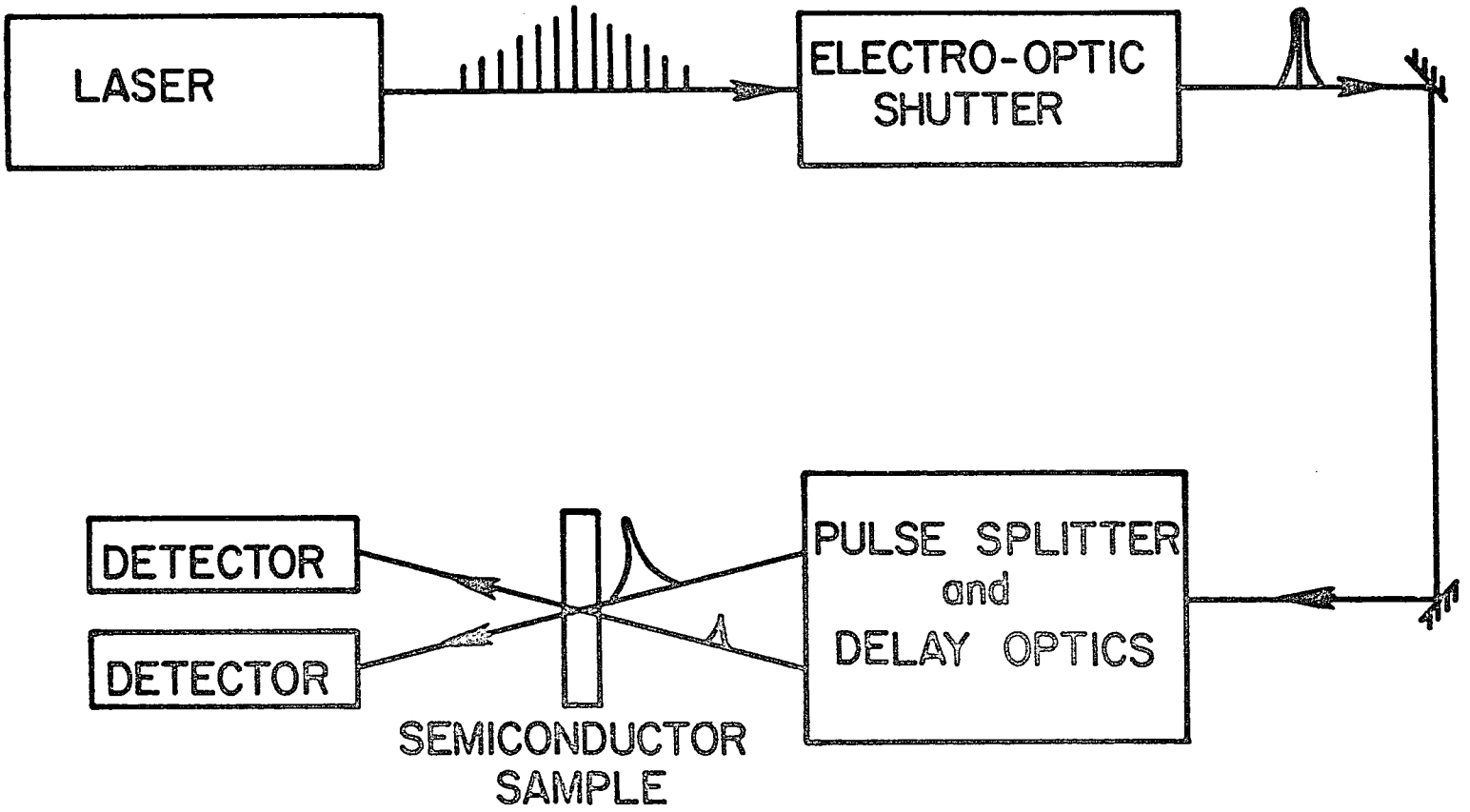

Fig. 1. Block Diagram of Experimental Arrangement for Measuring Ultrashort Relaxation Times in Semiconductors.

mounted on a 4 ft x 8 ft granite slab. The remainder of this chapter describes each component of the system in more detail.

The Nd:glass Laser

The production of very short optical pulses by mode-locking requires a laser system with active medium that provides a large gain bandwidth for light amplification. To obtain light pulses of duration τ, a frequency bandwidth of $\Delta\nu \simeq 1/\tau$ is needed. Nd^{3+}:glass, with a fluorescent bandwidth of 2.7×10^{12} Hz, has the potential of producing pulses as short as 0.3 psec. In practice, pulses between 5 and 15 psec duration are obtained. This deviation from the theoretically calculated pulse width is caused by the broadening of short pulses in a dispersive and nonlinear medium and by spectral narrowing due to preferential amplification of frequency components close to the gain maximum. In fact, pulse widths would be wider than those observed if it were not for the pulse shortening effects of the nonlinear saturable absorber that is used to passively mode lock the laser. For a discussion of the basic principles of mode-locking and the production of ultra-short laser pulses, the reader is referred to Von der Linde (1973).

The mode-locked output from the Nd:glass laser system employed in these experiments consists of a series of approximately 100 pulses separated one from the other by approximately 8 nsec. Each pulse is 5 to 10 psec in duration and has an energy of 0.1 mJ at a wavelength of 1.06 μm. The laser produces single well mode-locked pulse trains on more than 70% of its firings. A brief description of the laser hardware follows.

The active lasing medium, a Brewster-cut Owens-Illinois ED2.3S Nd:glass rod approximately 19 cm long and 6.4 mm in diameter, is housed in a Korad K1 laser head. The glass rod is pumped by a helical xenon flash lamp with an arc length of 28 in. A high voltage, symmetrically shaped pulse from a 10 kV power supply is used to ionize the xenon gas. The high voltage pulse is 0.5 msec in duration, and it typically delivers an energy of 600 J at 4.5 kV. Both flash lamp and glass rod are cooled by circulating water maintained at room temperature. The power supply consists of a 60 μF capacitor bank plus pulse shaping electronics. The flash lamp and power supply are fired approximately once per minute.

The laser oscillator cavity is 120 cm long with a spherical mirror of radius 2.5 m with a reflectivity of 99.7% at 1.06 μm at one end and a flat mirror with a reflectivity of 27% at the output end. The laser is mode-locked by placing a 1-mm-thick cell containing a 10:1 solution of dichloroethane and Eastman Q-switch solution A9860 in contact with the output mirror. The output mirror forms one face of the dye cell. Thus it must be resistant to the solvent dichloroethane as well as withstand the high power levels of the optical pulses. The mode-locking dye is replenished after each laser firing by syphoning fresh dye solution from a reservoir with a hypodermic needle as shown in Fig. 2.

The Electro-optic Shutter

The selection of a single pulse from the mode-locked train of pulses is achieved by an electro-optic shutter system first employed

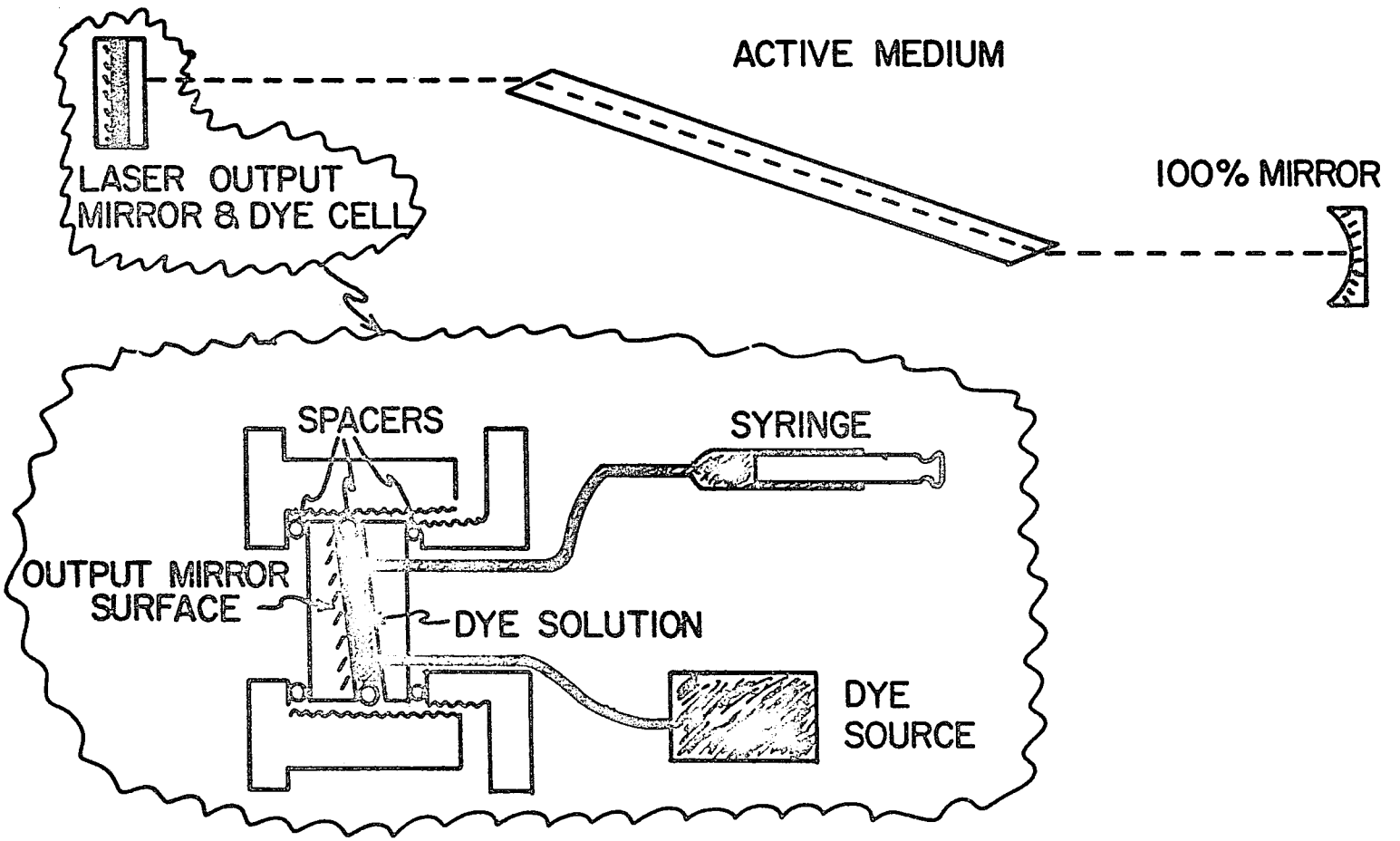

Fig. 2. Schematic of Laser Head and Dye Cell Arrangement.

by Von der Linde, Bernechker, and Laubereau (1970). A schematic diagram of this system is shown in Fig. 3. A 10-mm-aperture Pockels cell (Isomet model 416B with copper tab electrodes) consisting of a heavily deuterated KD*P crystal is placed between two crossed Glan polarizers (Karl Lambrecht model GLQS-10) designed to withstand more than 100 MW cm^{-2} of power. The polarizers are arranged such that when there is no voltage applied to the Pockels cell, there is no light transmitted by the second polarizer; instead, the light is focused between the electrodes of a spark gap. When the beam energy is high enough to cause breakdown of the gas in the spark gap, a high voltage pulse is transmitted along the triaxial cable L_2 to the Pockels cell, causing a 90° rotation of the plane of polarization of the light. As a result, a portion of the beam passes through the second polarizer. The duration of the voltage pulse is proportional to the length of the cable L1. This length is chosen to ensure that only one pulse is transmitted by the shutter. To avoid reflections of the high voltage pulse, the length of line L3 and the resistance R3 are chosen so that the Pockels cell and spark gap assembly are impedance matched to the coaxial cable. The length of cable L2 controls the time delay between the breakdown of the spark gap and the application of the voltage pulse to the Pockels cell. The design of the spark gap, spark gap power supply, and electro-optic shutter used in these experiments is described in detail by Weichel (1972).

A portion of the beam that is focused between the electrodes of the spark gap is deflected by a beam splitter to a fast

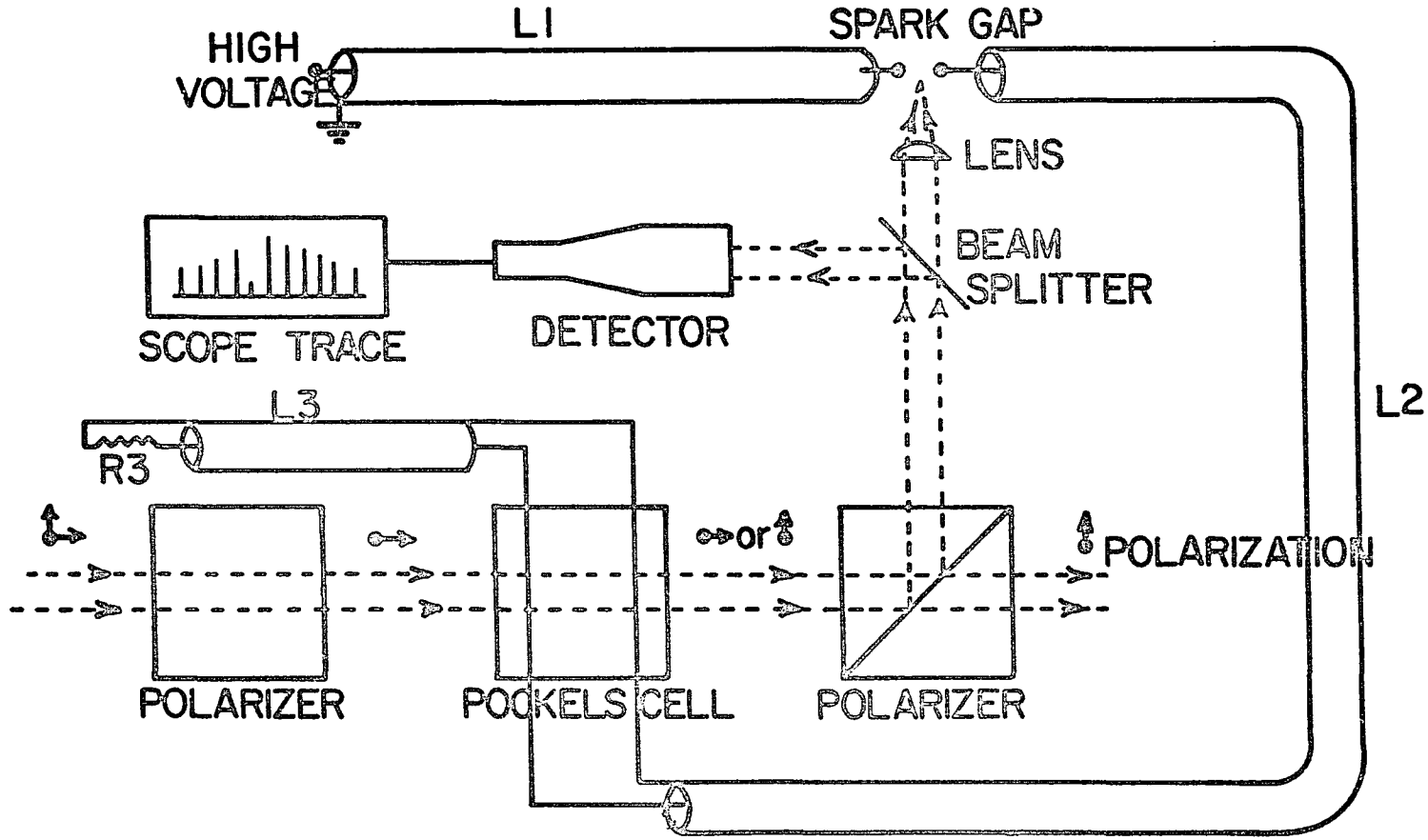

Fig. 3. Schematic Diagram of the Electro-optic Shutter System.

detector-oscilloscope combination with a rise time of approximately 1 nsec. Inspection of a photograph of the oscilloscope trace ensures that proper pulse switchout has occurred and that the pulse train is not multiple.

The Pulse Splitting and Delay Optics

The purposes of the pulse splitting and delay apparatus are to split the switched-out pulse into two parts, to temporally delay one part with respect to the other, and then to focus both parts onto a semiconductor sample. A schematic diagram of the apparatus is shown in Fig. 4. The single incident pulse is divided into two parts by a beamsplitter. One pulse (excitation) is directed to a stationary Porro prism and the other pulse (probe) to a movable Porro prism, which is capable of providing delays from 0 to 10^{-9} sec. Both pulses are then focused, by a single lens, onto a semiconductor sample mounted in a liquid nitrogen dewar.

The focal length of the lens is chosen to ensure that the angular separation of the two pulses is such that they may be unambiguously detected by separate detectors. The use of separate detectors avoids time resolution problems. Also, since the probe pulse is much weaker than the excitation pulse, the angular separation of the two pulses must be large enough to ensure that the light scattered by the semiconductor sample from the strong pulse path in the direction of the weak pulse detector is negligible. A lens of focal length 20 cm, giving an angular separation of 10°, is used in these experiments. Before each experiment, the scatter of the strong pulse into the weak pulse

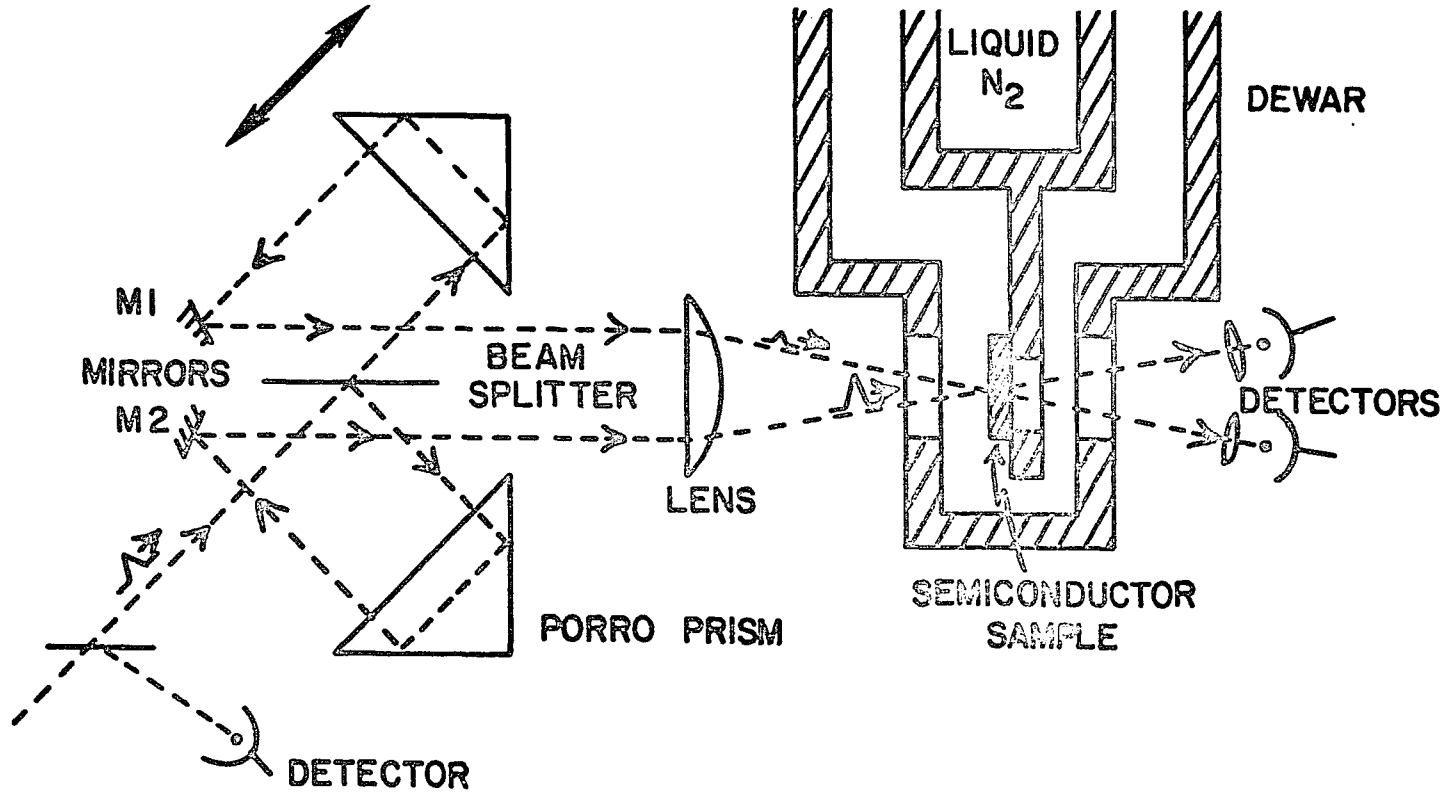

Fig. 4. Schematic Diagram of Pulse Splitter and Delay Optics.

detector is checked by blocking the weak pulse, firing the laser, and noting the voltage on the weak pulse (probe) detector.

The focusing element (lens) should be positioned after the beam splitting and delay optics. If it is placed before the Porro prism, the size of the focused probe pulse on the sample will vary with the prism delay.

The mirrors M1 and M2 may be adjusted so that the two pulses coincide at the sample surface. The overlap of the two beams is monitored by replacing the sample with a piece of darkened Polaroid film and observing the patterns burned into the film when the laser is fired.

The Pulse Monitoring Electronics

The incident pulse energy, transmission of the excitation pulse, and transmission of the probe pulse are essential parameters in excitation-probe experiments. These parameters are monitored by three detector systems as shown schematically in Fig. 4. Each detector system consists of an integrating detector circuit, an amplifying circuit, and a peak-detector-and-hold circuit. Since the detectors monitor only the energies of the pulses, the word transmission should be interpreted as energy transmission throughout this work. The detector system used in these experiments is of a unique design; it is described in detail in Appendix A. The detector system measures optical pulse energies as small as 10 nJ (at 1.06 μm) with an electronic accuracy of 1%, when read or recorded within 15 sec after the pulse is incident on the

photodiode. A single detector system of this type may be constructed for approximately $150.

The photodiode is mounted inside a copper enclosure to isolate it from electrical noise. In addition, a spatial filter consisting of a lens and pinhole combination shields the diode from extraneous light. The level of RF and optical noise present is monitored by inserting an opaque object into the laser cavity to prevent lasing, firing the flash lamps, and noting the voltages on all detectors. This shot together with the "scatter" shots described in the previous section provides an accurate measure of the noise present.

CHAPTER 3

MEASUREMENT OF RELAXATION TIMES IN SEMICONDUCTORS

The intraband relaxation processes of an electron located energetically above the conduction band minimum are complex; moreover, the evolution of these processes occurs on a time scale that is too rapid for present electronic detection systems. In some cases, the characteristic relaxation times of these processes have been determined indirectly from transport measurements. With the advent of mode-locked lasers and picosecond optical pulses, direct measurement of many of these relaxation times is now possible. The remainder of this chapter describes the procedures and results of experiments that measure the nonlinear, nonequilibrium properties of semiconductors on a picosecond time scale.

Experimental Method

The absorption of light quanta of energy greater than the band gap in a semiconductor induces an electron to make a transition from the valance band to a position high in the conduction band. A hole is left behind in the valence band (Fig. 5). After such an absorption process, the electrons (holes) will eventually relax through various collisional processes to the bottom (top) of the conduction (valence) band, where after a time long compared to a picosecond they will radiatively recombine.

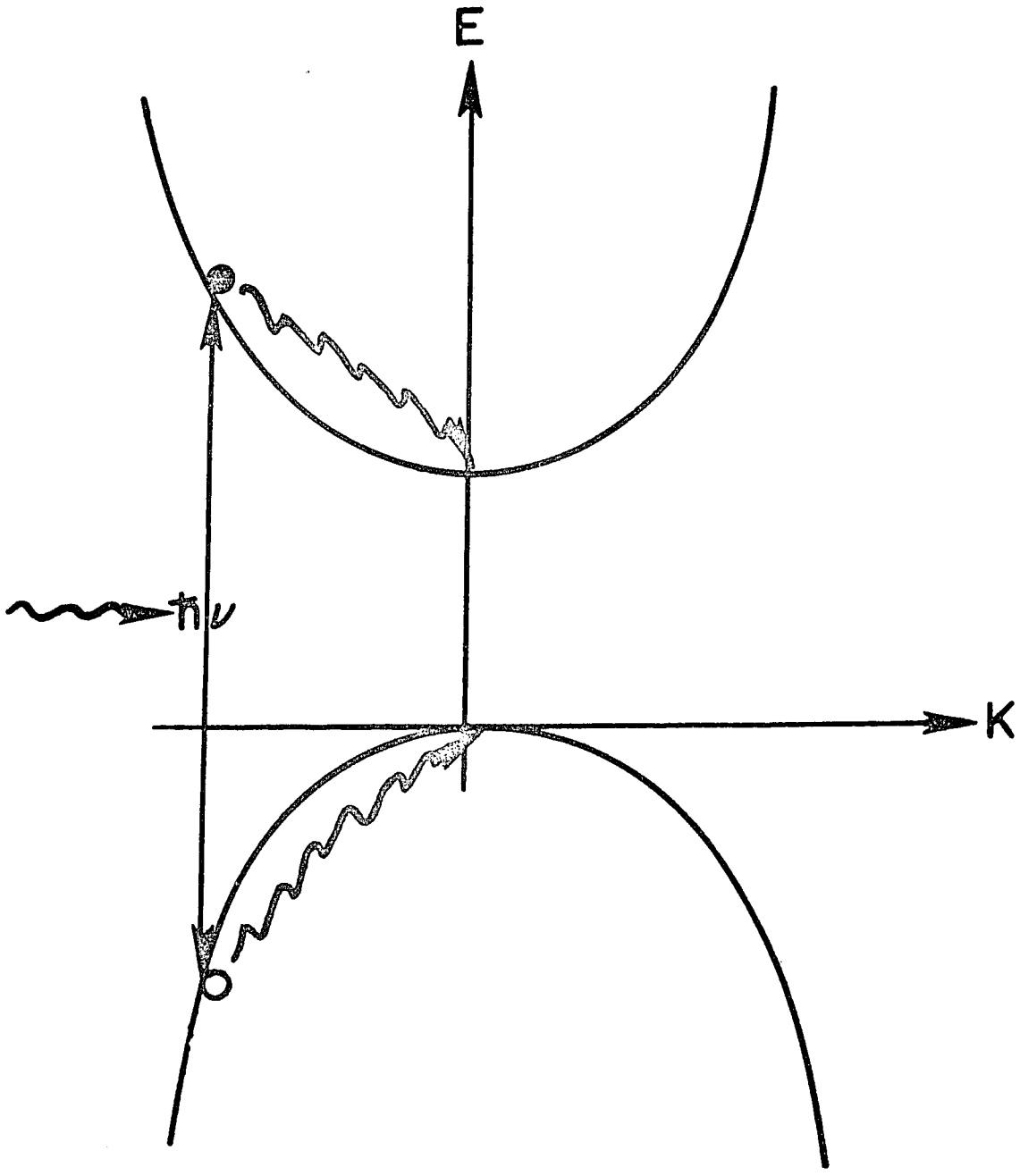

Fig. 5. Direct Optical Transitions in a Semiconductor.

Intense ultrashort pulses (typically 5 psec in duration and having peak powers on the order of 2×10^7 W) when tightly focused can produce an enormous number of such electron-hole pairs on a time scale that is short compared to many of the kinetic processes involved in the time evolution of the carrier distribution. If a sufficiently large number of carrier pairs is generated in a sufficiently short time, the optical properties of the semiconductor will be altered. In particular, if all the available states in the conduction (valence) band are occupied by electrons (holes), transitions of the type described in the first paragraph are no longer possible, and the transmission of the sample must increase. The experiments described in this section measure the degree of this saturation of the transmission and monitor its decay.

The experimental technique used to measure the nonlinear absorption of the semiconductor sample involves the use of a single picosecond optical pulse switched from the train of pulses with a laser-triggered spark gap and electro-optical shutter as described in the preceding chapter. In the first experiment, the single pulse is passed through a variable attenuator then focused onto the sample. The transmission of that pulse is then monitored as shown in Fig. 6a. This procedure when repeated for pulses of varying energy will generate a plot of transmission versus incident pulse energy. If the more energetic pulses generate enough free carriers to fill the electron states that are resonant with the optical transition, then a condition of enhanced transparency should result as described in the preceding paragraph.

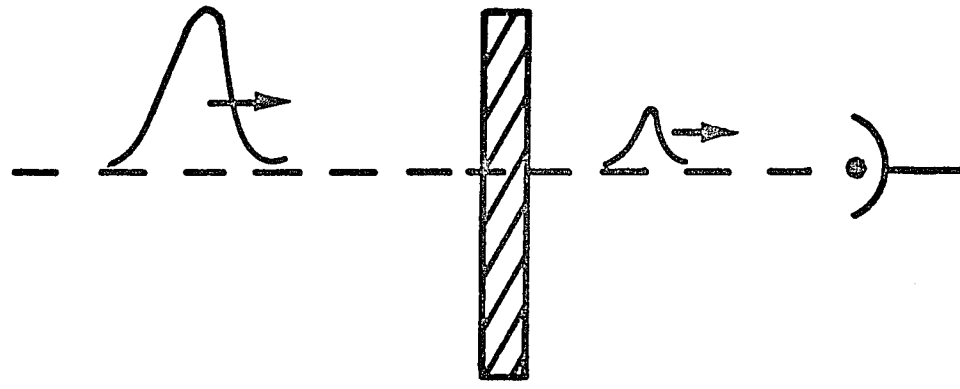

(a)

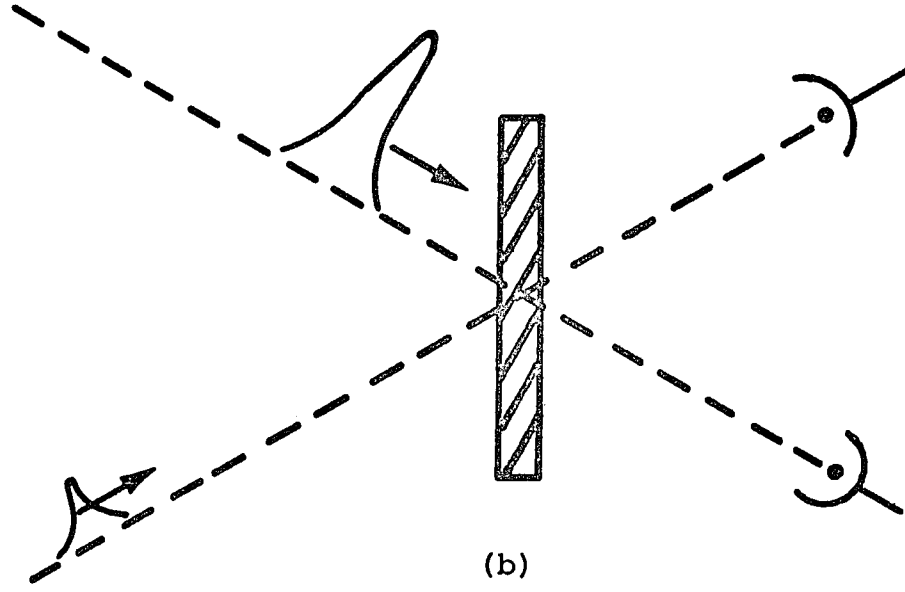

(b)

Fig. 6. Experimental Procedure for Measuring Relaxation Times in Semiconductors.

(a) Single pulse transmission, (b) excitation-probe.

The duration of this enhanced transparency may then be measured, in a second experiment, by the excitation-probe method as follows: the semiconductor sample is first irradiated by a single ultrashort pulse (excitation) of sufficient energy to cause a condition of enhanced transmission to exist; this excitation pulse is then followed at some later time by a weaker pulse (probe) that interrogates this transparency as shown in Fig. 6b. The excitation and probe pulses are derived from a single pulse as described in the section on pulse splitting and delay optics of Chapter 2. This probe pulse technique was first applied on a picosecond time scale by Shelton and Armstrong (1967).

The optical pulses used in these experiments are 5 to 10 psec in duration and are focused on the sample to a spot with an estimated diameter of approximately 480 μm. The wavelength of the radiation from the Nd:glass laser is, of course, 1.06 μm (corresponding to an energy of 1.17 eV).

Sample Preparation

The germanium wafer used in these experiments is cut from a high quality Czochralski-grown single crystal ingot, purchased from Sylvania Electronics, Inc., Towanda, Pennsylvania. The crystal is undoped, high purity (ρ_{min} = 40.0 Ω-cm) germanium cut with the (111) plane as the face. The sample is prepared by first cutting a 0.5-mm-thick wafer from the 2.5-cm-diameter ingot. One side of the wafer is polished with a compound (Linde A) having a grit size of 0.3 μm and then etched with Syton HT30 obtained from Monsanto Corporation of St. Louis, Missouri. The sample is then mounted on a KZF-2 substrate (with

the etched surface in contact with the glass), and it is polished and etched to a thickness of 5.5 μm, as determined by an interferometric technique.

The prepared sample plus glass substrate is mounted over a 0.6-cm-diameter hole in a copper block mounted in a liquid nitrogen dewar especially designed and built for this experiment.

Single Pulse Data

Figure 7 contains a plot of single pulse transmission versus pulse energy in quanta for two sample temperatures, 297 K and 105 K. Each point shown represents a single data point. For both curves the low energy transmission agrees well with that expected from the linear absorption coefficients at those two temperatures (Dash and Newman, 1955), taking into account the normal Fresnel law reflection off the surface. At both temperatures the sample exhibits a condition of enhanced transmission for large pulse energies. At 297 K the transmission increases by a factor of 3; at 105 K it increases by a factor of 20. The upper limit in energy for these curves is determined by surface damage to the sample. These data demonstrate that the states that are optically coupled are indeed saturated in some sense. The exact manner in which these transitions are saturated will be discussed in a later chapter.

Excitation-Probe Data

Figure 8 is a plot of the normalized ratio of probe pulse to excitation pulse transmission versus the delay of the probe pulse

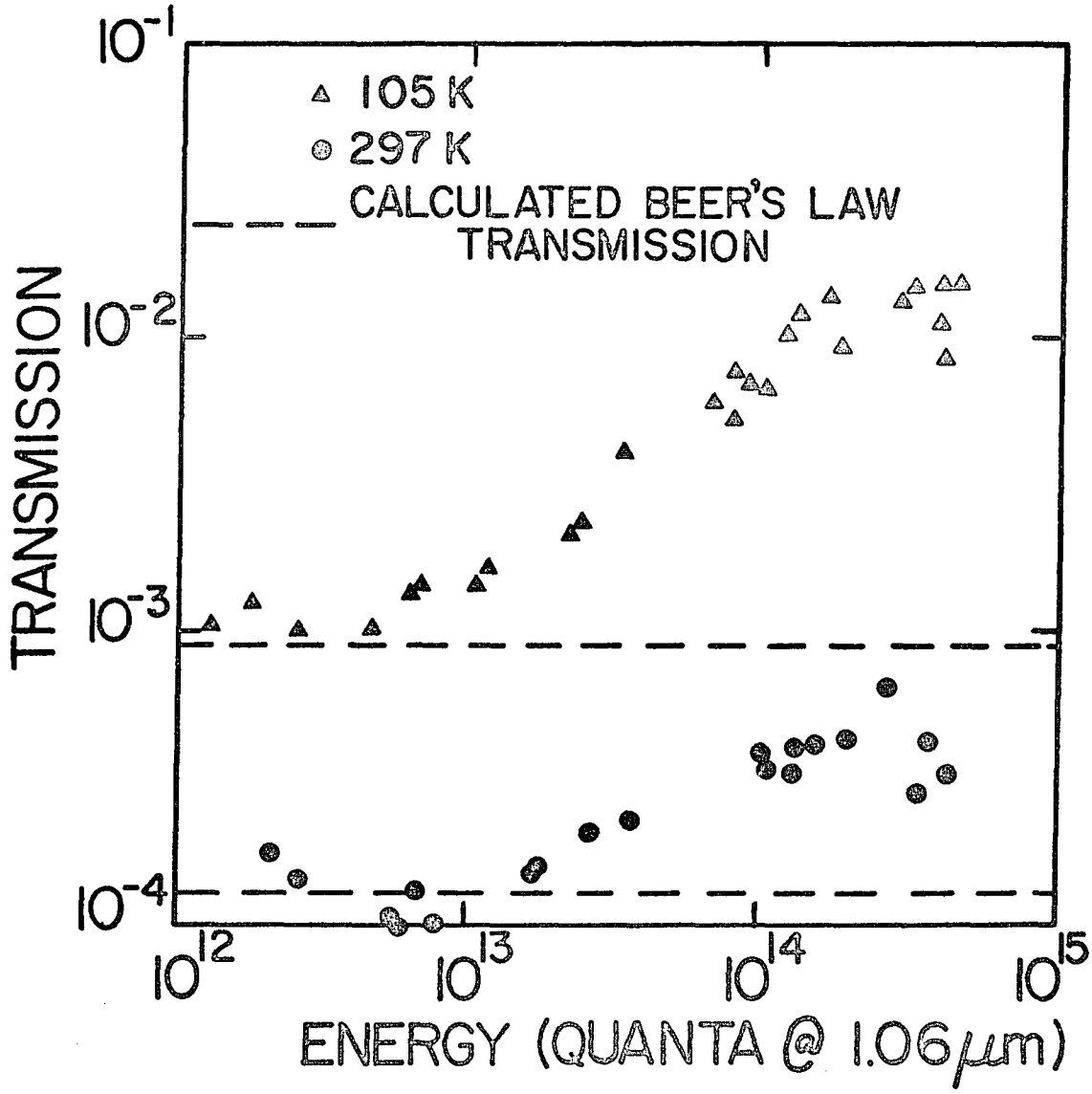

Fig. 7. Single Pulse Transmission of a 5.5 μm Thick Single Crystal Germanium Sample Versus Incident Energy in Units of Quanta at 1.06 μm for the Temperatures 297 K and 105 K.

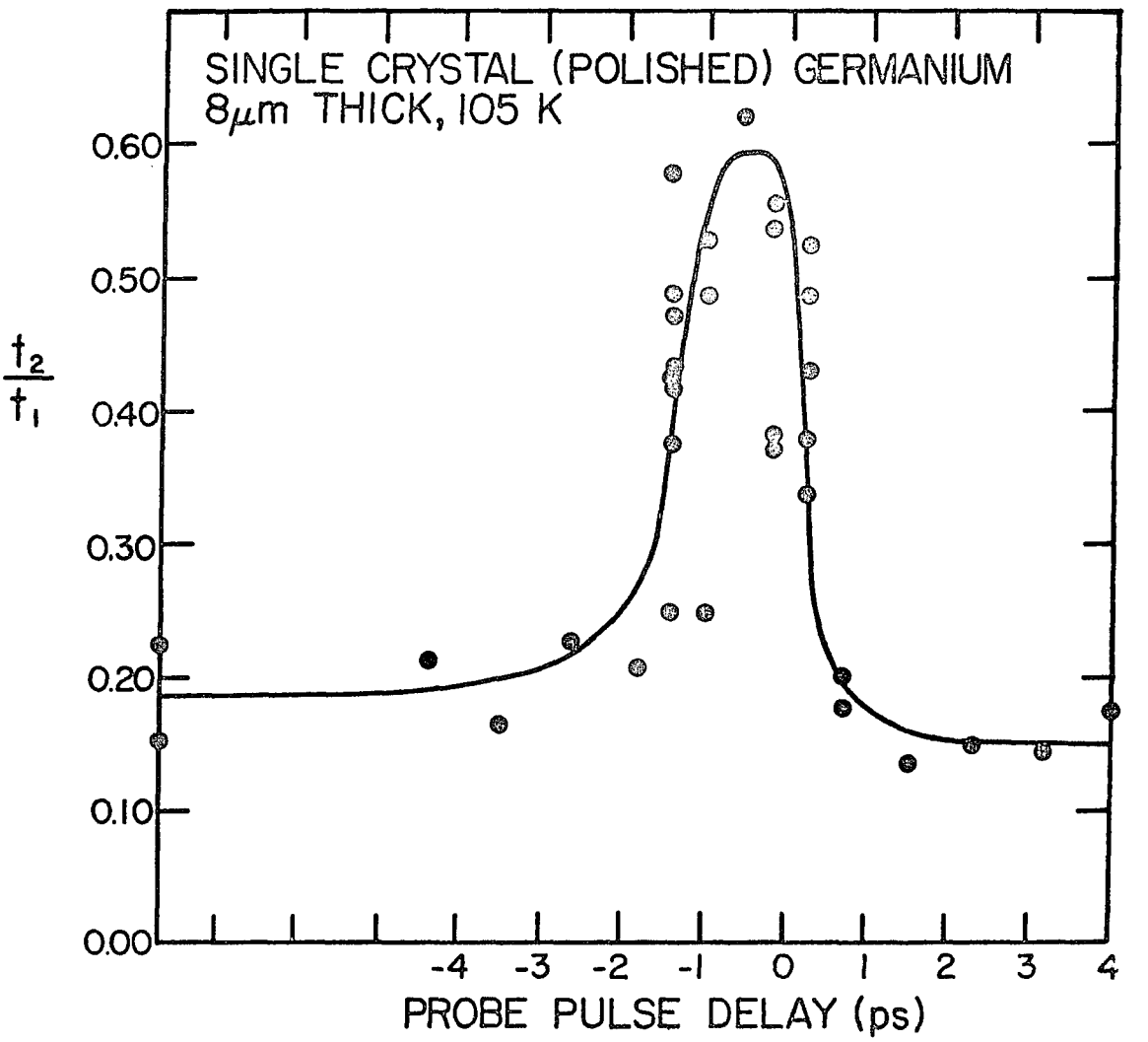

Fig. 8. Energy Transmission Ratio (t_2/t_1) Versus Delay Time (in Picoseconds) between the Excitation Pulse and the Probe Pulse.

relative to the excitation pulse for delays of a few picoseconds near the origin of pulse coincidence. The sample temperature is 105 K. Each point shown represents a single measurement. The excitation pulse contains about 10^{14} quanta. In this experiment the probe pulse has 5% of the energy of the excitation pulse. Notice that the sample used to obtain the data of Fig. 8 has a thickness of 8 μm. All other measurements are performed on a 5.5-μm-thick sample.

Notice that the width of the response shown in Fig. 8 is of the order of the duration of the excitation or the probe pulse. This spike, of a few picoseconds duration, is caused by a scattering of the excitation beam into the probe beam due to an index grating formed in the sample by the interference of the two beams, as interpreted by Shank and Auston (1975). An analysis of this "beam clashing" problem may be found in Shih et al. (1973). This correlation spike is not the main subject of this study, and it will not be discussed further.

In addition to the narrow increase in probe transmission near zero delay, a condition of enhanced probe transmission is obtained for delays as long as 100 psec. These data for sample temperatures of 297 K and 105 K are presented in Fig. 9 as a plot of the normalized ratio of the probe pulse to excitation pulse transmission versus the delay of the probe pulse relative to the excitation pulse. In these experiments the excitation pulse contains approximately 10^{14} quanta; the probe pulse has 5% of the energy of the excitation pulse. The excitation pulse is in the region of nonlinear transmission, and the probe pulse, when acting alone, is in the region of linear transmission (see Fig. 7).

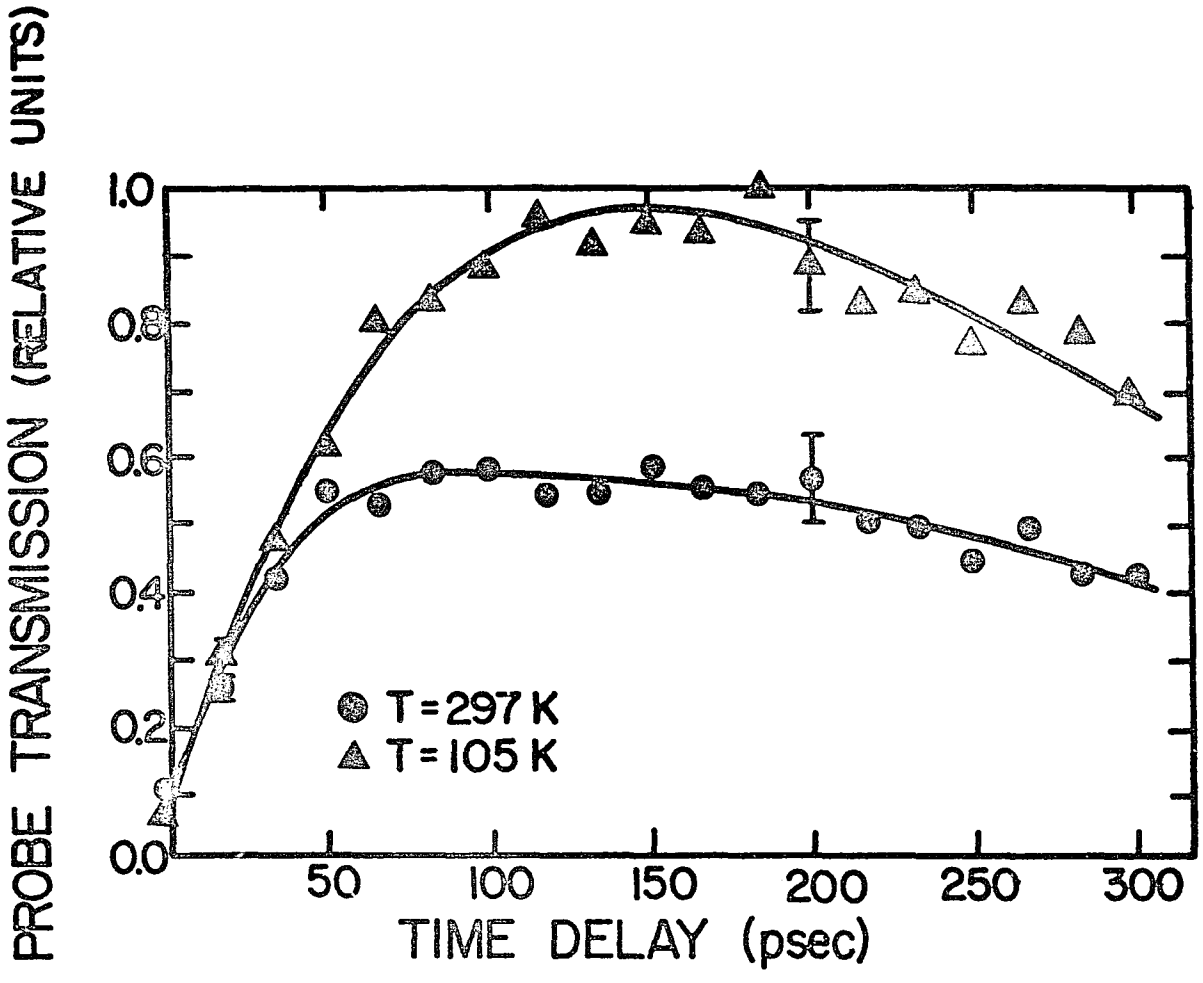

Fig. 9. Normalized Ratio of Probe Pulse Transmission to Excitation Pulse Transmission Versus Time Delay of Probe Pulse with Respect to Excitation Pulse for Temperatures 297 K and 105 K.

Each point shown is the average of six data points, and the error bars indicate one standard deviation. We note that in Fig. 9 the narrow correlation spike at zero delay is not shown owing to the gross increments in probe pulse delay.

Figure 10 is a plot of normalized probe transmission versus time delay for three different excitation pulse energies, all with the sample cooled to 105 K. Again, each plotted point is the average of six data points, and the error bars indicate one standard deviation. The ratios 100:5, 20:1, and 1:1 shown for the curves of Fig. 10 are the relative ratios of the excitation to probe energies. The 100:5 curve in Fig. 10 corresponds to the 105 K curve in Fig. 9. For the 20:1 plot, the excitation pulse is adjusted in the nonlinear transmission region to the steep part of the curve (see Fig. 7), while the probe pulse is in the linear region. For 1:1, both pulses are in the linear transmission region, and, as expected, these data are independent of time delay. (We have ignored the correlation spike at the origin in this figure also.)

In summary, Figs. 7 through 10 present measurements of the nonlinear, nonequilibrium properties of the germanium solid state plasma. Single pulse transmission has been measured as a function of incident pulse energy at sample temperatures of 105 K and 297 K. In addition, the relative transmission of a probe pulse, as a function of time delay after an excitation pulse, has been measured for three different excitation pulse energies and two temperatures. A model that explains the observed behavior of germanium under intense optical radiation is described in the next chapter.

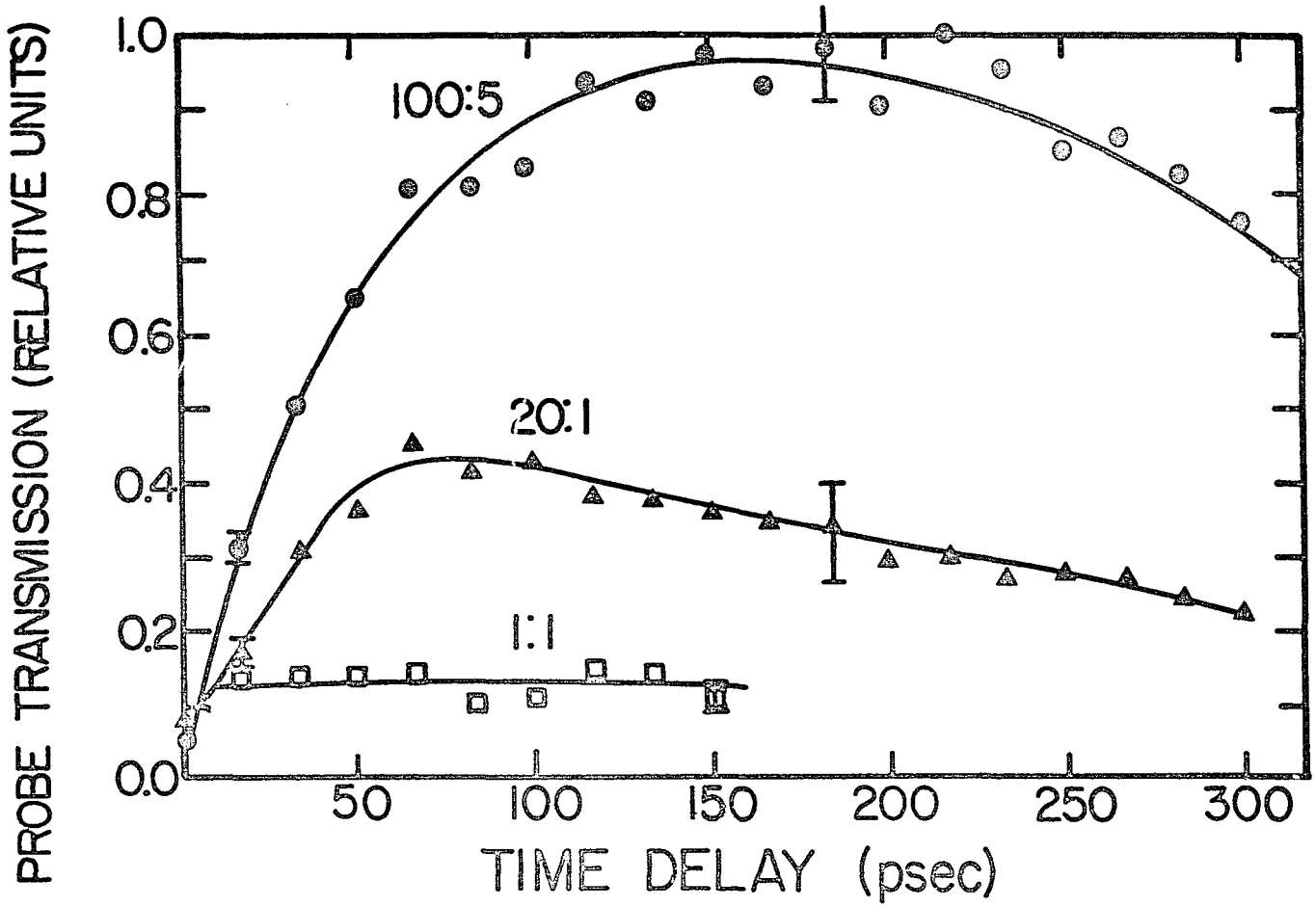

Fig. 10. Normalized Ratio of Probe Pulse Transmission to Excitation Pulse Transmission Versus Time Delay of Probe Pulse with Respect to Excitation Pulse for Three Different Excitation Energies.

Ratios labeling these curves are relative energies of excitation pulse to probe pulse.

Experimental Error

The uncertainty evident in the measurements displayed in Figs. 7 through 10 arises from the following sources: (1) measurement of probe pulse delay, (2) optical pulse detection, and (3) irreproducible pulse production.

Because the delay of the probe pulse relative to the excitation pulse is controlled by a movable prism driven by a micrometer (see Fig. 4), changes in the prism position can be read to within 0.0001 in., corresponding to an uncertainty in probe delay of 0.02 psec. Also, because the correlation spike of Fig. 8 is present only when probe and excitation pulses are coincident in the sample, the location of the peak of this spike may be used to determine zero delay. The peak of this "beam clashing" curve may be easily determined to within 1 psec. Thus, we may measure changes in delay with an accuracy of 0.02 psec and absolute delay with an accuracy of 1 psec. Therefore, there is negligible error in the abscissa of Figs. 9 and 10.

The errors inherent in the measurement of the pulse energies may be divided into the following categories: electronic accuracy, absolute radiometric calibration, relative calibration, and noise.

The electronic accuracy of the peak detector and hold circuit is 1%; it is the least significant source of error in the measurement of pulse energies. The limitations of the electronic performance of this circuit are amply discussed in Appendix A, and we will not repeat those discussions here.

A much more important source of error is the absolute radiometric calibration of the photodiode integrating circuits. These circuits were calibrated with an energy meter. However, two factors affect the complete reliability of this calibration: single pulse energies used in these experiments are in the extreme lower portion of the range of the energy meter, where the meter's accuracy is suspect, and the calibration is sensitive to the alignment of the lens and spatial filter combination mentioned in Chapter 2. The result is that the absolute calibration of the detectors may in fact be off by some significant factor. The abscissa of the single pulse measurements (absolute number of quanta) shown in Fig. 7 may then be in error by some constant factor. This factor is, however, the same for each data point. Therefore, although we might argue that the horizontal axis of Fig. 7 should be shifted slightly to the left or to the right, an error in the radiometric accuracy of the detectors would not affect the curve shape nor account for the scatter of the data in this figure.

The ordinates of Figs. 7, 9, and 10 are transmission or ratios of transmission. The accurate measurement of transmission depends on the relative sensitivities of the detectors, not the absolute sensitivity. The relative sensitivities of the detectors are determined using a calibrated beamsplitter and interference filters. This relative calibration is estimated to be accurate to 10%. Again, this error is not of sufficient magnitude to explain the large error bars of Figs. 9 or 10.

Electrical noise and optical noise from the spark gap, power supply discharge, flash lamp, spontaneous emission from the active

lasing medium, spurious reflections, scatter from the semiconductor sample, etc. are sources of error whether the energy measurement is absolute or relative. In Chapter 2, we have already discussed the precautions taken to minimize these problems: We enclose the detector in a copper case to eliminate electrical (RF) noise and we provide a lens-spatial filter combination to reduce the amount of off-axis stray light that is incident on the photodiode. In addition, for excitation-probe measurements, we require a sufficiently large angular separation between the excitation beam and probe beam to ensure that light scattered from the excitation path in the direction of the probe detector is negligible. By performing the two preliminary shots described in Chapter 2, we carefully measure the noise level at the beginning of each experiment.

We believe the main sources of error for both excitation and excitation-probe measurements to be the variation in pulse width and in energy from one laser firing to the next. The laser pulse train envelope is somewhat irreproducible, and the pulse width and shape vary with the location of the pulse in the train of pulses, as described by Von der Linde (1973). This irreproducible and random nature of the pulse evolution within the laser cavity precludes the continued selection of identical pulses by the laser-triggered spark gap. The pulse width (unmeasured) is believed to range from 5 to 15 psec in duration. The dependence of the excitation-probe data on the level of excitation is clearly depicted in Fig. 10; the theoretical dependence of the single pulse (excitation) transmission data on pulse width is illustrated in Fig. 13. (p. 66).

In addition to the uncertainty in pulse energy and width from data point to data point, the transverse mode structure of the laser is also uncertain (uncontrolled). Deviations of the transverse mode structure from the TEM_{00} mode will lead to "hot" spots on the surface of the semiconductor sample when the beam is focused. Variations in the positions of these "hot" spots as the mode structure changes from one firing to the next will result in variations in the degree of overlap between the excitation and probe beams and consequently will result in an error in the probe transmission.

Mercury Cadmium Telluride

Experimental nonlinear transmission data are also obtained for the semiconductor compound $Hg_{1-x}Cd_xTe$, where x represents the mole fraction of cadmium. These compounds have two properties that make them attractive candidates for these studies: they are direct band gap materials (thus no side valleys in the conduction band complicate the theoretical calculations) and their energy band gap may be varied by adjusting the mole fraction of cadmium x.

During single pulse transmission measurements, etched HgCdTe samples with x values of 0.6 exhibit an increase in transmission for large excitation energies. Excitation-probe measurements reveal that this state of enhanced transmission, unlike that of germanium, peaks at the origin of excitation pulse and probe pulse coincidence and that it has a lifetime of less than 50 psec.

Also, unlike germanium, the ability of the sample to exhibit a condition of enhanced transmission depends on surface preparation.

No deviation from linear, Beer's law transmission is observed for unetched samples with x values of 0.6 during single pulse transmission measurements. In addition, no increase in transmission is observed for samples, etched or unetched, with x values of 0.2 or 0.4.

The theoretical studies of these data are not yet complete, and, for this reason, the detailed discussion of these measurements is relegated to Appendix B.

CHAPTER 4

OPTICAL INTERACTIONS IN GERMANIUM

In the previous chapter, we reported the results of experiments that measured the degree and duration of a saturation of the optical transmission of germanium. There were two kinds of experiments. In the first experiment, a single picosecond pulse from a mode-locked Nd:glass laser was focused onto a thin germanium sample, and the total number of transmitted quanta was measured. The experiment was then repeated for varying pulse intensities and two sample temperatures (see Fig. 7); for extremely energetic pulses, a bleaching of the transmission was observed at both temperatures. In the second experiment, two pulses were focused on the germanium surface, each arriving at a different time. The first pulse, much more energetic than the second, caused a condition of enhanced transmission to exist in the germanium. The transmission of the second pulse was then used to probe the time evolution of the germanium transmission. This experiment was repeated for different sample temperatures and excitation energies (see Figs. 9 and 10).

Theoretical considerations naturally fall into two categories: the evolution of the germanium electron-hole distribution while the excitation pulse is present, and the evolution of that distribution from the passage of the excitation pulse to the arrival of the probe pulse. Accordingly, we will consider separately the excitation pulse (single

pulse) transmission and the probe pulse transmission. Because the transmission of both pulses is intimately connected with the energy band structure and phonon spectra of germanium, we begin the discussion with a review of these topics. This review is followed by a qualitative overview of the theoretical model and a description of the role of the various physical processes in this model. Next, an outline of the calculations describing the interaction of single intense, ultrashort pulses with germanium is presented. A theoretical description of the evolution of the sample transmission as a function of time after the passage of the excitation pulse concludes the chapter.

The main objective of this work is the presentation of the experimental data from the excitation-probe measurements and the comparison of these results with the theoretical model presented in this chapter. The presentation of the calculations will not be detailed or complete owing to the tedious and voluminous nature of these calculations. We do not believe this will detract from the presentation, but rather it will ensure that the physics of the model will not become lost in the algebra. In particular, the details of the many scattering calculations that must be performed using perturbation theory are omitted. The details of these calculations are being prepared for presentation elsewhere.

Energy Band Structure of Germanium

The energy band structure of germanium is shown in Fig. 11. The significant features of the conduction band are the locations of the conduction band valleys. The minima of these valleys are quite close in

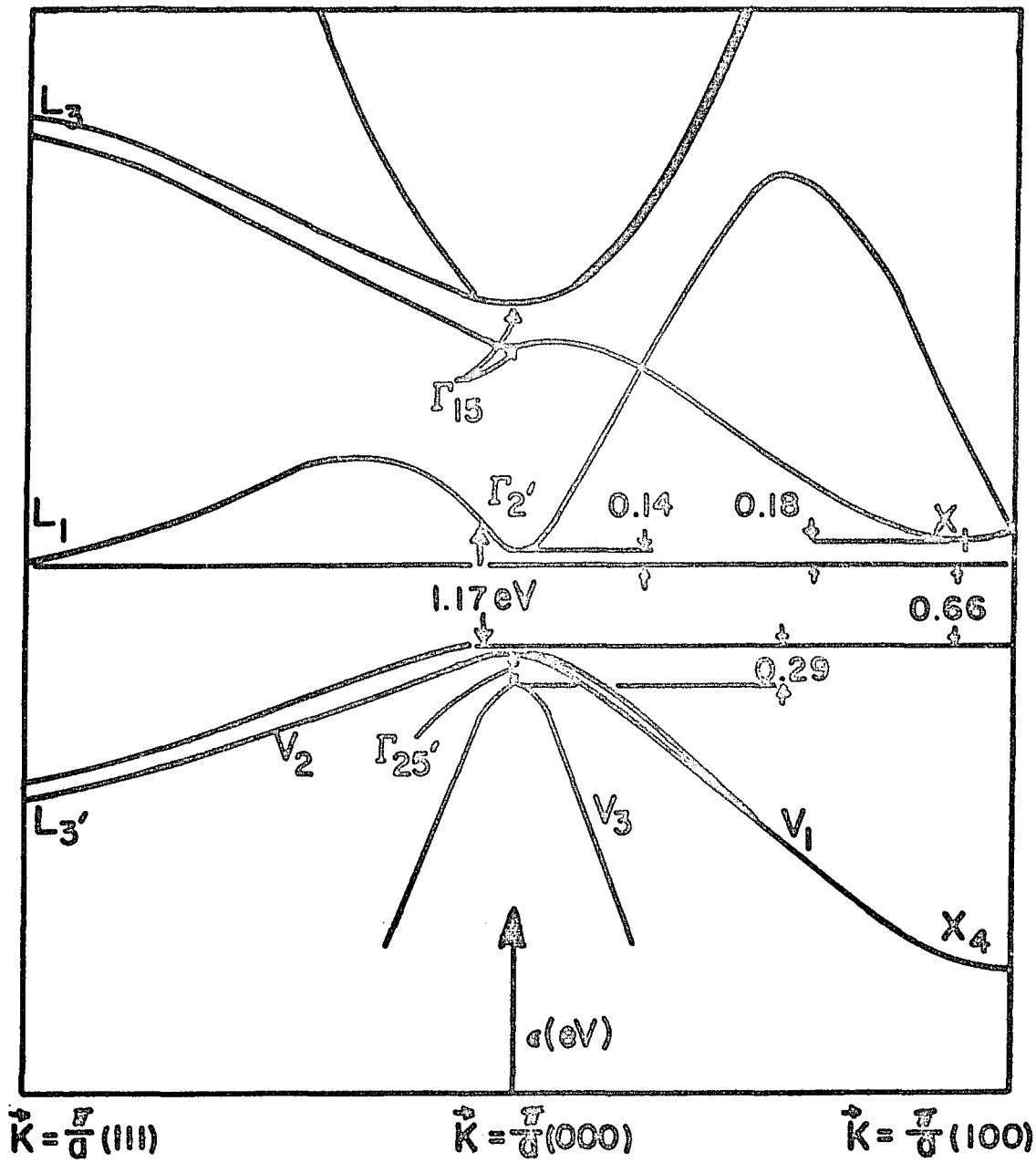

Fig. 11. Structure of the Conduction and Valence Bands of Germanium in k Space for 300 K.

energy. The minimum located at $\Gamma_{2'}$ is separated from the top of the valence band ($\Gamma_{25'}$) by 0.805 eV at 300 K. This separation is 0.889 eV at 77 K. The indirect gap located at L_1 has a separation of 0.664 eV at 300 K and a separation of 0.734 eV at 77 K. The band minimum located near X_1 is 0.18 eV higher than the minimum at L_1. There are three other valleys like the one in the (111) direction whose minima are located exactly at the Brillouin zone boundary. There are five other valleys like the one in the (100) direction. The constant energy surfaces in these valleys are elongated ellipsoids; however, these valleys enter the calculations mainly through their density of states, and the algebra may be simplified considerably by assuming a parabolic band structure with suitably chosen effective masses for the conduction band valleys. The same effective mass is assumed for the X_1 and L_1 valleys. This effective mass is taken to be $m_c \simeq 0.22$ m. The density of states effective mass of the direct conduction band valley is $m_0 \simeq 0.1$ m.

There are three valence bands. When spin-orbit splitting is neglected, two of these bands are degenerate throughout the Brillouin zone and have an effective mass $m_h \simeq 0.3$ m. The third band has an effective mass of 0.1 m; owing to its small contribution to the density of states it will be neglected. For purposes of calculating density of states, the two heavy-hole valence bands will be treated as degenerate. All of the band structure parameters quoted here, as well as the references to the original calculations and measurements, are found in Neuberger (1971).

The phonon spectrum of germanium is shown in Fig. 12. The energy is virtually independent of wave vector for the optical phonons; as a result, we assume that the transverse and longitudinal optical modes have a single energy $\hbar\Omega_0$. We approximate the acoustic phonon dispersion curves in a linear fashion. The energy of a phonon is assumed to be directly proportional to the wave vector; the proportionality constant is denoted by c_A for all polarizations.

An Overview of the Theoretical Model

When the first pulse is incident on the germanium sample, a portion is reflected. In the single-pulse experiments the reflection coefficient was monitored, and, within the accuracy of the measurement technique, the reflection coefficient remained at 36%, independent of incident pulse energy. The unreflected portion of the excitation pulse enters the bulk of the crystal where most of it is absorbed.

We note that the Kramers-Kronig relation requires that a change in the absorption coefficient, such as the one observed in the single-pulse measurements, must be accompanied by a change in the refractive index and, consequently, a change in the portion of light reflected. Such a change in index is, indeed, present, but the change is so slight that its observation requires a sensitive detection scheme. Auston and Shank (1974), using ellipsometric techniques, have measured the change in the refractive index of germanium under experimental conditions similar to those described in the previous chapter. The maximum index change observed was $\Delta n/n \simeq -0.05$, where n is the refractive index. Thus,

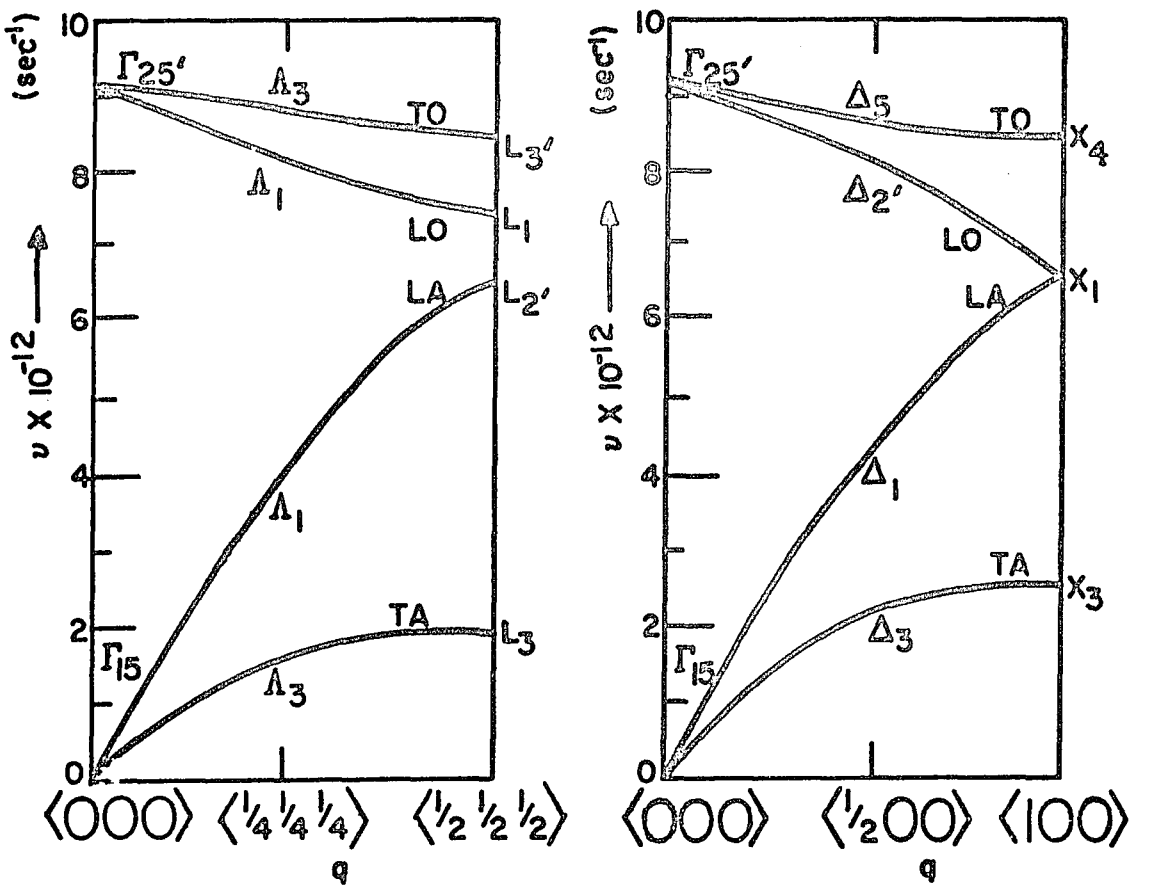

Fig. 12. Lattice Vibration Spectrum of Germanium as Determined by Brockhouse and Iyengar (1958) with Symmetry Assignment by Lax and Hopfield (1961).

the reflection coefficient may be considered constant for purposes of computing the number of quanta entering the bulk of the germanium.

The light entering the bulk of the crystal is absorbed by two processes. In the first process, direct optical absorption, a quanta of light from the excitation pulse is absorbed inducing an electron to make a transition from near the top of the valence band to the conduction band valley near Γ, leaving behind a hole in the valence band. Such a process is allowed since the energy of the light quanta (1.17 eV) is greater than the direct band gap ($\sim$0.80 eV). Once there are electrons in the conduction band and holes in the valence band, free carrier absorption is possible. Free carrier absorption is the process where an electron in any one of the conduction band valleys makes a transition to a state higher in that same valley by means of the simultaneous absorption of a quanta of light and the absorption or emission of a phonon (optical or acoustic). An identical process occurs for holes in the valence band. The rate for direct absorption (10^{13} to 10^{14} sec^{-1}) is usually larger than that for free carrier absorption (10^{10} to 10^{13} sec^{-1}). However, the rate at which direct absorption events can occur decreases as the number of unfilled electron states in the Γ-valley decreases. The rate for free carrier absorption events increases as the number of electrons (holes) in the conduction (valence) band increases. A calculation of the transition times for both direct and free carrier absorption events using perturbation theory indicates that these transitions occur on a time scale that is extremely short compared to the pulse width.

Because of the small number of electron states available in the Γ-valley, one might be tempted to conclude that the direct

transitions are saturated at very low pulse energies. In fact, this is not the case since an electron in the Γ-valley will rapidly emit or absorb a phonon and make a transition to one of the valleys at X or L. A perturbation calculation shows that the rate for electron transitions from the Γ-valley to the L-valley is greater than 10^{14} sec^{-1}. Thus, electrons are emptied from the central valley to the side valleys at a rate that is larger than the direct absorption rate, and any decrease in the number of states available for direct absorption is ultimately determined by the buildup of the electron populations in the X and L-valleys. Because we have not presented the perturbation calculation for the valley-valley scattering for the reader's inspection, he may treat the claim that this scattering rate is rapid compared to the direct absorption rate as an assumption for the model. Similar statements should be applied wherever unsupported rates are quoted in this overview. Such calculations will be presented in another work.

The direct absorption of the optical pulse creates a large number of nonequilibrium carriers. Because of the narrow bandwidth of the excitation pulse, only narrow regions of states in the central valley of the conduction and valence bands are optically coupled by direct transitions. Thus, the nonequilibrium carriers, electrons and holes, initially occupy very localized regions within the conduction band and valence band, respectively. However, since each carrier must move in the screened Coulomb field of the other carriers, carrier-carrier scattering events will occur. These events include electron-electron, electron-hole, and hole-hole collisions. The rate for such events is very large. These collisions ensure that the electron and

hole distributions will be Fermi-like. They also ensure that the Fermi distribution for holes and the distribution for the electrons will reach a common temperature, which is different from the lattice temperature. Perturbation calculations indicate that if the distributions are not Fermi-like, the lifetime of the states is short compared to the inverse of the direct absorption rate (10^{-14} sec). This may be taken into account by describing the carrier distributions by Fermi-Dirac statistics at all times.

Notice that indirect phonon-assisted interband absorption processes, which involve the transition of an electron from the valence band near Γ to either the L or X conduction band valleys and the simultaneous absorption of a photon and the absorption or emission of a phonon, have been omitted from the model. Since these indirect absorption processes involve the simultaneous interaction of a photon, electron, and phonon, one must use second-order perturbation theory to calculate the rates for such a process. The probability that an electron will reach the L or X-valley by means of an optically induced direct transition to the Γ-valley followed by a long wave vector phonon-assisted scattering to one of these side valleys is much greater than the probability that the electron will reach the same valley by means of an optically induced phonon-assisted indirect absorption. For this reason indirect optical absorption events are ignored.

Electrons located high in a conduction band valley may relax within that valley by emitting phonons. The effect of this relaxation is to reduce the electron temperature and increase the lattice temperature.

Holes, of course, may also relax by emitting phonons. The increase in lattice temperature due to these phonon-assisted intraband relaxation processes is significant only at extremely large pulse energies. Perturbation calculations indicate that the lifetime of these relaxation processes is on the order of the pulse width.

It is important to notice that the total number of carriers is unchanged by free carrier absorption or phonon-assisted relaxation within the valleys. These processes serve only to elevate or reduce, respectively, the distribution temperature. Only direct absorption will increase the number of carriers. Recombination processes serve to reduce the carrier number.

The recombination processes are divided into two general categories: radiative and nonradiative. Radiative recombination may be of two types: direct or indirect. The recombination of an electron in the Γ-valley of the conduction band with a hole in the valence band by means of emission of a photon is termed direct; the recombination of an electron in the L or X-valley with a hole in the valence band by means of simultaneous emission of a photon and emission (or absorption) of a phonon is termed indirect. Both processes occur on a nanosecond time scale. These processes, although included in the formalism and final equations presented in Appendix D, do not appreciably affect the carrier number of the time scales of interest.

Nonradiative recombination is far more important in reducing the carrier number than radiative recombination. The large number of

quanta absorbed by the crystal results in a large carrier density; these carriers have collective plasma oscillations. The characteristic frequency (plasma frequency) of these oscillations is proportional to the square root of the carrier density. When the density of carriers is such that the plasma frequency is energetically near the direct gap energy E_0 or the indirect gap energy E_G, electrons and holes can recombine while simultaneously emitting plasmons. When the plasmon energy is near E_0 or E_G, the rate for these recombination processes is large enough to compete with direct and free carrier absorption rates. These nonradiative recombination processes are, in fact, as important in determining the final number of conduction electrons as the saturation in the total number of available electron states in the conduction band due to the buildup of the electron population.

The nonradiative plasma recombinations can be direct or indirect. An electron from the Γ-valley can directly recombine with a hole in the valence band while emitting a plasmon, or an electron in the X or L-valley can make a virtual transition to the Γ-valley by means of the emission or absorption of a phonon then recombine with a hole in the valence band while emitting a plasmon. The rates for the direct and indirect nonradiative recombinations are different. Which process is dominant depends on whether the plasmon energy, $\hbar\omega_p$, is nearer E_0 or E_G. When the plasmon energy is near E_G, the indirect recombinations are more important; direct plasma recombinations are negligible. When the plasmon energy is near E_0, the direct plasma recombinations, which are much faster than the indirect, dominate.

We assume that the collective plasma oscillations have a lifetime that is short compared to a picosecond. The energy lost in the decay of the plasma oscillations is transferred to single electron and hole states and, therefore, serves to ultimately increase the temperature of the carrier distribution. The nonradiative plasma recombinations thus serve both to limit the number of carriers by inducing electron-hole recombinations and to cause energy absorbed from the pulse by direct optical transitions to raise the electron-hole temperature.

The diffusion of carriers from the interaction region (focused spot size times sample thickness) also reduces the carrier number. Calculations using the Boltzmann equation indicate that the number of carriers leaving the interaction region on a picosecond time scale is negligible.

In summary, the following processes are rapid compared to the width of the optical pulses from the Nd:glass laser: direct absorption, phonon-assisted valley-to-valley electron scattering, particle-particle scattering, nonradiative recombination, and free carrier absorption. Intravalley phonon-assisted decay times are on the same order as the pulse width. Radiative recombination and diffusion occur on a time scale much too slow to be of interest in this problem.

When the excitation pulse enters the crystal, it is absorbed by direct optical transitions, creating a large number of electrons in the Γ-valley. These electrons are quickly scattered to the L and X-valleys by long wave vector phonons. Particle-particle scattering events ensure that the carrier distributions obey Fermi-Dirac statistics

and that both electron and hole distributions have the same temperature. Free carrier events elevate the carrier distribution temperature. For large excitation pulse energies plasma recombinations eventually limit the carrier number and also serve to heat the distribution. All of these processes occur rapidly while the excitation pulse is interacting with the sample.

After the passage of the excitation pulse, the interaction region of the sample contains a large number of carriers with a high distribution temperature. As time progresses, the distribution temperature may be reduced by phonon-assisted intraband relaxation. After a long time (nanoseconds), the carrier number may be reduced by radiative recombinations and diffusion of carriers from the interaction region. The weak (probe) pulse interrogates this evolution of the distribution. The probe transmission indicates whether the states that are optically coupled are available for absorption or whether they are occupied. Keep in mind that electrons deposited in the central valley of the conduction band are immediately scattered to the side valleys. Thus, the central valley states available for direct absorption are saturated only if states in the side valleys are also filled.

The probe pulse transmission may be understood in the following way. Immediately after the passage of the excitation pulse, the carriers are located high in the valleys because of the high distribution temperature, leaving the states that are optically coupled vacant and available for absorption. Probe transmission is small. Later, the distribution cools by means of intraband phonon-assisted transitions, and carriers

fill the states needed for absorption. Probe transmission increases. Finally, as the distribution temperature cools to near the lattice temperature, the carriers occupy states near the very bottom of the bands, and states needed for absorption are once again available. Probe transmission decreases. Thus we see qualitatively how this model accounts for the rise and fall of the probe transmission as displayed in Fig. 9.

In the following pages, we choose a set of parameters that describes the electron and hole distributions, and we outline the derivation of equations that, through the interactions described above, determine the behavior of the probe absorption as a function of sample temperature and excitation pulse energy.

Excitation Pulse Absorption

In the overview, we argued that if electron and hole distributions are not Fermi-like, the lifetime of the occupied states will be exceedingly short. Thus, the distributions will rapidly relax by means of particle-particle collisions to Fermi distributions. This fact can be taken into account by defining the electron and hole distributions to be Fermi-like at all times as far as the light absorption is concerned. For electrons we define

$$f_{c\Gamma}(\vec{k}) = \frac{1}{1 + \exp\left(\frac{E_{c\Gamma}(\vec{k}) - E_F}{T}\right)}, \quad E_0 \leq E_{c\Gamma}(\vec{k}) < +\infty \qquad (1)$$

$$f_{cL,X}(\vec{k}) = \frac{1}{1 + \exp\left(\frac{E_{cL,X}(\vec{k}) - E_F}{T}\right)}, \quad E_G \leq E_{cL,X}(\vec{k}) < +\infty \qquad (2)$$

and for holes

$$f_h(\vec{k}) = \frac{1}{1 + \exp\left(\frac{E_h(\vec{k}) + E_h}{T}\right)}, \quad 0 \leq E_h(\vec{k}) < +\infty, \tag{3}$$

where Fermi distributions are represented by $f_i(k)$, normalized energies by E_i, and normalized distribution temperatures by T. The subscript cΓ denotes the Γ-valley of the conduction band, cL the L-valley of the conduction band, and cX the X-valley of the conduction band. The subscript h represents holes in the valence band. Thus, for example, $f_{c\Gamma}(\vec{k})$ represents the Fermi-Dirac distribution for the electrons in the Γ-valley of the conduction band. E_F and E_h are the normalized Fermi energies of the electrons and holes, respectively. E_0 and E_G are the normalized energies of the direct and indirect energy gaps, respectively. The indirect energy gap is taken to be $E_G \equiv (8E_L + 6E_X)/14$, where E_L is the normalized energy band gap at L and E_X, the normalized energy band gap at X, for both the conduction band valley at X and the valley at L. All energies are normalized in terms of $\hbar\omega_0$ in the following manner:

$$E_{cL,X}(\vec{k}) = \frac{1}{\hbar\omega_0}\left(E_G + \frac{\hbar^2k^2}{2m_c}\right) = E_G + \frac{\hbar^2k^2}{2\hbar\omega_0 m_c}, \tag{4}$$

$$E_{c\Gamma}(\vec{k}) = \frac{1}{\hbar\omega_0}\left(E_0 + \frac{\hbar^2k^2}{2m_0}\right) = E_0 + \frac{\hbar^2k^2}{2\hbar\omega_0 m_0}, \tag{5}$$

$$E_h(\vec{k}) = \frac{\hbar^2k^2}{2\hbar\omega_0 m_h}, \tag{6}$$

$$E_h = \frac{E_h}{\hbar\omega_0} \text{ and } E_F = \frac{E_F}{\hbar\omega_0}, \tag{7}$$

and the normalized temperature is

$$T = \frac{k_B T}{\hbar\omega_0}, \tag{8}$$

where $\hbar$ is Planck's constant divided by 2π, k the wavevector of the electron, k_B Boltzmann's constant, and ω_0 the circular frequency of the optical pulse. These distributions depend on time through T, E_h, and E_F. E_h and E_F are related since the total number of electrons is equal to the total number of holes at all times.

The electron density is measured in terms of N_0 which is defined by

$$N_0 = \frac{\varepsilon_\infty m\omega_0^2}{4\pi e^2}, \tag{9}$$

where ε_∞ is the high frequency dielectric constant and e the electron charge. Neglecting the Γ-valley and considering the effective mass of each of the four L-valleys to be equal to that of each of the six X-valleys, the electron density is calculated as 10 times the density in any one valley

$$n = A\int_0^\infty dy y^{1/2} F\left(\frac{y + E_G - E_F}{T}\right) \tag{10}$$

where

$$A \equiv \frac{5}{\pi^2 N_0}\left(\frac{2m_c\omega_0}{\hbar}\right)^{3/2} \tag{11}$$

and

$$F(Z) \equiv \frac{1}{1 + e^Z}. \tag{12}$$

Since the number of holes is equal to the number of electrons, n is also given by (summing over two valence bands)

$$n = B \int_0^\infty dy y^{1/2} F\left(\frac{y + E_h}{T}\right) \tag{13}$$

$$B \equiv \frac{1}{\pi^2 N_0} \left(\frac{2m_h \omega_0}{\hbar}\right)^{3/2} . \tag{14}$$

Notice that the electron and hole distributions are taken to be time dependent only. By neglecting the spatial dependence within the interaction region, we are ignoring the pulse propagation problem. This is a major assumption and its consequences are being investigated. The distributions should be or can be viewed as spatial averages of the actual distributions over the interaction region.

The photon distribution within the interaction region is also assumed to be time dependent but not space dependent: $N_q = N_q(t)$. In addition, we assume that all quanta are of the same wave vector: $W(t) = \sum_q \hbar\omega_q N(t) \simeq \hbar\omega_0 N_0(t)$.

Notice that due to the rapid nature of phonon-assisted intervalley scattering, we take E_F to be the same for the central valley and all 10 (L and X) side valleys.

The variation of the Fermi-Dirac distributions with time during the interaction of the excitation pulse with the sample may be separated in the following fashion:

$$\frac{df_{c\Gamma}(\vec{k})}{dt} = \left(\frac{\partial f_{c\Gamma}}{\partial t}\right)_{DA} + \left(\frac{\partial f_{c\Gamma}}{\partial t}\right)_{FCA} + \sum_j \left(\frac{\partial f_{c\Gamma}}{\partial t}\right)_{\Gamma \to j} + \left(\frac{\partial f_{c\Gamma}}{\partial t}\right)_{REL} + \left(\frac{\partial f_{c\Gamma}}{\partial t}\right)_{DR} \tag{15}$$

$$\frac{df_{cj}(\vec{k})}{dt} = -\left(\frac{\partial f_{c\Gamma}}{\partial t}\right)_{\Gamma\to j} + \left(\frac{\partial f_{cj}}{\partial t}\right)_{FCA} + \left(\frac{\partial f_{cj}}{\partial t}\right)_{REL} + \left(\frac{\partial f_{cj}}{\partial t}\right)_{IR} \tag{16}$$

$$\frac{df_{h}(\vec{k})}{dt} = \left(\frac{\partial f_{h}}{\partial t}\right)_{DA} + \left(\frac{\partial f_{h}}{\partial t}\right)_{FCA} + \left(\frac{\partial f_{h}}{\partial t}\right)_{DR} + \left(\frac{\partial f_{h}}{\partial t}\right)_{IR} + \left(\frac{\partial f_{h}}{\partial t}\right)_{REL}, \tag{17}$$

where DA represents the direct absorptions; FCA, the free carrier absorptions; $\Gamma\to j$, the phonon-assisted scattering from the Γ-valley to the jth valley; REL, the intravalley relaxation of electrons and holes by means of emission or absorption of phonons; DR, the direct plasmon recombination; and, finally, IR, the indirect plasmon recombination. We note that the direct absorption terms mainly contribute to an increase in the carrier number. The free carrier absorption contributions serve to increase the distribution temperature. The intravalley phonon-assisted relaxation terms decrease the distribution temperature. The direct and indirect recombination terms decrease the electron number and increase the distribution temperature. The $\Gamma\to j$ scattering terms do not change either the electron number or temperature; rather, they serve to populate the side valleys in the conduction band.

Notice that every term on the right-hand side of Eqs. (15) through (17) may be readily evaluated using perturbation theory. To evaluate each such term in this work would be distracting and tedious. However, the perturbation calculation for one term, $(\partial f_{cj}/\partial t)_{REL}$, is performed in detail in Appendix C. The procedure is the same for all first-order perturbation calculations. The procedure for second-order calculations is similar to that for the first-order ones. A detailed

and tutorial calculation of the second-order free carrier terms may be found in Matter (1975).

The behavior of the Fermi distributions for both electrons and holes is determined if E_F, E_h, and T are known at all times. We now derive a set of differential equations that describe the behavior of E_F, E_h, and T with time.

Consider first the time behavior of the electron density, which is given by

$$\sum_{\vec{k}} \frac{df_{c\Gamma}(\vec{k})}{dt} + \sum_{\vec{k}} \sum_{j} \frac{df_{cj}(\vec{k})}{dt} = \frac{dn}{dt}, \tag{18}$$

where j denotes a summation over all conduction band side valleys. We substitute Eqs. (15) through (17) into Eq. (18), recognizing that the free carrier terms, $\Gamma \rightarrow j$ terms, and relaxation terms do not affect the electron density. The result is

$$\frac{dn}{dt} = \sum_{\vec{k}} \left(\frac{\partial f_{c\Gamma}(\vec{k})}{\partial t}\right)_{DA} + \sum_{\vec{k}} \left(\frac{\partial f_{c\Gamma}(\vec{k})}{\partial t}\right)_{DR} + \sum_{\vec{k}} \sum_{j} \left(\frac{\partial f_{cj}(\vec{k})}{\partial t}\right)_{IR}. \tag{19}$$

However, inspection of Eq. (10) shows that n is a function of E_F and T. Thus we can also write

$$\frac{dn}{dt} = \left(\frac{\partial n}{\partial E_F}\right)_T \cdot \frac{dE_F}{dt} + \left(\frac{\partial n}{\partial T}\right)_{E_F} \cdot \frac{dT}{dt}, \tag{20}$$

where we define

$$\rho_{FE}(E_F,T) \equiv \left(\frac{\partial n}{\partial E_F}\right)_T \tag{21}$$

$$\rho_{TE}(E_F,T) \equiv \left(\frac{\partial n}{\partial T}\right)_{E_F}. \tag{22}$$

Obviously, ρ_{FE} and ρ_{TE} are easily obtained by differentiating Eq. (10). Equation (19) becomes

$$\rho_{FE}\frac{dE_F}{dt} + \rho_{TE}\frac{dT}{dt} = \sum_{\vec{k}}\left(\frac{\partial f_{c\Gamma}(\vec{k})}{\partial t}\right)_{DA} + \sum_{\vec{k}}\left(\frac{\partial f_{c\Gamma}(\vec{k})}{\partial t}\right)_{DR} + \sum_{\vec{k}}\sum_{j}\left(\frac{\partial f_{cj}(\vec{k})}{\partial t}\right)_{IR}. \tag{23}$$

Equation (23) is a differential equation that relates dE_F/dt and dT/dt; all other terms may be determined from either perturbation calculations or Eq. (10).

The fact that the number of electrons equals the number of holes requires that E_F and E_h be related by

$$\frac{dn}{dt} = \left(\frac{\partial n}{\partial E_h}\right)_T\frac{dE_h}{dt} + \left(\frac{\partial n}{\partial T}\right)_{E_h}\frac{dT}{dt} = \left(\frac{\partial n}{\partial E_F}\right)_T\frac{dE_f}{dt} + \left(\frac{\partial n}{T}\right)_{E_F}\frac{dT}{dt}. \tag{24}$$

We define

$$\gamma_{HE}(E_F,E_h,T) \equiv -\frac{(\partial n/\partial E_F)_T}{(\partial n/\partial E_h)_T} \tag{25}$$

and

$$\gamma_{HT}(E_F,E_h,T) \equiv \frac{(\partial n/\partial T)_{E_F} - (\partial n/\partial T)_{E_h}}{(\partial n/\ E_h)_T}. \tag{26}$$

Then,

$$\frac{dE_h}{dt} = -\gamma_{HE}\frac{dE_F}{dt} + \gamma_{HT}\frac{dT}{dt}. \tag{27}$$

Expressions for γ_{HE} and γ_{HT} are evaluated by differentiating Eqs. (10) and (13).

To this point, we have obtained two differential equations, (23) and (27), relating three unknowns E_F, E_h, T. We wish to find still a third independent differential equation relating these variables. We accomplish this by considering the energy density of the electrons and holes. The total energy is given by

$$u = u_e + u_h \tag{28}$$

and

$$\frac{du}{dt} = \sum_{\vec{k}} E_{c\Gamma}(\vec{k}) \frac{df_{c\Gamma}(\vec{k})}{dt} + \sum_{\vec{k}} \sum_{j} E_{cj}(\vec{k}) \frac{df_{cj}(\vec{k})}{dt} + 2 \sum_{\vec{k}} E_h(\vec{k}) \frac{df_h(\vec{k})}{dt} . \tag{29}$$

The energy lost to the lattice due to $\Gamma \rightarrow j$ phonon-assisted scattering events is negligible. As discussed earlier, nonradiative recombinations do not change u. Radiative recombinations would decrease the total energy, but they are negligible. The free carrier absorption and phonon-assisted intravalley relaxation contributions of the Γ-valley to the energy are negligible compared to those of the L and X-valleys. The following equations summarize these statements

$$\frac{du}{dt} = \left(\frac{\partial u}{\partial t}\right)_{DA} + \left(\frac{\partial u}{\partial t}\right)_{FCA} + \left(\frac{\partial u}{\partial t}\right)_{PEL} \tag{30}$$

where

$$\left(\frac{\partial u}{\partial t}\right)_{DA} = \sum_{\vec{k}} E_{c\Gamma}(\vec{k}) \left[\frac{\partial f_{c\Gamma}(\vec{k})}{\partial t}\right]_{DA} + 2 \sum_{\vec{k}} E_h(\vec{k}) \left[\frac{\partial f_c(\vec{k})}{\partial t}\right]_{DA}, \tag{31}$$

$$\left(\frac{\partial u}{\partial t}\right)_{FCA} = \sum_{\vec{k}} \sum_{j} E_{cj}(\vec{k}) \left(\frac{\partial f_{cj}(\vec{k})}{\partial t}\right)_{FCA} + 2 \sum_{\vec{k}} E_{h}(\vec{k}) \left(\frac{\partial f_{h}(\vec{k})}{\partial t}\right)_{FCA}, \tag{32}$$

and

$$\left(\frac{\partial u}{\partial t}\right)_{REL} = \sum_{\vec{k}} \sum_{j} E_{cj}(\vec{k}) \left(\frac{\partial f_{cj}(\vec{k})}{\partial t}\right)_{REL} + 2 \sum_{\vec{k}} E_{h}(\vec{k}) \left(\frac{\partial f_{h}(\vec{k})}{\partial t}\right)_{REL}. \tag{33}$$

Using Eqs. (10) and (13), we obtain

$$u = A \int_{0}^{\infty} dy y^{1/2}(y + E_G) F\left(\frac{y + E_G - E_F}{T}\right) + B \int_{0}^{\infty} dy y^{3/2} F\left(\frac{y + E_h}{T}\right). \tag{34}$$

Notice that

$$u = u(E_F, E_h, T). \tag{35}$$

Therefore,

$$\frac{du}{dt} = \left(\frac{\partial u}{\partial E_F}\right)_{T,E_h} \cdot \frac{dE_F}{dt} + \left(\frac{\partial u}{\partial E_h}\right)_{T,E_F} \cdot \frac{dE_h}{dt} + \left(\frac{\partial u}{\partial T}\right)_{E_F,E_h} \cdot \frac{dT}{dt}. \tag{36}$$

Making use of the definitions of γ_{HE} and γ_{HT}, we obtain

$$\frac{du}{dt} = \left[\left(\frac{\partial u}{\partial E_F}\right)_{T,E_h} - \left(\frac{\partial u}{\partial E_h}\right)_{T,E_F} \cdot \gamma_{HE}\right] \frac{dE_F}{dt} + \left[\left(\frac{\partial u}{\partial T}\right)_{E_F,E_h} + \left(\frac{\partial u}{\partial E_h}\right)_{T,E_F} \cdot \gamma_{HT}\right] \frac{dT}{dt}. \tag{37}$$

Let us define

$$\rho_{UF} \equiv \left[\left(\frac{\partial u}{\partial E_F}\right)_{T,E_h} - \left(\frac{\partial u}{\partial E_h}\right)_{T,E_F} \cdot \gamma_{HE}\right] \tag{38}$$

$$\rho_{UT} \equiv \left[\left(\frac{\partial u}{\partial T}\right)_{E_F,E_h} + \gamma_{HT}\left(\frac{\partial u}{\partial E_h}\right)_{T,E_F}\right] . \tag{39}$$

Thus,

$$\rho_{UF}\frac{dE_F}{dt} + \rho_{UT}\frac{dT}{dt} = \left(\frac{\partial u}{\partial t}\right)_{DA} + \left(\frac{\partial u}{\partial t}\right)_{FCA} + \left(\frac{\partial u}{\partial t}\right)_{REL}. \tag{40}$$

Notice that expressions for ρ_{UF} and ρ_{UT} are obtained by partial differentiation of Eqs. (34), (10), and (13). Also notice that all of the terms on the right-hand side of Eq. (40) can be evaluated using perturbation theory. One such term, $(\partial u/\partial t)_{REL}$, is evaluated in Appendix C to illustrate the procedure. Equations (23), (27), and (40) constitute the basic differential equations describing the time evolution of E_F, E_h, and T during the time the excitation pulse interacts with the sample. The final form of these differential equations after the evaluation of ρ_{FE}, ρ_{TE}, γ_{HE}, γ_{HT}, and the various scattering terms is presented in Matter (1975), along with a description of the numerical solution of these equations.

The equations presented in this section are modified substantially after the excitation pulse passes. The following section outlines these modifications.

Probe Pulse Absorption

After the passing of the excitation pulse, the interaction region of the crystal contains a large number of nonequilibrium carriers with a high distribution temperature. The probe pulse is of sufficiently

low energy that it does not noticeably perturb the carrier distribution, but merely monitors its time evolution. During the period between the passing of the excitation pulse and the arrival of the probe pulse (a period of from 0 to 300 psec), no optical field is present, and no free carrier or direct absorption events are possible. Many of the equations of the previous section must be modified to reflect these facts. Equations (15) through (17) become

$$\frac{df_{c\Gamma}(\vec{k})}{dt} = \sum_j \left(\frac{\partial f_{c\Gamma}}{\partial t}\right)_{\Gamma\to j} + \left(\frac{\partial f_{c\Gamma}}{\partial t}\right)_{REL} + \left(\frac{\partial f_{c\Gamma}}{\partial t}\right)_{other} \tag{41}$$

$$\frac{df_{cj}(\vec{k})}{dt} = - \left(\frac{\partial f_{c\Gamma}}{\partial t}\right)_{\Gamma\to j} + \left(\frac{\partial f_{cj}}{\partial t}\right)_{REL} + \left(\frac{\partial f_{cj}}{\partial t}\right)_{other} \tag{42}$$

$$\frac{df_{h}(\vec{k})}{dt} = \left(\frac{\partial f_{h}}{\partial t}\right)_{REL} + \left(\frac{\partial f_{h}}{\partial t}\right)_{other}. \tag{43}$$

These equations describe the electron and hole distributions after the first pulse leaves the sample.

The terms subscripted "other" include the indirect (IR) and direct (DR) nonradiative plasma recombination terms, which were present in the previous section, as well as radiative recombination and diffusion terms, which are added for this section. Once direct absorption events cease, the plasma recombination processes quickly (with respect to a picosecond) reduce the carrier number to a level where the plasma frequency is less than either the direct or indirect band gap. The net result is that the plasma recombination processes are negligible when computing the probe transmission for finite delays. The radiative

recombination and diffusion terms represent slow processes that were negligible during the short period the excitation pulse interacted with the crystal. In fact, they are also negligible here, except for time delays in the nanosecond region. Thus the effect of the "other" terms may be neglected for time delays from 0 to 300 psec. These terms are included in the final equations presented in Appendix D, but for clarity of presentation, they will initially be omitted from the discussions of this section.

Continuing with our modification of the equations of the previous chapter, we find that Eq. (19) becomes

$$\frac{dn}{dt} = \sum_{\vec{k}} \left(\frac{\partial f_{c\Gamma}(\vec{k})}{\partial t}\right)_{other} + \sum_{\vec{k}} \sum_{j} \left(\frac{\partial f_{cj}(\vec{k})}{\partial t}\right)_{other}. \tag{44}$$

Equations (20), (21), and (22) are still correct, but Eq. (23), with the help of Eq. (44), now reads

$$\rho_{FE} \cdot \frac{dE_F}{dt} + \rho_{TE} \cdot \frac{dT}{dt} = \sum_{\vec{k}} \left(\frac{\partial f_{c\Gamma}(\vec{k})}{\partial t}\right)_{other} + \sum_{\vec{k}} \sum_{j} \left(\frac{\partial f_{cj}(\vec{k})}{\partial t}\right)_{other}. \tag{45}$$

The Fermi energies E_F and E_h are still related through the electron number as required by Eq. (27), that is,

$$\frac{dE_h}{dt} = -\gamma_{HE} \frac{dE_F}{dt} + \gamma_{HT} \frac{dT}{dt}. \tag{46}$$

The basic equation for the energy of the carriers after the excitation

pulse passes is

$$\frac{du}{dt} = \left(\frac{\partial u}{\partial t}\right)_{REL} + \left(\frac{\partial u}{\partial t}\right)_{other}. \tag{47}$$

For the moment, we ignore the "other" contributions to the equations. The only contributions remaining are the intravalley phonon-assisted relaxation terms. These relaxation terms do not change the electron number whatsoever. We write

$$\left(\frac{dn}{dt}\right)_{REL} = 0 = \left(\frac{\partial n}{\partial T}\right)_{E_F}\left(\frac{dT}{dt}\right)_{REL} + \left(\frac{\partial n}{\partial E_F}\right)_{T}\left(\frac{dE_F}{dt}\right)_{REL}. \tag{48}$$

Using definitions (21) and (22) in Eq. (48), we obtain

$$\left(\frac{dE_F}{dt}\right)_{REL} = -\frac{\rho_{TE}}{\rho_{FE}}\left(\frac{dT}{dt}\right)_{REL} = -\gamma_{FE}\left(\frac{dT}{dt}\right)_{REL} \tag{49}$$

where

$$\gamma_{FE} \equiv \frac{\rho_{TE}}{\rho_{FE}} = \frac{(\partial n/\partial T)_{E_F}}{(\partial n/\partial E_F)_T}. \tag{50}$$

Similarly, for the holes

$$\left(\frac{dE_h}{dt}\right)_{REL} = \gamma_{FH}\left(\frac{dT}{dt}\right)_{REL} \tag{51}$$

where

$$\gamma_{FH} \equiv -\frac{(\partial n/\partial T)_{E_h}}{(\partial n/\partial E_h)_T}. \tag{52}$$

Equations (46) and (49) are the basic coupled differential equations for determining the time behavior of the electron and hole Fermi energies, E_F and E_h, in terms of the temperature, T, for intravalley phonon-assisted relaxation. Expressions for γ_{FE} and γ_{FH} are

easily obtained by performing the indicated partial differentiations on Eqs. (10) and (13). γ_{FE} is a measure of the change in electron Fermi energy with temperature under the constraint of constant electron density. A similar statement applies for γ_{FH}. The behavior of E_F, E_h, and T during phonon-assisted intraband relaxation processes will be entirely determined if we can obtain an expression for the time behavior of T alone. We now consider the electron and hole energies.

The time rate of change of the combined electron and hole energy may be written

$$\left(\frac{du}{dt}\right)_{REL} = \left(\frac{du_e}{dt}\right)_{REL} + \left(\frac{du_h}{dt}\right)_{REL}. \tag{53}$$

The electron energy u_e and the hole energy u_h obey the following differential equations:

$$\left(\frac{du_e}{dt}\right)_{REL} = \left(\frac{\partial u_e}{\partial T}\right)_{E_F}\left(\frac{dT}{dt}\right)_{REL} + \left(\frac{\partial u_e}{\partial E_F}\right)_{T}\left(\frac{dE_F}{dt}\right)_{REL} \tag{54}$$

and

$$\left(\frac{du_h}{dt}\right)_{REL} = \left(\frac{\partial u_h}{\partial T}\right)_{E_h}\left(\frac{dT}{dt}\right)_{REL} + \left(\frac{\partial u_h}{\partial E_h}\right)_{T}\left(\frac{dE_h}{dt}\right)_{REL}. \tag{55}$$

Using Eq. (49), we find that Eq. (54) becomes

$$\left(\frac{du_e}{dt}\right)_{REL} = \left[\left(\frac{\partial u_e}{\partial T}\right)_{E_F} - \gamma_{FE}\left(\frac{\partial u_e}{\partial E_F}\right)_{T}\right]\left(\frac{dT}{dt}\right)_{REL}. \tag{56}$$

We define

$$\gamma_{UE} \equiv \left(\frac{\partial u_e}{\partial T}\right)_{E_F} - \gamma_{FE}\left(\frac{\partial u_e}{\partial E_F}\right)_{T}. \tag{57}$$

The equation for the time rate of change of the electron energy during intravalley relaxation, Eq. (56), becomes

$$\left(\frac{du_e}{dt}\right)_{REL} = \gamma_{UE}\left(\frac{dT}{dt}\right)_{REL} \tag{58}$$

and, similarly, Eq. (55) becomes

$$\left(\frac{du_h}{dt}\right)_{REL} = \gamma_{UH}\left(\frac{dT}{dt}\right)_{REL} \tag{59}$$

where

$$\gamma_{UH} \equiv \left(\frac{\partial u_h}{\partial T}\right)_{E_H} + \gamma_{FH}\left(\frac{\partial u_h}{\partial E_H}\right)_T . \tag{60}$$

Combining Eqs. (58) and (59), we find that

$$\left(\frac{dT}{dt}\right)_{REL} = \frac{1}{\gamma_{UE} + \gamma_{UH}}\left[\left(\frac{du_e}{dt}\right)_{REL} + \left(\frac{du_h}{dt}\right)_{REL}\right] . \tag{61}$$

Notice that γ_{UE} (γ_{UH}) represents the change in electron (hole) energy with respect to temperature during intravalley relaxation. Explicit expressions for γ_{UE} and γ_{UH} are easily obtained since they involve only partial differentiations of the expressions for carrier number and carrier energy [Eqs. (10), (13), and (34)].

Equations (46), (49), and (61) constitute a set of coupled, first-order linear differential equations that determine the time evolution of the Fermi energies of the electrons and holes and the time evolution of the distribution temperature during intravalley relaxation. As discussed earlier, this is the only process of any consequence after the first pulse ceases to interact with the sample.

Since the energy relaxation terms on the right-hand side of Eq. (61) dominate the behavior of the probe pulse transmission, they are calculated in Appendix C. This perturbation calculation should serve as a model for performing the other scattering calculations that have been mentioned throughout this chapter.

Although we have argued that the "other" contributions to the change in carrier number, Fermi energy, and temperature are negligible, their contributions may be accounted for in the following way. We assume that the change in temperature with time is dominated by the intravalley relaxation processes. That is

$$\frac{dT}{dt} = \left(\frac{dT}{dt}\right)_{REL} + \left(\frac{dT}{dt}\right)_{other} \simeq \left(\frac{dT}{dt}\right)_{REL}. \tag{62}$$

This means that Eq. (61) will not need to be modified in the presence of "other" terms, such as diffusion, radiative recombination, and non-radiative recombination. This is a reasonable approximation since the primary effect of each of these terms is to reduce the carrier number by a small amount. We may express this reduction of the electron number as

$$\frac{dn}{dt} = \left(\frac{dn}{dt}\right)_{REL} + \left(\frac{dn}{dt}\right)_{other} = \left(\frac{dn}{dt}\right)_{other}. \tag{63}$$

Then, using Eq. (62), we obtain

$$\begin{aligned}\left(\frac{dn}{dt}\right)_{other} &= \left(\frac{\partial n}{\partial E_F}\right)_T \left(\frac{dE_F}{dt}\right)_{other} + \left(\frac{\partial n}{\partial T}\right)_{E_F} \left(\frac{dT}{dt}\right)_{other} \\ &\simeq \left(\frac{\partial n}{\partial E_F}\right)_T \left(\frac{dE_F}{dt}\right)_{other}.\end{aligned} \tag{64}$$

Rearranging we find that

$$\left(\frac{dE_F}{dt}\right)_{other} = \gamma_{RD}\left(\frac{dn}{dt}\right)_{other} \tag{65}$$

where

$$\gamma_{RD} \equiv \frac{1}{(\partial n/\partial E_F)_T} \, . \tag{66}$$

Thus, to account for the small effect of the "other" terms on electron Fermi energy, we simply add Eq. (49) to Eq. (65) to obtain

$$\frac{dE_F}{dt} = -\gamma_{FE}\left(\frac{dT}{dt}\right)_{REL} + \gamma_{RD}\left(\frac{dn}{dt}\right)_{other} . \tag{67}$$

The decrease in carrier number with time due to diffusion can be calculated from the Boltzmann equation. The decrease due to radiative and nonradiative recombination can be calculated using perturbation theory.

Equations (46), (61), and (67) constitute a more rigorous set of equations that determine the evolution of the carrier distribution as a function of time.

In summary, the excitation pulse interacts with the sample creating a large number of electron-hole pairs with a high distribution temperature, as outlined by the equations of the previous section. The electron and hole Fermi energies and distribution temperature at the end of the excitation pulse serve as the initial values for the equations of the present section. Equations (46), (61), and (67) then describe the time evolution of the Fermi distributions of the electrons and holes when no optical field is present. For convenience, we again

write these equations:

$$\frac{dE_h}{dt} = -\gamma_{HE}\frac{dE_F}{dt} + \gamma_{HT}\frac{dT}{dt} \tag{46}$$

$$\left(\frac{dT}{dt}\right) = \frac{1}{\gamma_{UE} + \gamma_{UH}}\left[\left(\frac{du_e}{dt}\right)_{REL} + \left(\frac{du_h}{dt}\right)_{REL}\right] \tag{61}$$

$$\frac{dE_F}{dt} = -\gamma_{FE}\left(\frac{dT}{dt}\right)_{REL} + \gamma_{RD}\left(\frac{dn}{dt}\right)_{other}. \tag{67}$$

For times from 0 to 300 psec, the electron number remains relatively constant. The evolution of the Fermi distributions during this time is determined by the intravalley relaxation of the electrons and holes by means of phonon emission. The probe transmission samples this distribution relaxation. The coupling of the probe pulse to the electron distribution is described below.

The probe pulse is depleted by both direct absorption and free carrier absorption events. Changes in either the direct or free carrier absorption coefficients will result in a change in the probe transmission. The following rate equation describes the relationship between the probe pulse energy density and the absorption coefficients:

$$\frac{dW}{dt} = -[\alpha_{DA} + \alpha_{FCA}]W, \tag{68}$$

where α_{DA} and α_{FCA} represent the direct and free carrier absorption coefficients. W represents the energy density of the probe pulse in the crystal. We assume that the carrier distribution is not perturbed by the presence of the probe pulse.

Expressions for the absorption coefficients in terms of E_F, E_H, and T are then obtained from perturbation theory through the following expressions:

$$\sum_{\vec{k}} \left(\frac{\partial f_{c\Gamma}(\vec{k})}{t}\right)_{DA} = \left(\frac{W}{N_0 h\omega_0}\right)\alpha_{DA}(E_F, E_h, T) \tag{69}$$

and

$$\sum_{\vec{k}}\sum_{j}\left(\frac{\partial f_{cj}(\vec{k})}{\partial t}\right)_{FCA} + 2\sum_{\vec{k}}\left(\frac{\partial f_h(\vec{k})}{\partial t}\right)_{FCA} = \frac{W}{\hbar\omega_0 N_0}\alpha_{FCA}(E_F, E_h, T). \tag{70}$$

These equations emphasize that as the electron and hole Fermi energies and distribution temperature change with time so do the free carrier and direct absorption coefficients. This change in absorption coefficients is reflected in the change in probe pulse transmission through Eq. (68).

Since the carrier distributions evolve primarily through intravalley phonon-assisted relaxation, the observed increase in probe transmission reported in the previous chapter is an indication of this relaxation time.

If one performs the indicated perturbation calculations and evaluates all of the ρ's, γ's, and α's defined in this chapter, one obtains the final equations presented in Appendix D. These equations describe the probe transmission as a function of time delay after the excitation pulse. The results of numerically evaluating these equations are presented in the next chapter.

In Chapter 5, we emphasize only the time behavior of the probe pulse transmission, given that the excitation pulse creates a certain

number of carriers with a certain distribution temperature. The numerical results of calculations describing the evolution of the Fermi distribution during the interaction of the excitation pulse with the crystal are discussed by Matter (1975).

CHAPTER 5

NUMERICAL ANALYSIS

In this chapter we present the results of numerically integrating the equations of Appendix D. These equations are obtained by completing the calculations outlined in Chapter 4. We also compare the theoretical results with the experimental results of Chapter 3.

Excitation Pulse Results

In this work, we have emphasized the evolution of the carrier distribution with time after the passage of the excitation pulse. However, since the interaction between the excitation pulse and germanium sample determines the initial carrier distribution at time t = 0, we will make some general comments on the numerical single pulse results.

Figure 13 is a plot of excitation pulse transmission versus pulse energy for two temperatures, 105 K and 197 K. This figure contains both the theoretical curves and the experimental data. The detailed single pulse equations as well as a more complete discussion of the single pulse results may be found in Matter (1975). The values taken for the various physical parameters that enter both the single pulse and excitation-probe equations are listed at the end of Appendix D.

In terms of the model presented in Chapter 4, the behavior of the single pulse transmission may be accounted for by direct interband transitions followed by heating of the electron distribution. For

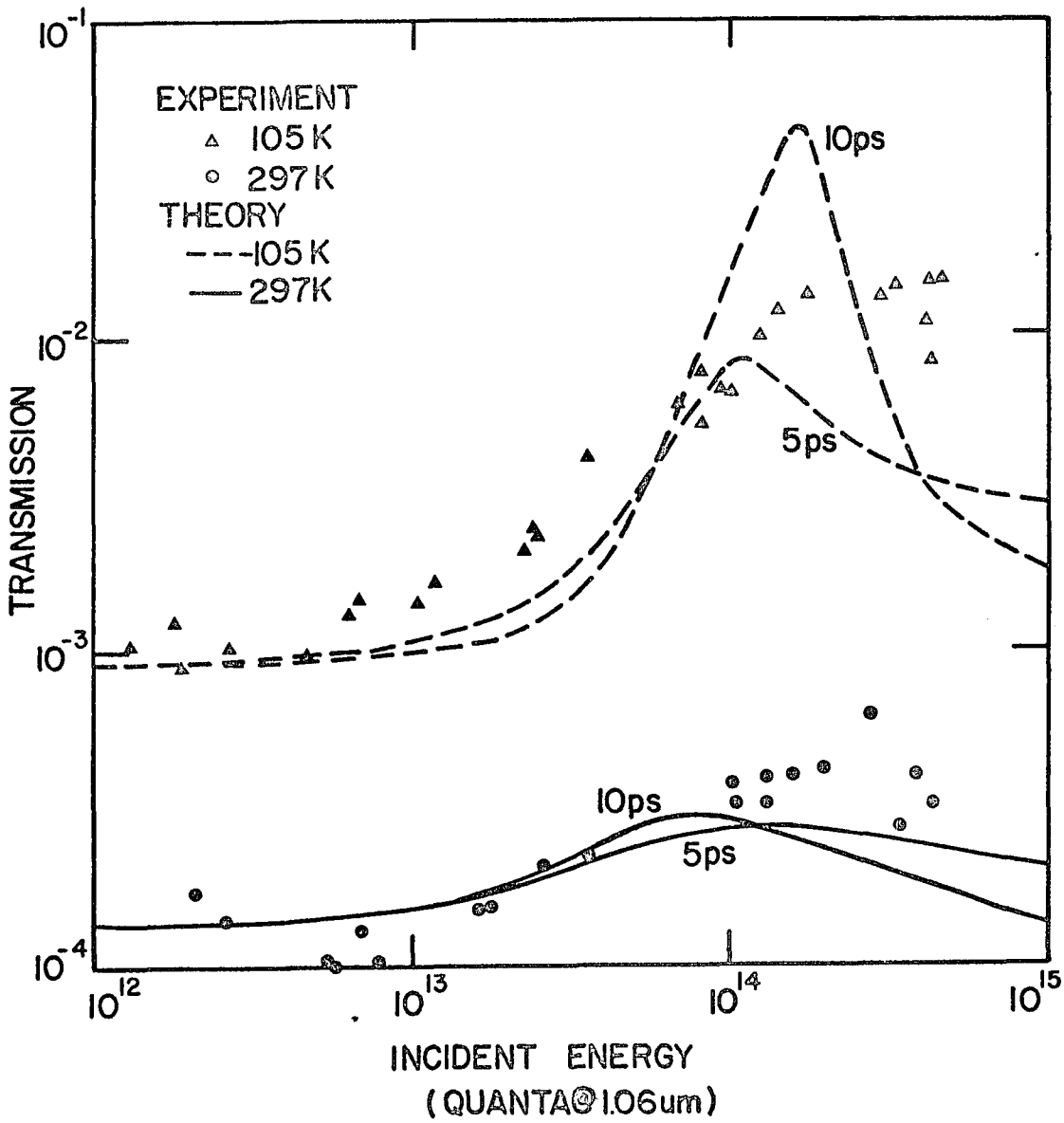

Fig. 13. Single Pulse Transmission of a 5.5 μm Thick Single Crystal Germanium Sample Versus Incident Energy in Units of Quanta at 1.06 μm.

The theoretical curves are for pulse widths of 5 psec and 10 psec.

energies less than 10^{13} quanta (sample interaction volume is approximately 10^{-6} cm^3), the transmission follows Beer's law. For intermediate pulse energies of 10^{13} to 10^{14} quanta, the transmission rises due to the saturation of the available optically coupled electronic states by means of direct absorption. Due to the rapid nature of phonon-assisted intervalley scattering, saturation of the optically coupled states in the Γ-valley also requires a saturation of the states in the side valleys of the conduction band. Further increase in the transmission, for energies larger than 10^{14} quanta, is prevented as the electrons are heated and removed from the optically coupled states by an increase in distribution temperature. The electrons are heated by free carrier absorption and by plasma recombination as discussed in Chapter 4. Similar arguments apply to the hole distribution in the valence band. For energies above 5×10^{14} quanta the crystal is damaged.

In addition to its role in raising the distribution temperature, nonradiative plasma recombination is the dominant mechanism for determining the maximum density of carriers present after the passage of the intense excitation pulse. Recall that when the plasma frequency is energetically near the direct gap energy E_0 or the indirect gap energy E_G, electrons and holes can recombine while simultaneously emitting plasmons. The plasmons then rapidly decay, transferring their energy to single electron-hole states, and ultimately serve to increase the temperature of the carrier distribution. As the number of carriers increases, the plasma frequency increases. When the plasmon energy is near the direct band gap, the nonradiative recombination rate becomes

comparable to the direct absorption rate, thus limiting the density of electron-hole pairs.

There are several features of the data in Fig. 13 that may be accounted for by the presence of nonradiative recombination. First, consider that the band gap of germanium for a sample temperature of 105 K is higher than for a sample temperature of 297 K. Thus, the plasmon energy becomes comparable to the direct band gap at a lower carrier density for a sample temperature of 297 K than for a sample temperature of 105 K. As a result, the nonradiative recombination restricts the final carrier density to a lower value for the higher sample temperature (see Table 1). For a given excitation pulse energy, restricting the carrier density to a lower value for the higher sample temperature requires that more plasma recombinations take place; thus, the distribution temperature will be higher for the higher sample temperature (see Table 1). We then conclude that for a given incident pulse energy there will be a larger density of carriers with a lower distribution temperature at a sample temperature of 105 K than at 297 K. This larger number of carriers located lower in the band accounts for the greater degree of saturation at 105 K (see Fig. 13).

The shape of the transmission saturation is very sensitive to the pulse width (and shape), as illustrated by the theoretical curves of Fig. 13: one set for a pulse width of 10 psec and one for 5 psec. This is because the phonon-assisted electron relaxation time is of the order of the pulse width. Thus, the electrons cool even during the short time the excitation pulse is present. There is, however,

Table 1. Initial Conditions for Probe Transmission after the Passage of a 1.6×10^{14} Quanta Excitation Pulse.

Parameter	Temperature (K) 105	200	297
Linear absorption coefficient (cm^{-1})	1.11×10^4	1.29×10^4	1.46×10^4
Indirect band gap (eV)	0.763	0.732	0.700
Direct band gap (eV)	0.872	0.836	0.799
Distribution temperature (K)	980	2,124	3,108
Electron density (cm^{-3})	6.9×10^{19}	4.9×10^{19}	4.0×10^{19}
Electron Fermi energy	0.71	0.27	-0.12
Hole Fermi energy	-0.04	0.20	0.57

considerably more time for the relaxation of the distribution temperature during the 10 psec pulse than during the 5 psec pulse. The exact width of each pulse from the laser is unknown, but it is between 5 and 15 psec in duration, depending on the portion of the pulse train from which it is selected.

Probe Pulse Results

The temperature of the germanium sample and the energy of the excitation pulse determine the initial carrier distributions and, thus, the initial transmission of the probe pulse (we assume for the remainder

of this discussion that the pulse width remains constant at 5 psec). The rise and fall observed in the probe pulse transmission as a function of time is due to the temperature relaxation of these electron and hole distributions by means of phonon emission as described in detail in the previous chapter. Briefly, the probe pulse transmission initially increases as the electrons, heated by the excitation pulse, cool and fill the electronic states needed for absorption. Because the states that are optically coupled lie at some energy above the bottom of the conduction band, further cooling of the electron distribution will remove the electrons from these states resulting in a decrease in transmission. Similar arguments hold for holes in the valence band.

Since the initial conditions depend only on the sample temperature and excitation pulse energy (assuming a constant pulse shape), we discuss first the behavior of the probe pulse transmission as the temperature of the germanium is varied and the excitation pulse energy remains constant at 1.6×10^{14} quanta. Next we vary the excitation energy while holding the temperature constant.

Throughout the probe studies, the decrease in electron number due to radiative recombination, nonradiative recombination, and diffusion is negligible. For all practical purposes, the electron number remains constant.

Values for the distribution temperature, carrier density, and electron and hole Fermi energies after the passage of an excitation pulse containing 1.6×10^{14} quanta are given in Table 1 for three sample temperatures. These serve as the initial values for the equations in

Appendix D. In addition, values for the linear absorption coefficient, indirect band gap, and direct band gap are also given for these three temperatures. The values for the location of the conduction band valleys in energy have been given in the previous chapter. The linear absorption coefficients and other relevant physical constants are given in Appendix D.

Notice in Table 1 that the electron density is higher and the distribution temperature lower for 105 K than for 297 K, in agreement with the arguments of the previous section.

Figure 14 is a computer-generated plot of normalized probe transmission versus probe delay for three sample temperatures: 105 K, 200 K, and 297 K. The excitation pulse energy is 1.6×10^{14} for each curve; the initial values for the carrier distributions for these curves are given in Table 1. For curve I, the sample temperature is 105 K; for curve II, 200 K; for curve III, 297 K. Notice that the transmission of curve I peaks at a delay of approximately 109 psec, curve II at a delay of 123 psec, and curve III at a delay of 137 psec. If the rise time is defined as the time required for the transmission to reach half its maximum value, the rise times are 21, 29, and 20 psec for curves I, II, and III, respectively.

The time behavior of the probe pulse transmission is determined by the temperature relaxation of the initial carrier distributions. The computer-generated curves of distribution temperature and electron Fermi energy versus time are shown in Fig. 15. The distribution temperature relaxation curves (I, II, III) of this figure correspond to the same

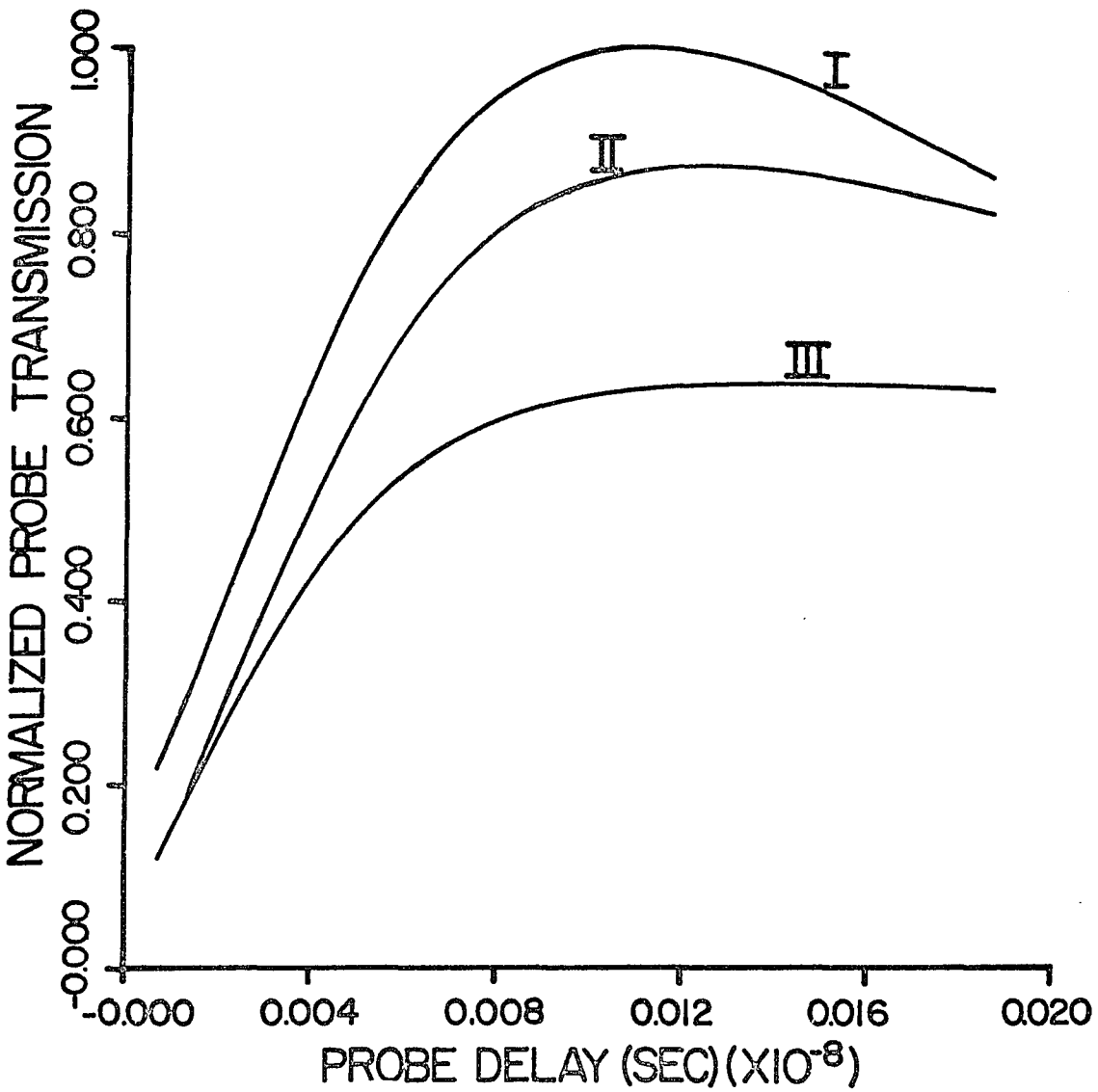

Fig. 14. Theoretical Normalized Ratio of Probe Pulse Transmission to Excitation Pulse Transmission Versus Time Delay of Probe with Respect to an Excitation Pulse of Energy 1.6×10^{14} Quanta for Sample Temperatures of 105 K (I), 200 K (II), and 297 K (III).

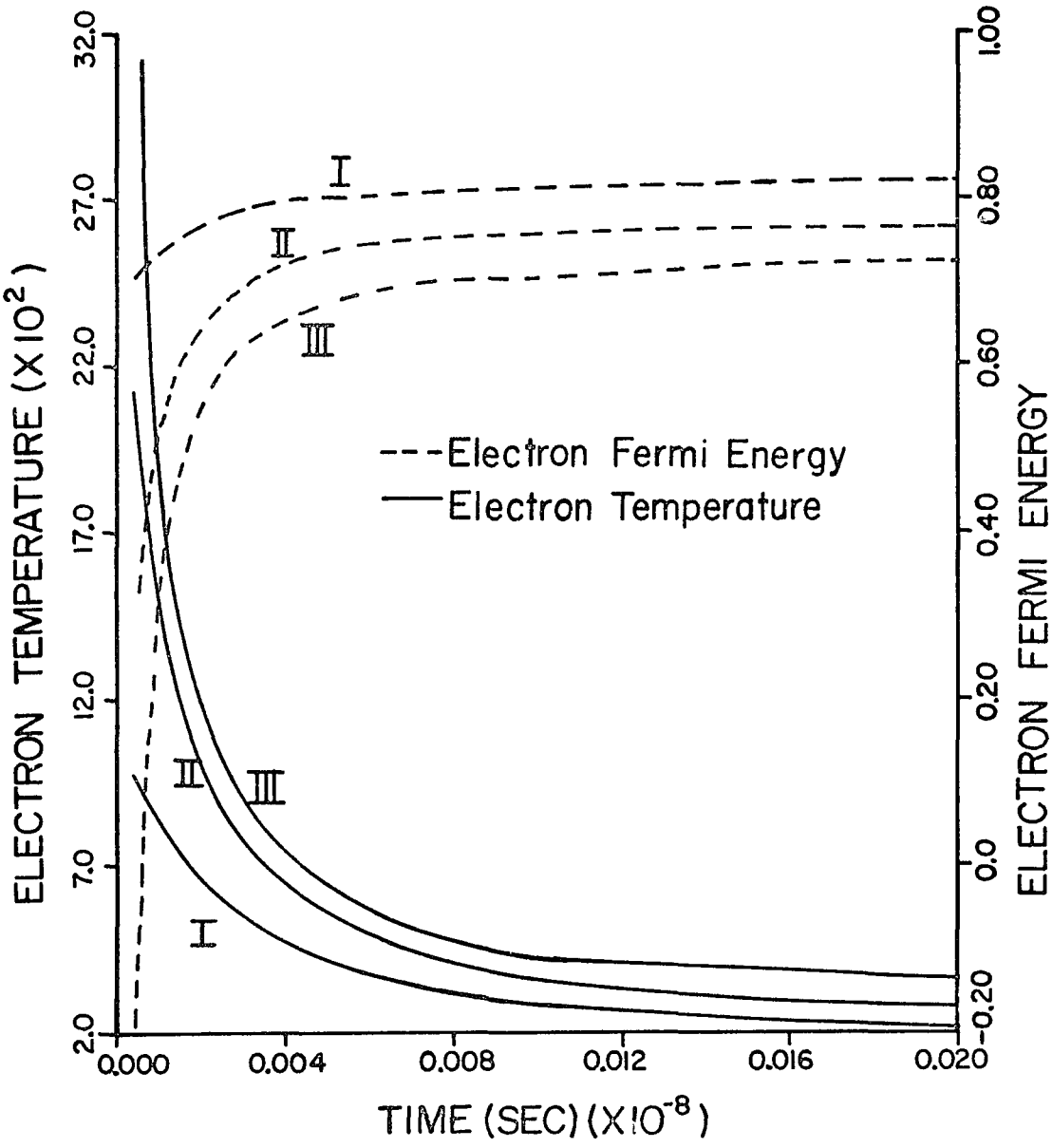

Fig. 15. Theoretical Electron Distribution Temperature in Degrees Kelvin and Electron Fermi Energy in Electron Volts Versus Time in Seconds after an Excitation Pulse of Energy 1.6 x 10^{14} Quanta for Sample Temperatures of 105 K (I), 200 K(II), and 297 K (III).

initial conditions and sample temperatures as the curves (I, II, III) of Fig. 14. Notice that the time required for the electron temperature to relax to half its initial value is 45 psec for a sample temperature of 105 K, 18 psec for 200 K, and 16 psec for 297 K. This is due to the factor $(T - T_0)$ in Eq. (C-26). That is, the rate of decay of the distribution temperature is proportional to the difference between the distribution temperature and the lattice temperature; curve I will relax slower than II or III since it has the lowest initial distribution temperature.

One might be tempted to conclude, since the temperature decay time for curve I of Fig. 15 is slower than that for curves II or III, that the transmission of curve I of Fig. 14 should rise more slowly than that of curves II and III of the same figure. This is not the case due to the fact that, although the electrons relax more slowly when the lattice temperature is 105 K than when it is 297 K, they do not have to relax as far before clogging the states which are optically coupled. Thus, the transmission rise times for different sample temperatures are not drastically different.

We also notice (Fig. 14) that the increase in probe transmission is larger for lower sample temperatures. This is because the cooler sample has a larger carrier population after the passage of the first pulse. The larger the carrier population, the more completely the carriers, upon "cooling," fill the states to which the probe pulse is optically coupled.

Since the direct absorption coefficient is decreased and the free carrier absorption coefficient increased as the number of

electrons (holes) in the conduction (valence) band is increased, we might wonder whether or not the free carrier coefficient becomes comparable to the direct absorption coefficient at any time. Furthermore, what portion of the free carrier coefficient is due to optical phonons and what portion is due to acoustic phonons? Figure 16 is a plot of the total absorption coefficient versus time after the excitation pulse. Figure 17 displays the direct and free carrier contributions to the total absorption coefficient. The direct absorption coefficient always dominates in germanium. Figure 18 is a plot of the optical phonon-assisted free carrier absorption coefficient and the acoustic phonon-assisted free carrier absorption coefficient versus time. The largest contribution to free carrier absorption is from optical phonon-assisted transitions.

Figure 19 illustrates the general agreement between the theoretical curves and the experimental data for the two sample temperatures, 105 K and 297 K. The fit is good, but not exact. Many of the experimentally measured parameters used in these equations (and listed in Appendix D) are not known with great precision. The relaxation of the carrier temperature is sensitive to several of these parameters. For example, the phonon-assisted intravalley energy relaxation rate is dominated by the optical phonons (see Fig. 18); thus, a small change in the optical phonon-electron coupling constant results in a dramatic change in the electron relaxation rate. This is reflected in the rise times of the probe transmission curves, as illustrated in Fig. 20. We see that the curves may be fitted more exactly by optimizing the choices for this and other physical parameters at our disposal.

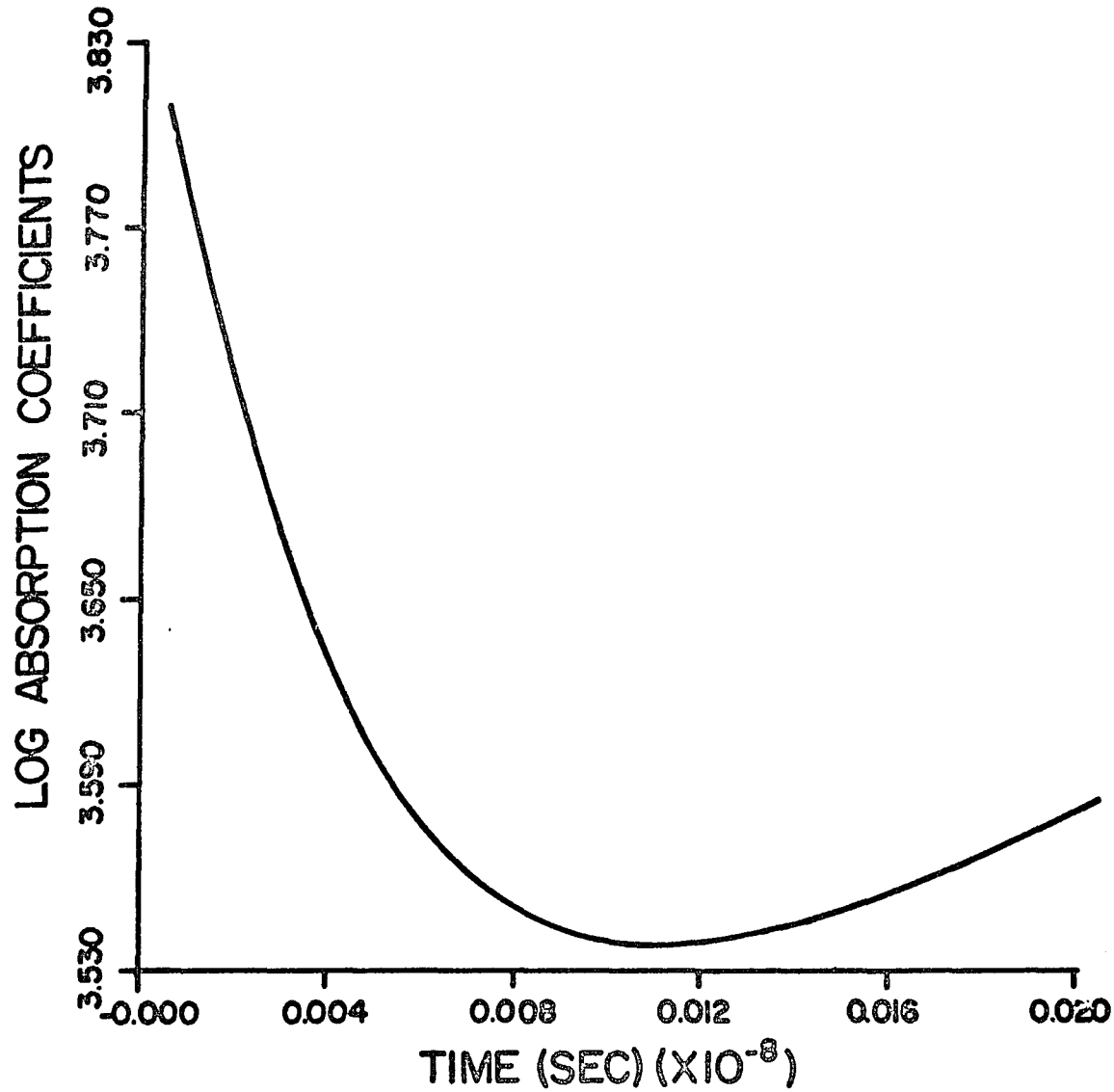

Fig. 16. Theoretical Total Absorption Coefficient (cm^{-1}) Versus Time in Seconds after an Excitation Pulse of Energy 1.6×10^{14} Quanta and for a Sample Temperature of 105 K.

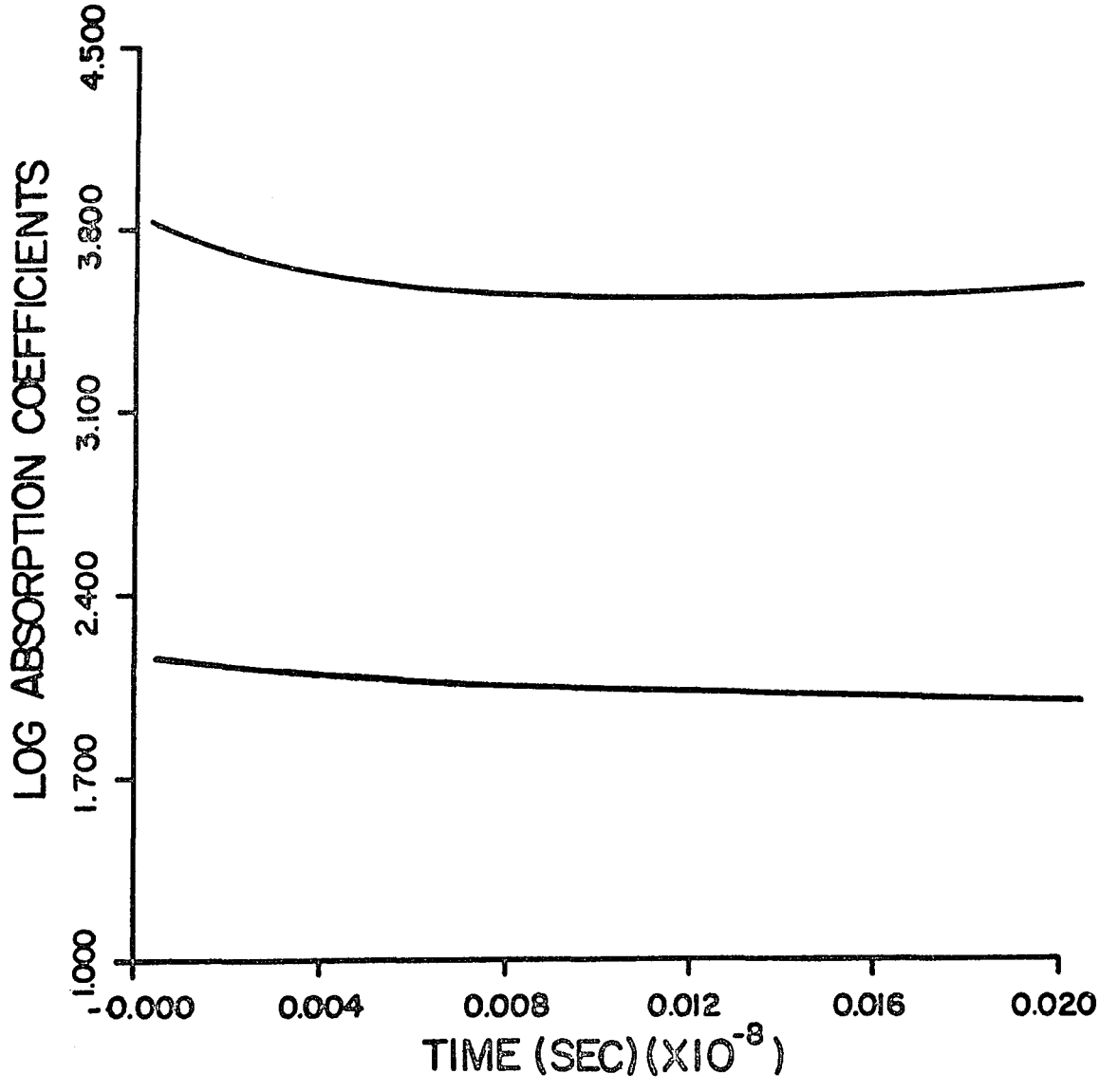

Fig. 17. Theoretical Direct Absorption Coefficient (Upper Curve) and Free Carrier Absorption Coefficient (Lower Curve) Versus Time in Seconds after an Excitation Pulse of Energy 1.6 x 10^{14} Quanta and for a Sample Temperature of 105 K.

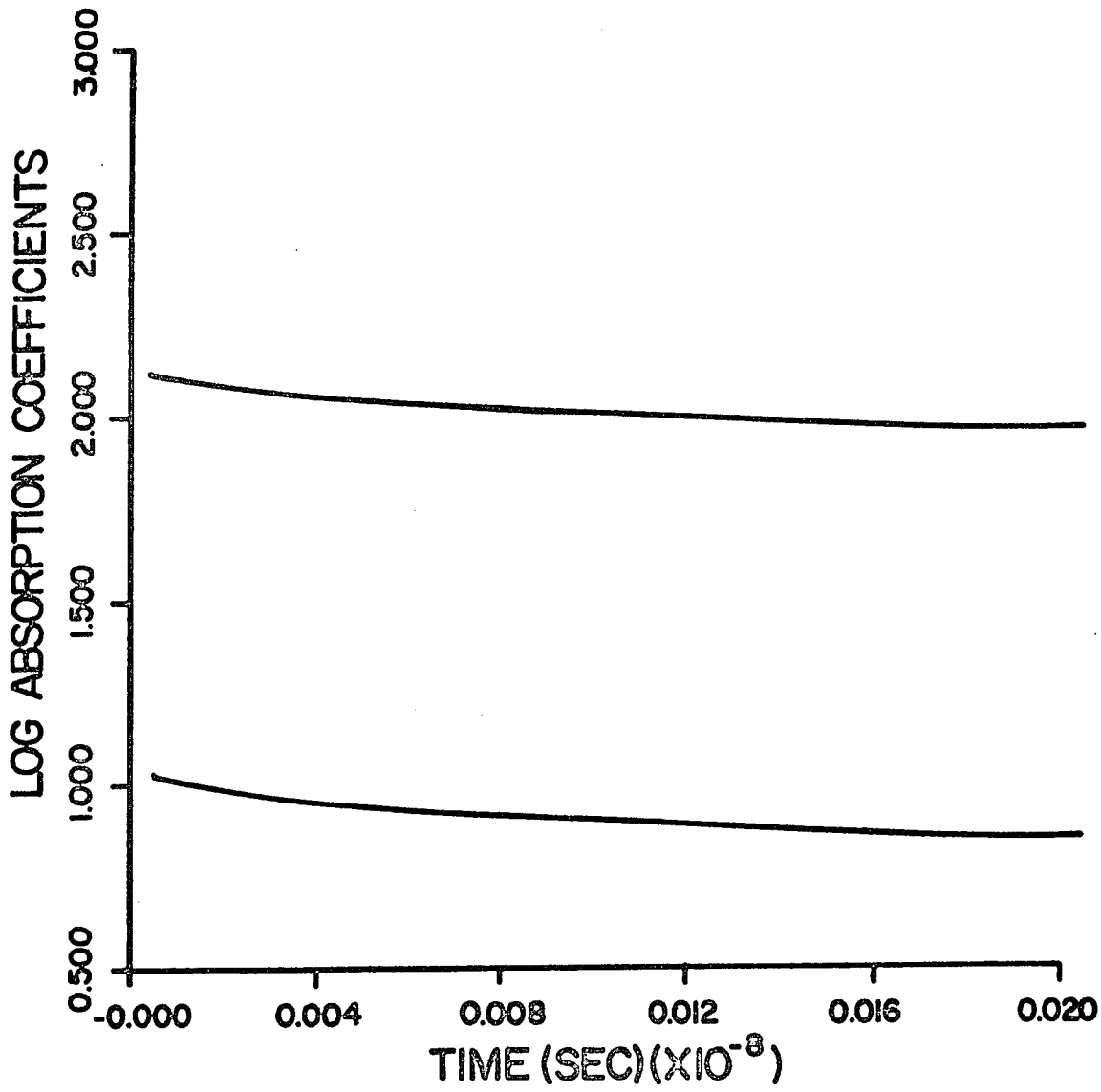

Fig. 18. Theoretical Free Carrier Absorption Coefficient due to Optical Phonons (Upper Curve) and due to Acoustic Phonons (Lower Curve) Versus Time in Seconds after an Excitation Pulse of Energy 1.6 x 10^{14} Quanta and for a Sample Temperature of 105 K.

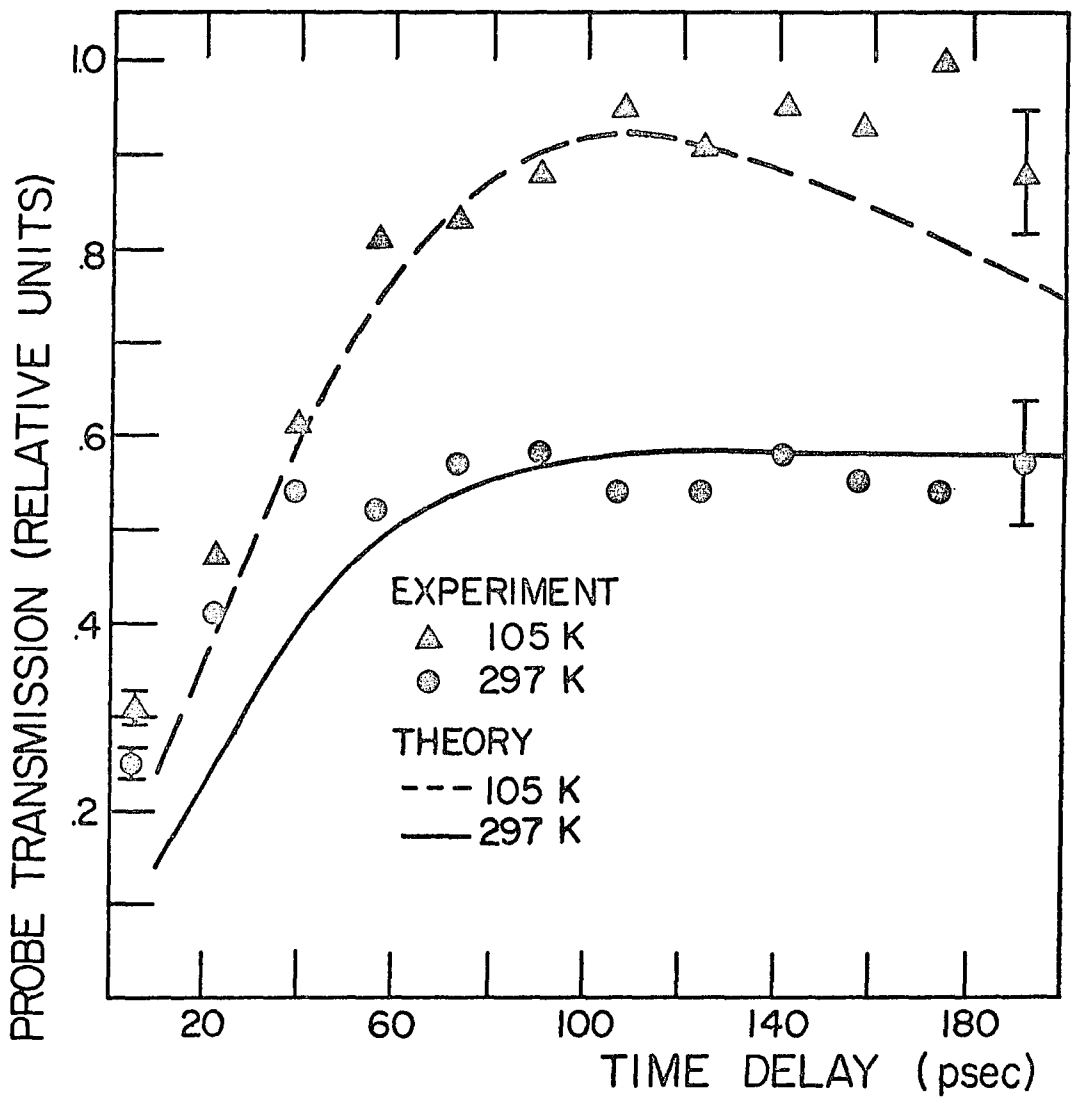

Fig. 19. Comparison of the Theoretical and the Experimental Normalized Ratio of Probe Pulse Transmission to Excitation Pulse Transmission Versus Time Delay of Probe with Respect to an Excitation Pulse of Energy 1.6×10^{14} Quanta.

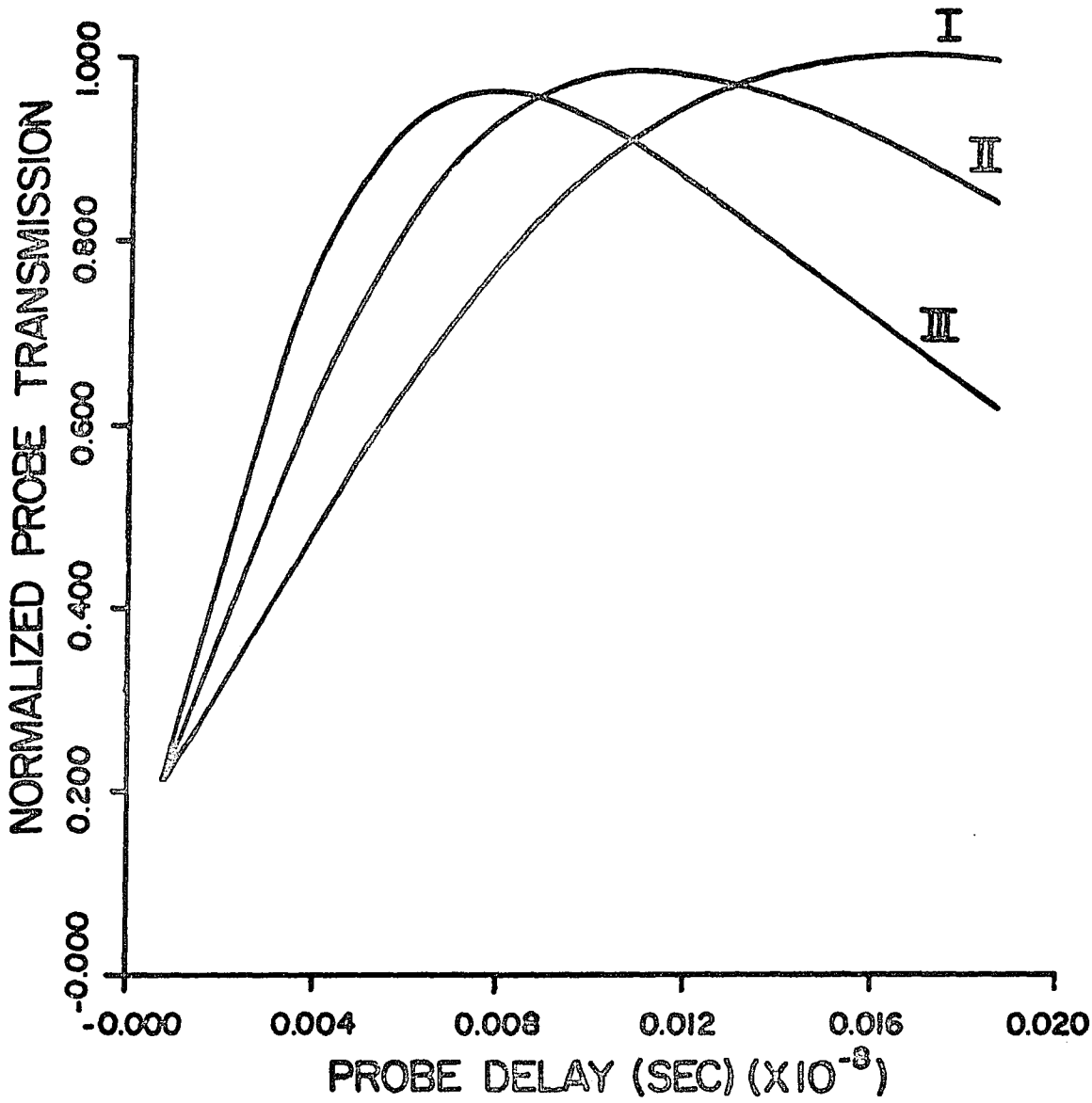

Fig. 20. Theoretical Normalized Ratio of Probe Pulse Transmission to Excitation Pulse Transmission Versus Time Delay of Probe with Respect to an Excitation Pulse of Energy 1.6×10^{14} Quanta for a Sample Temperature of 105 K and Three Optical Phonon-Electron Coupling Constants: 2.0×10^{-3} (I), 2.5×10^{-3} (II), and 3.0×10^{-3} erg cm^{-1} (III).

We now present the numerical results of probe pulse transmission calculations where the initial carrier distributions are determined by varying the excitation energy while holding the sample temperature constant. Figure 21 is a plot of normalized probe transmission versus delay for four different excitation energies: 6.3×10^{13}, 1.0×10^{14}, 1.6×10^{14}, and 4.0×10^{14} quanta. The sample temperature is 105 K.

The more quanta a pulse contains, the higher the direct absorption rate and the larger the carrier density. The larger carrier density means a larger plasma recombination rate and a larger free carrier absorption rate. Both plasma recombination and free carrier absorption serve to raise the distribution temperature; thus, the more energetic excitation pulses result in a higher distribution temperature and a larger carrier density. The electrons elevated high in the conduction band by the excitation pulse relax after the passage of the first pulse by means of phonon-assisted intravalley scattering processes. The electrons located high in the band relax at a faster rate than those located near the bottom of the band (again, note the $(T - T_0)$ dependence of Eq. (C-26)); however, the electrons located high in the band have to "cool" by a larger amount that those located low in the band in order to saturate the states needed for direct absorption of the probe pulse. Similar arguments apply for the holes in the valence band. Thus, one does not expect the rise times of the curves in Fig. 21 to necessarily be radically different. Also, note that since the larger excitation pulses create the larger carrier densities, they will lead to a larger transmission increase when the carriers relax. Thus, the transmission is more completely saturated for curve I of Fig. 21 than for curve IV.

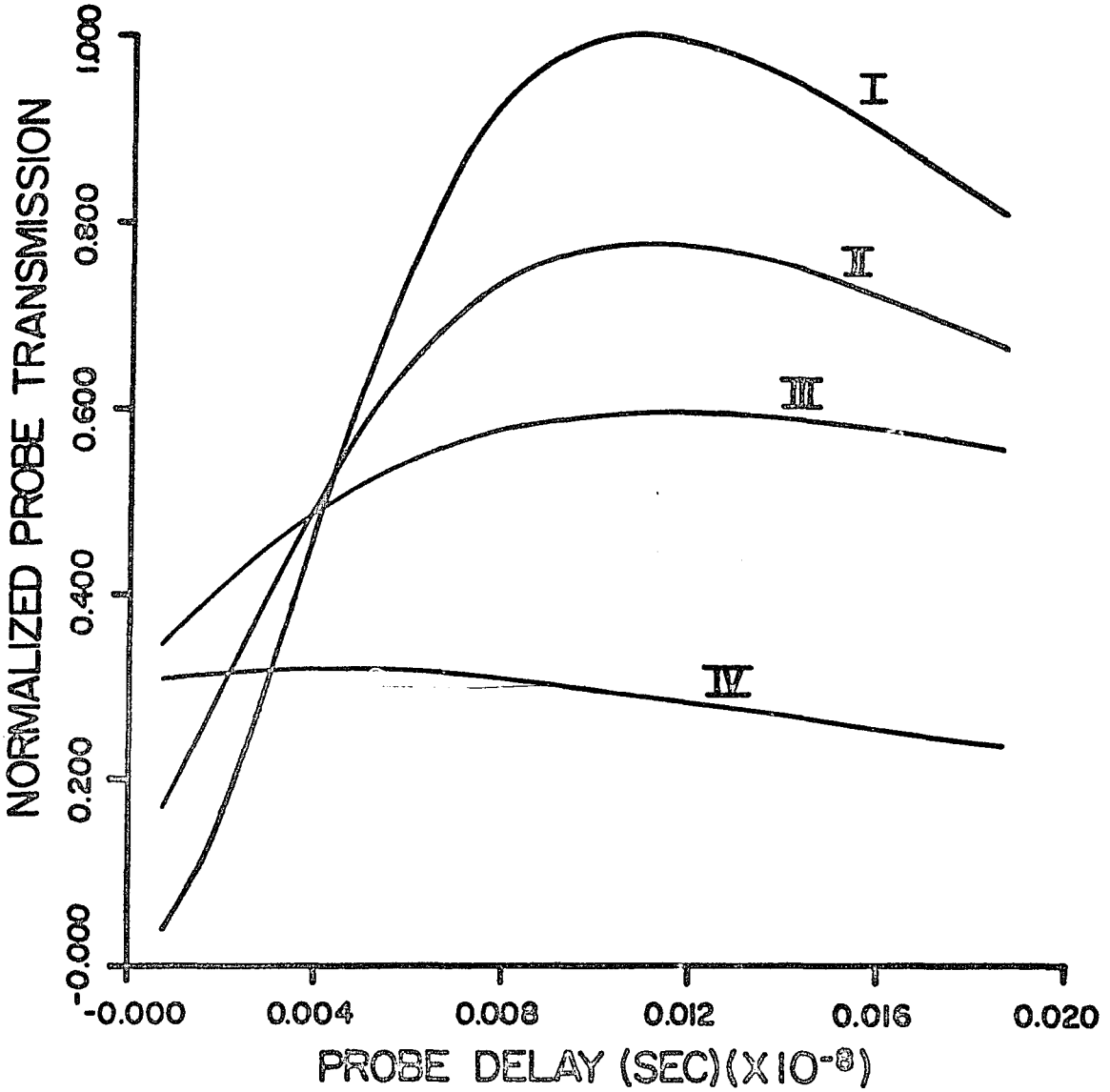

Fig. 21. Theoretical Normalized Ratio of Probe Pulse Transmission to Excitation Pulse Transmission Versus Time Delay of Probe with Respect to an Excitation Pulse of Energy 4.0×10^{14} (I), 1.6×10^{14} (II), 1.0×10^{14} (III), or 6.3×10^{13} (IV) Quanta for a Sample Temperature of 105 K.

Figure 22 presents the same information as Fig. 21 except that the sample temperature is 297 K.

Here we comment on the fact that in the first published account of our work we reported only the "beam clashing" spike near zero probe pulse delay (Kennedy et al., 1974). Notice both theoretically (Fig. 21) and experimentally (Fig. 10) that, as the intensity of the excitation pulse is reduced, the structure in the plot of probe transmission versus delay quickly disappears. The data appearing in our first paper (Kennedy et al., 1974) were obtained with a slightly different size for the focused optical sopt on the sample than later data. Also, the germanium sample was thicker. Both of these effects serve to enlarge the interaction region of the sample and thus to reduce the number of quanta per unit volume per unit time that are present in the sample. It is conceivable, then, that our optical spot size and thickness were such that our curve was flat except for the "beam clashing." Since it is now impossible to recreate those exact conditions, we cannot verify these conjectures.

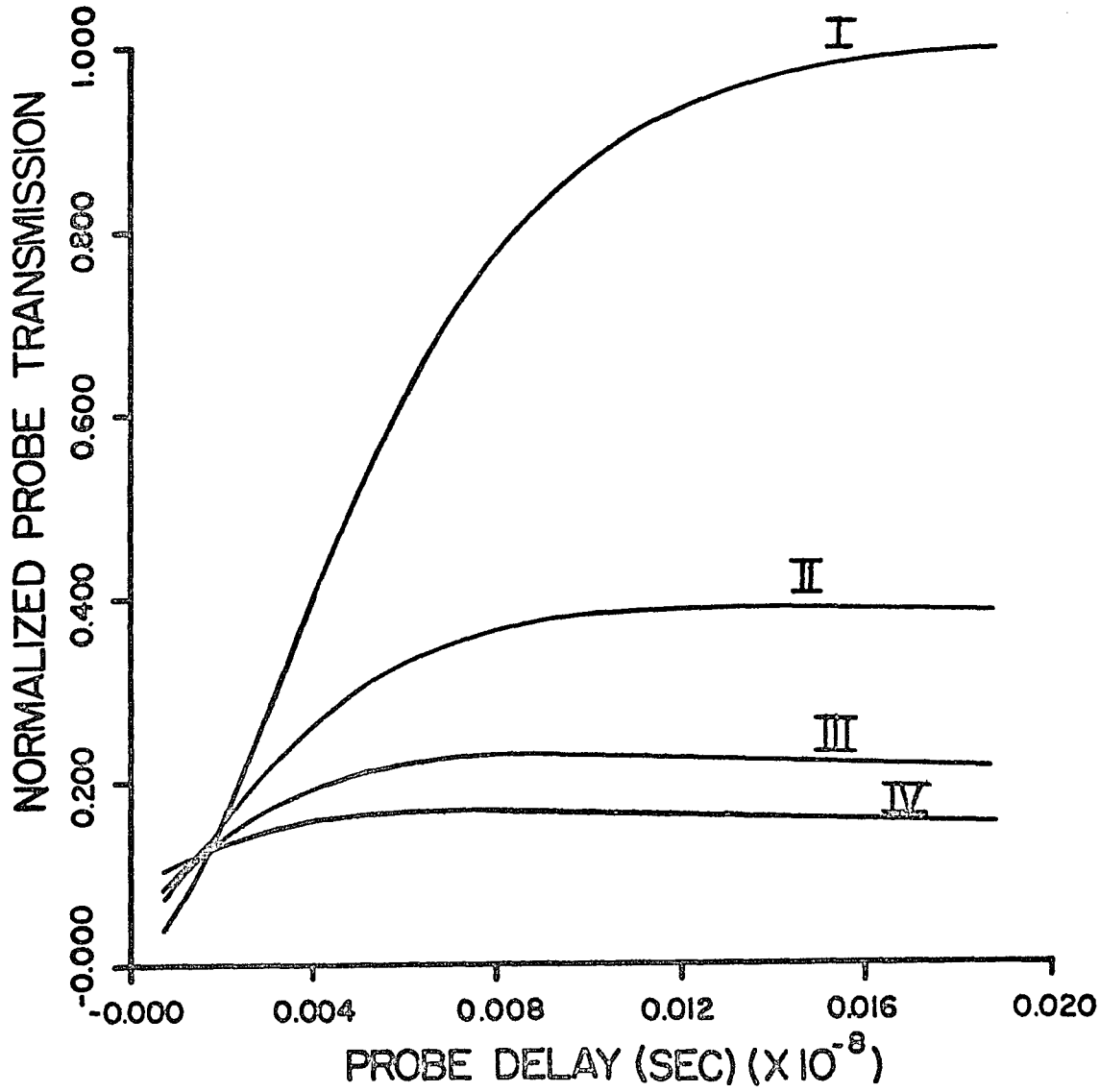

Fig. 22. Theoretical Normalized Ratio of Probe Pulse Transmission to Excitation Pulse Transmission Versus Time Delay of Probe with Respect to an Excitation Pulse of Energy 4.0×10^{14} (I), 1.6×10^{14} (II), 1.0×10^{14} (III), or 6.3×10^{13} (IV) Quanta for a Sample Temperature of 297 K.

CHAPTER 6

CONCLUSIONS

We have measured the transmission of germanium at 1.06 μm when irradiated by intense picosecond pulses and have observed a condition of enhanced transmission. For pulse energies between 10^{12} and 10^{13} quanta, the transmission obeys Beer's law. Between 10^{13} and 10^{14} quanta, the transmission increases. For pulse energies larger than 5×10^{14} quanta, the sample damages. These measurements are described in Chapter 3.

We have argued (Chapter 4) that the single pulse transmission of germanium as a function of pulse energy may be accounted for by direct interband transitions followed by heating of the electron distribution in the following way. When the excitation pulse enters the crystal, it is absorbed by direct optical transitions, creating a large number of electrons in the central valley of the conduction band. These electrons are quickly scattered to the side valleys by long wavelength phonons. Particle-particle scattering events ensure that the carrier distributions obey Fermi-Dirac statistics and that both electron and hole distributions have the same temperature. The transmission initially rises due to the saturation of the available optically coupled stated by means of direct absorption. Further increase in the transmission for energies larger than 10^{14} quanta is prevented as the electrons are heated and removed from these states by free carrier absorption and nonradiative recombination. For large excitation pulse energies, nonradiative recombination also limits the carrier number.

The time evolution of the enhanced transmission induced by the excitation pulse was monitored by measuring the transmission of a weak probe pulse that arrived at some controlled time after the excitation pulse. The transmission of the germanium continued to rise for approximately 100 psec after the excitation pulse passed; then the transmission slowly decreased.

The rise and fall observed in the probe transmission are due to the temperature relaxation of the electron and hole distributions by means of phonon emission. The probe pulse transmission initially increases as the electrons, heated by the excitation pulse, cool and fill the electron states needed for absorption. Because the states that are optically coupled lie at some energy above the bottom of the conduction band, further cooling of the electron distribution will remove the electrons from these states resulting in a decrease in transmission.

APPENDIX A

ENERGY MONITORS

When performing experiments that require the use of pulsed lasers, one experimental parameter of frequent interest is the energy in a single pulse. A common method for obtaining this information is shown in Fig. A1. When a light pulse is incident on the photodiode, electron-hole pairs created in the junction are swept out by the reverse bias, thus charging the capacitor C. The charge on the capacitor then decays through the resistor. Provided that the energy is deposited on the photodiode in a time short compared to the RC time constant of the circuit, the peak charge on the capacitor is proportional to the total energy deposited on the detector. The exponential voltage decay from this circuit is usually displayed on an oscilloscope and recorded on photographic film. The limited accuracy with which these visual readings may be made and the cost of the photographic film, if many measurements are to be made, are two shortcomings of this measurement method.

A simple, inexpensive circuit that avoids the above difficulties is shown in Fig. A2. Built with moderately priced, readily available operational amplifiers, the circuit provides for a digital display that is proportional to the energy incident on the photodiode and that has an electronic accuracy of 1%. The circuit consists of three basic units: an integrating detector circuit, an amplifying circuit, and a unique peak-detector-and-hold circuit.

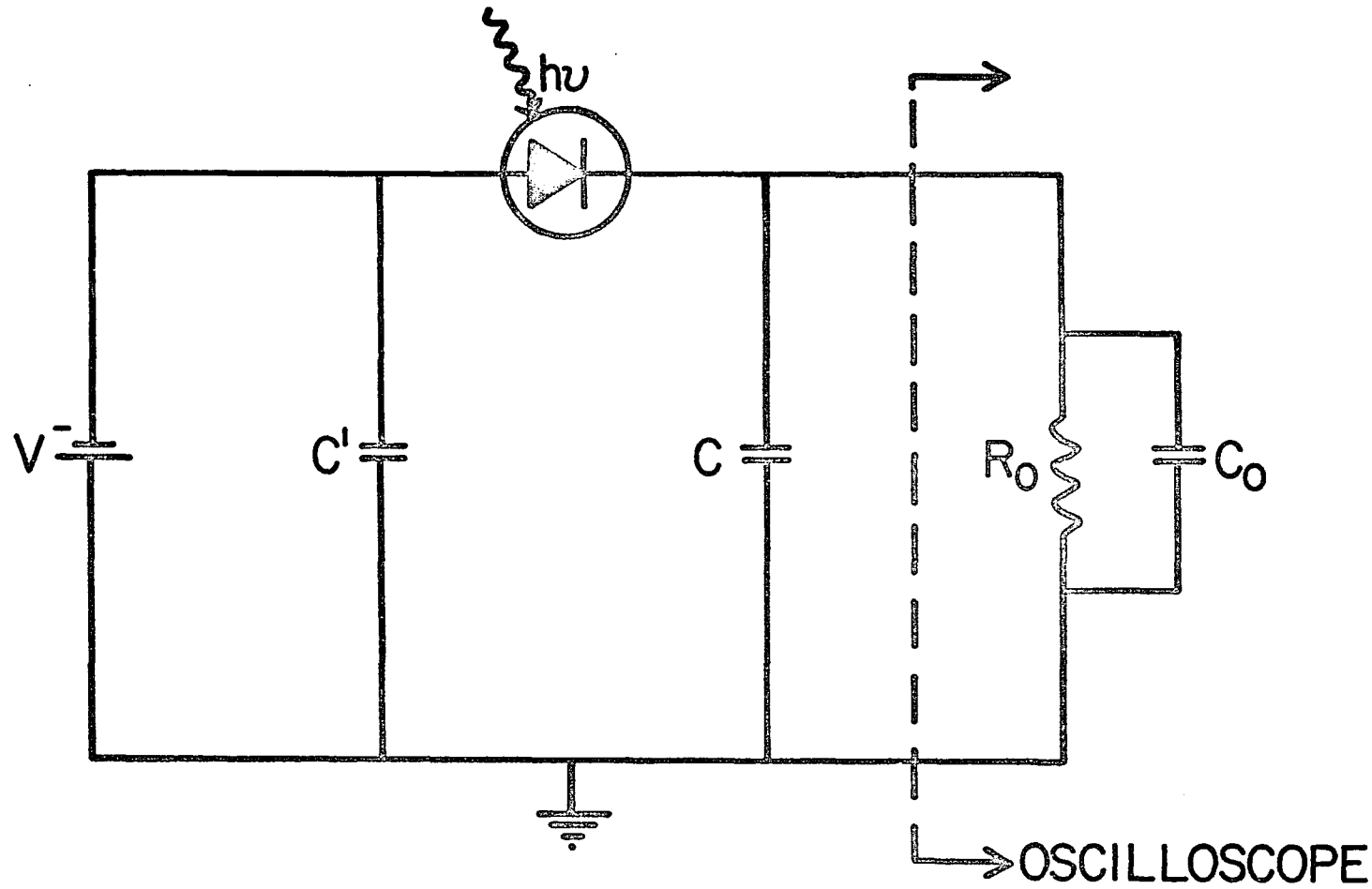

Fig. A1. Typical Photodiode Integrating Circuit.

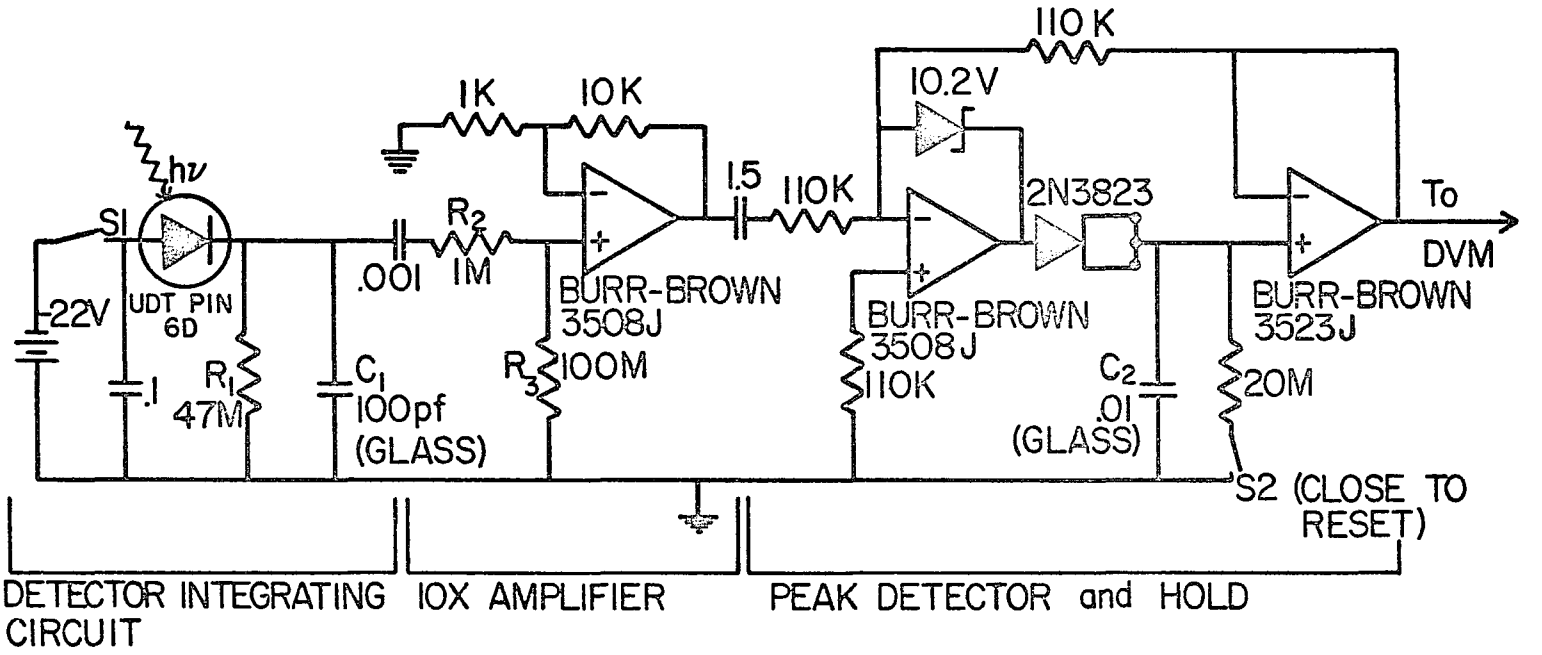

Fig. A2. Energy Monitor for Short Pulse Lasers.

Resistance is in ohms and capacitance
is in μF, unless otherwise noted.

The detector used is a United Detector Technology PIN 6D silicon photodiode operated in the photoconductive mode. The diode is reverse biased by a 22 V battery through the 47 MΩ resistor. The operation of the integrating circuit is identical to that of the circuit described above. Since the peak voltage across the integrating capacitor C_1 is proportional to the pulse energy incident on the diode, a large RC time constant is desirable to prolong the decay of this signal. However, a tradeoff is required by two constraints on R_1 and C_1. (1) A significant portion of the reverse bias voltage must appear across the photodiode; thus, the value of R_1 must be comparable to or less than the reverse bias resistance of the diode (in this case ∿100 MΩ). (2) In order that the signal provided by the detector circuit not be lost in the internal noise of the amplifiers that follow, the capacitor must provide a signal voltage $V = Q/C_1$ that exceeds the noise voltage (∿1 mV in our circuit). Our particular application involves monitoring low energy pulses of a few picoseconds duration, and the circuit parameters were chosen with this application in mind. These parameters may be adjusted to accommodate other signal and noise levels.

The detector is AC coupled to a noninverting amplifier (with a gain of 10 in our case). As discussed in a later paragraph, this amplifier must ensure a signal between ∿0.6 and 10 V as in input to the peak detector and hold circuit. The slew rate of this amplifier must be such that it can capture the input waveform before it decays by more than 1%. For times short compared to the response time of this amplifier, the amplifier will not exhibit its "ideal" input impedance, and for this

reason a 1 MΩ decoupling resistor (R_2) is incorporated into the circuit to insure a minimum acceptable charge error on the integrating capacitor. The resistor R_3 (100 MΩ) provides the return path for the AC coupling capacitor, and together with R_2 it forms a voltage divider with a reduction factor of 1 to 2%, provided the input impedance of the operational amplifier is 100 MΩ or greater. Because of operational amplifier input bias currents a voltage will be developed across resistor R_3. This may be compensated for by adjusting the internal voltage offset of the operational amplifier.

The first operational amplifier in the peak detector and hold unit is effectively an inverting, unit gain amplifier that charges the 0.01 μF track and hold capacitor C_2. The second amplifier is a high input impedance, low bias current, unity gain buffer amplifier that allows the voltage across capacitor C_2 to be read while drawing negligible charge from it. A 2N3823 FET is used as a high reverse impedance diode to clamp the capacitor voltage at the peak of the input waveform. When the input signal (a negative, decaying step function) to the first inverting amplifier appears, its output becomes positive. Since there is no initial charge on the capacitor, the diode is forward biased and allows the capacitor to be charged. The second amplifier feeds this voltage back to the input of the first amplifier while drawing negligible charge from the capacitor. Due to the finite slew rate of the second operational amplifier, there is, however, some lag between the time the track and hold capacitor voltage reaches some value and the time that value is fed back to the input of the first amplifier.

During this time, the first amplifier has no feedback and is showing open loop again. Due to current limiting in the first operational amplifier, the capacitor charges in a linear fashion during this period. Once the first operational amplifier begins to receive feedback from the second, the capacitor charges in an exponential fashion. (The significance of these two types of charging will be discussed further.) So long as the input signal continues to decrease, the capacitor will continue to be charged; however, as soon as the input signal starts to increase (decrease in absolute value), the diode (FET) will become reverse biased, thus decoupling the capacitor C_2. The capacitor must thus hold the negative peak of the incoming waveform. This voltage may decay only through the extremely high reverse resistance of the FET or due to the bias current from the noninverting buffer amplifier.

In general, the frequency response of an operational amplifier suffers drastically when it is driven into saturation. For this reason a Zener diode is incorporated into the feedback loop of the first operational amplifier. The forward voltage drop of the Zener diode limits the amplifier output to negative 0.7 V when no signal is present on the input. Likewise, the Zener diode limits the positive output of the amplifier to a value equal to the reverse breakdown voltage (10.2) of the diode whenever an input signal is applied.

The offset voltage of the first operational amplifer (peak detector and hold section) is important and may be conveniently checked by shunting the FET by a resistor (e.g., 1 kΩ) and monitoring the output of the buffer amplifier. The offset voltage of the buffer amplifier is

relatively unimportant since it is compensated for in the feedback loop of the first amplifier.

This peak detector and hold circuit is unique because of the use of an inexpensive ultralow input offset current operational amplifier (Burr-Brown 3523J) having limited bandwidth as the buffer amplifier (Graeme, 1974). The limited bandwidth, i.e., slower response, causes the brief period of linear charging due to no feedback (previously described) during which time the tracking capacitor is not following the input signal. Thus for small signals applied to the peak detector and hold, the voltage on the tracking capacitor will actually overshoot the peak of the input. For our circuit the dynamic range of the input is thus restricted to 0.6 to 10 V, rather than 0 to 10 V as in the ideal case. For exponential charging (due to feedback) there is no overshoot.

The sacrifice of dynamic range in the design allows construction of a much less expensive peak detector and hold than is commercially available. All the components for the energy monitor cost a total of $150, including the photodiode and operational amplifier power supplies (but not the digital voltmeter). The choice of an inexpensive buffer amplifier involves a tradeoff between low input offset current (long hold time) and large bandwidth (large dynamic range); we chose the former. Commercial peak detector and hold circuits use a more expensive buffer amplifier that has both low input offset current and large bandwidth.

A simple method of dynamically testing the peak detector is to apply a repetitive pulse train as an input while the track and hold

capacitor C_2 is shunted by a resistor providing an RC time constant less than the repetition rate. The waveforms on the capacitor and amplifier output may be observed and will exhibit the effects of finite slew rate and amplifier overshoot.

The signal from our peak detector decays less than 2% in the first 30 sec. The overall settling time of the peak detector unit is $\sim$50 μsec. Care should be exercised in choosing a capacitor for this unit, since many capacitors were found to have a leakage resistance that was much less than the back resistance of the FET or the input impedance of the buffer operational amplifier. A glass capacitor proved adequate for our purposes.

This energy monitor can be calibrated either absolutely against a calibrated thermopile or relatively if several similar units are to be used to determine parameters such as reflection and transmission coefficients. Electrical and optical noise problems are minimized by mounting the detector and associated circuits in a copper box and by baffling the detector optics, respectively.

This instrument provides an inexpensive, electronically accurate means of monitoring the energy of an optical pulse. When the output is displayed on a digital voltmeter, this unit provides a digital signal that is electronically accurate to $\sim$1% when read or recorded within 15 sec after the pulse is incident on the photodiode.

APPENDIX B

NONLINEAR, NONEQUILIBRIUM OPTICAL PROPERTIES OF MERCURY CADMIUM TELLURIDE

In this appendix, we describe the application of the experimental techniques of Chapter 3 to the measurement of the nonlinear, nonequilibrium properties of mercury cadmium telluride. Specifically, the single pulse transmission has been measured as a function of incident pulse energy for sample temperatures of 77 K and 300 K. In addition, the relative transmission of a probe pulse as a function of time delay after an excitation pulse has been measured for several different temperatures, surface preparations, and excitation pulse energies. Mercury cadmium telluride was selected for these studies because (1) it is a direct band gap material and (2) its band gap may be changed by varying the mole fraction x of Cd present in the compound (Schmit and Stelzer, 1969). One anticipates that these properties will contribute to the understanding of these novel solid state phenomena.

The optical pulses used in these experiments were obtained from a mode-locked Nd:glass laser. The wavelength of this radiation is 1.06 μm and the pulse width is on the order of 5 to 10 psec. These optical pulses were focused on the sample to a spot with a diameter of approximately 480 μm. The samples were single crystals of $Hg_{1-x}Cd_xTe$ with $x \sim 0.2$, 0.4, and 0.6 (see Table B1). For each x value three samples were prepared, each with a different surface treatment. The first

Table B1. Some Properties of Nine $Hg_{1-x}Cd_xTe$ Samples in This Experiment: Mole Fraction x of Cd, Band Gap in Electron Volts at 297 K and 105 K, Preparation of First and Second Surfaces, Type and Concentration (cm^{-3}) of Impurities.

SAMPLE NUMBER	X	E_G (300)	E_G (77)	FRONT SURFACE	BACK SURFACE	TYPE	CONCENTRATION
1	0.204	0.167	0.100	POLISHED	POLISHED	P	$<10^{16}$
2	0.4	0.433	0.414	POLISHED	POLISHED	P	$>6\times10^{16}$
3	0.61	0.752	0.783	POLISHED	POLISHED	P	?
4	0.204	0.167	0.100	ETCHED	POLISHED	P	$<10^{16}$
5	0.4	0.433	0.414	ETCHED	POLISHED	P	$>6\times10^{16}$
6	0.61	0.752	0.783	ETCHED	POLISHED	P	?
7	0.203	0.175	0.109	ETCHED	ETCHED	n	7×10^{15}
8	0.404	0.439	0.420	ETCHED	ETCHED	P	?
9	0.623	0.772	0.807	ETCHED	ETCHED	P	?

sample of each x value was mounted on a KZF-2 substrate and polished to a thickness of 5 μm or less; the second was mounted, polished, then etched on one surface; the third was polished, then etched on both surfaces. The exact x values and energy gaps for these samples at 77 K and 300 K are shown in Table B1.

When irradiated by a single pulse, the transmission of each sample as a function of pulse energy was recorded. Regardless of surface preparation, the transmission of samples with x value of 0.2 showed no deviation from linear, Beer's law behavior even when irradiated with pulses of sufficient energy to cause damage to the sample surface. The same was true for samples with x value of 0.4. The samples with x value of 0.6 and polished on both sides, but not etched, also exhibited no nonlinear behavior; however, the transmission of the two etched samples with x value of 0.6 (samples 6 and 9) did deviate markedly from Beer's law. The nonlinear transmission of sample 6 as a function of incident pulse energy is plotted for sample temperature of 297 K and 105 K in Figs. B1 and B2. The increase in transmission was a factor of about 10 at 297 K and 30 at 105 K. In contrast to our experience with Ge, these measurements indicate that the saturation of the transmission in these samples depends on the surface preparation. The nonlinear behavior of sample 9 was similar to that shown for sample 6.

The decay of the saturated optical absorption was investigated by irradiating a sample of $Hg_{1-x}Cd_xTe$ with a single intense optical pulse and monitoring the transmission of a weaker probe pulse, split from the intense pulse, that arrives a time t_d later. The data for sample 6

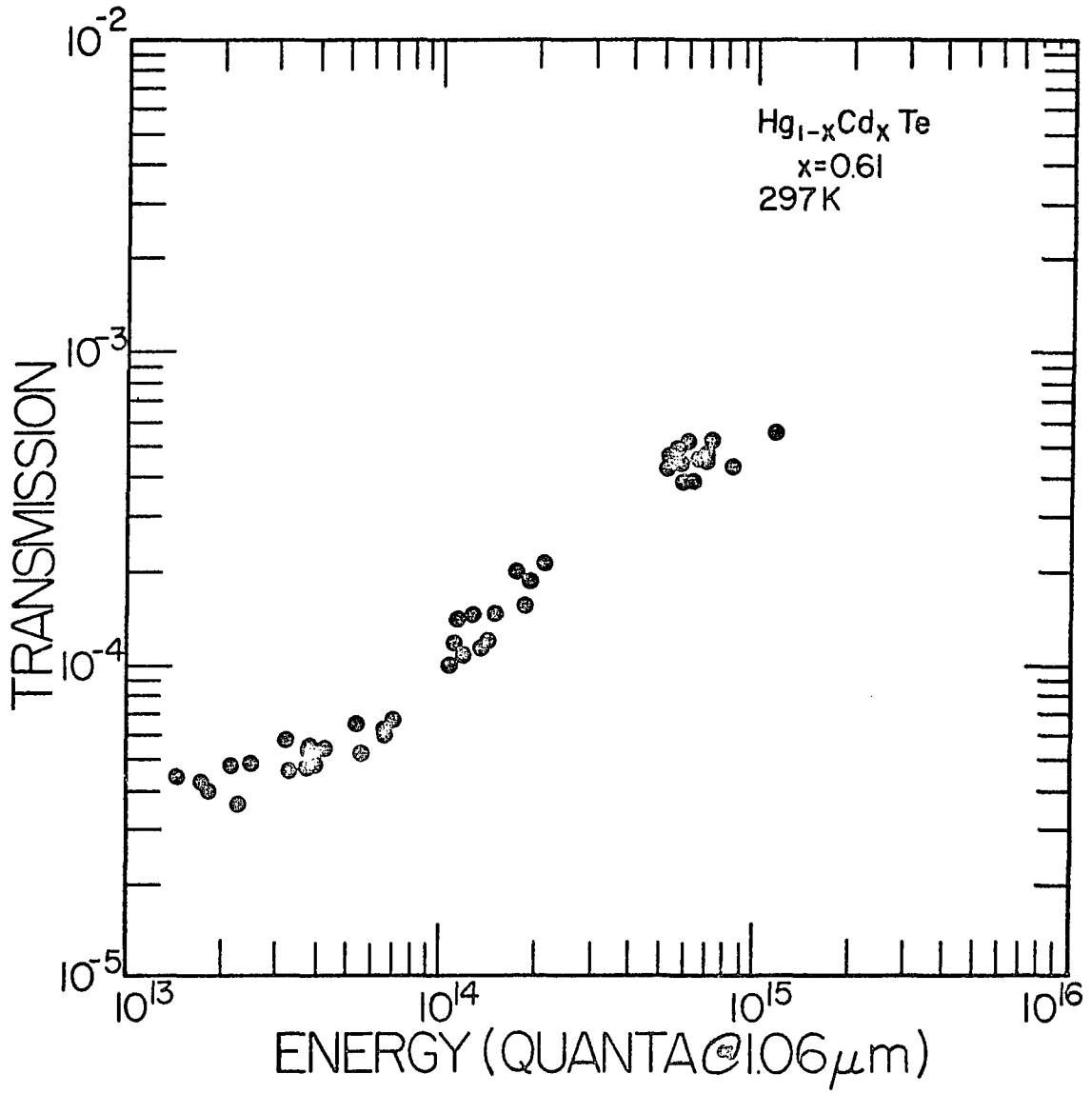

Fig. B1. Single Pulse Transmission of Sample 6 at 297 K.

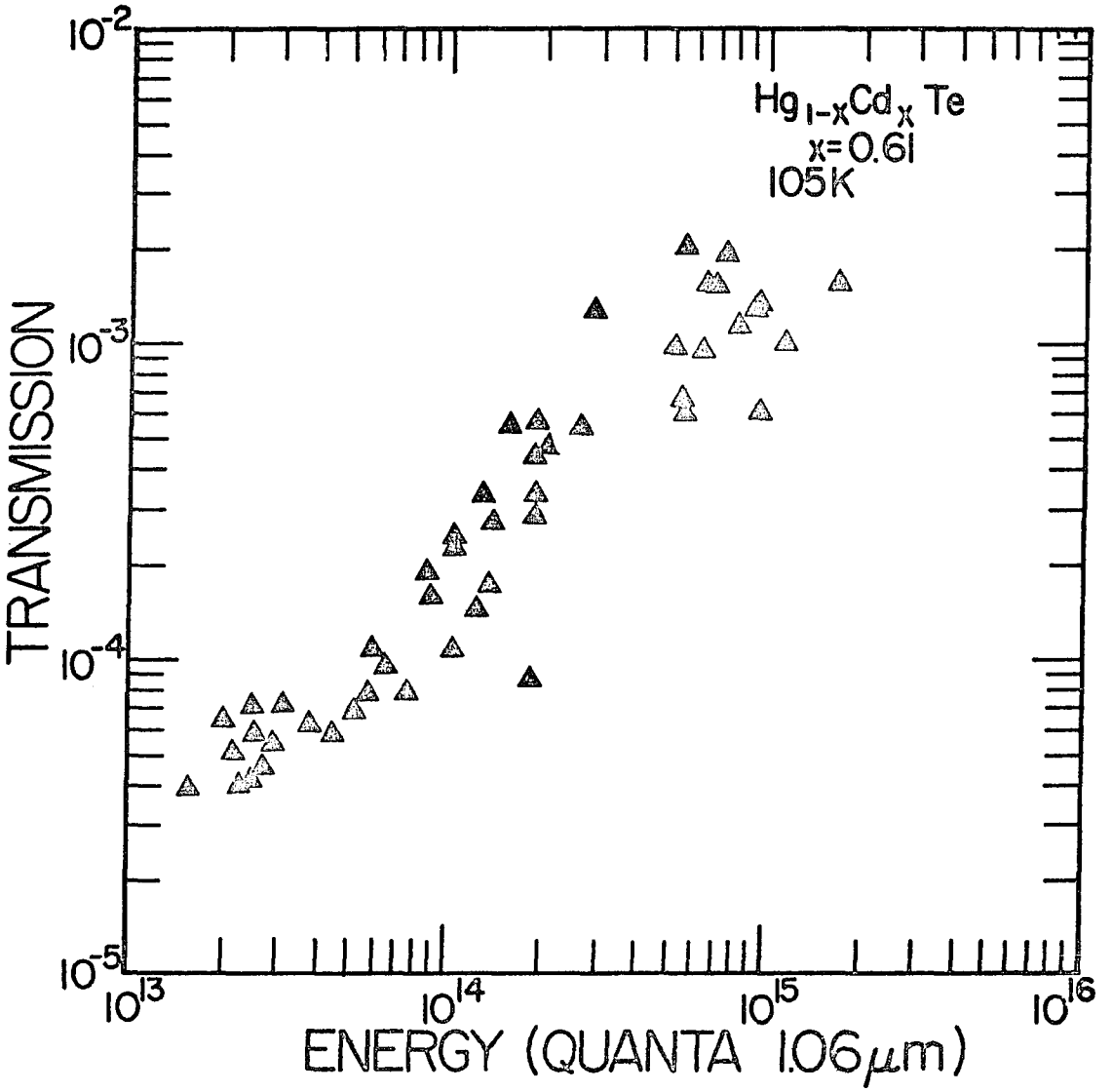

Fig. B2. Single Pulse Transmission of Sample 6 at 105 K.

are presented in Fig. B3 as a plot of the normalized ratio of probe pulse to excitation pulse transmission versus the delay of the probe pulse relative to excitation pulse for the two temperatures 297 K and 105 K. In these experiments the probe pulse had 5% of the energy of the excitation pulse. The excitation pulse was in the region of nonlinear transmission and the probe pulse in the region of linear transmission. Each point shown is the average of five data points, and the error bars indicate one standard deviation.

For comparison, the data for $Hg_{1-x}Cd_xTe$ sample 6 and a sample temperature of 297 K are plotted in Fig. B4, together with a similar curve for Ge (Smirl et al., 1975). The rapid rise and fall of the probe transmission occurring near zero delay in germanium has been attributed (Smirl et al., 1975; Shank and Auston, 1975; Shih et al., 1973) to a coupling of the two optical beams due to an index grating produced in the electron-hole plasma. Note that the narrow peak in transmission observed for $Hg_{1-x}Cd_xTe$ is not entirely due to the same phenomenon. Careful investigation of Fig. B3 shows that the rapid rise and fall of the probe transmission are not symmetric about zero delay as would be required if they were due to a correlation of the two pulses. In addition, the width of the peak is too large for the presence of the correlation spike alone. The rise time of the relative probe transmission, which is fitted well by an exponential, is about 10 psec for both 105 K and 297 K. The decay time of the 297 K curve is about 30 psec, while the decay for 105 K is somewhat shorter but does not have a good fit to a single exponential. The asymmetric form of the relative probe transmission

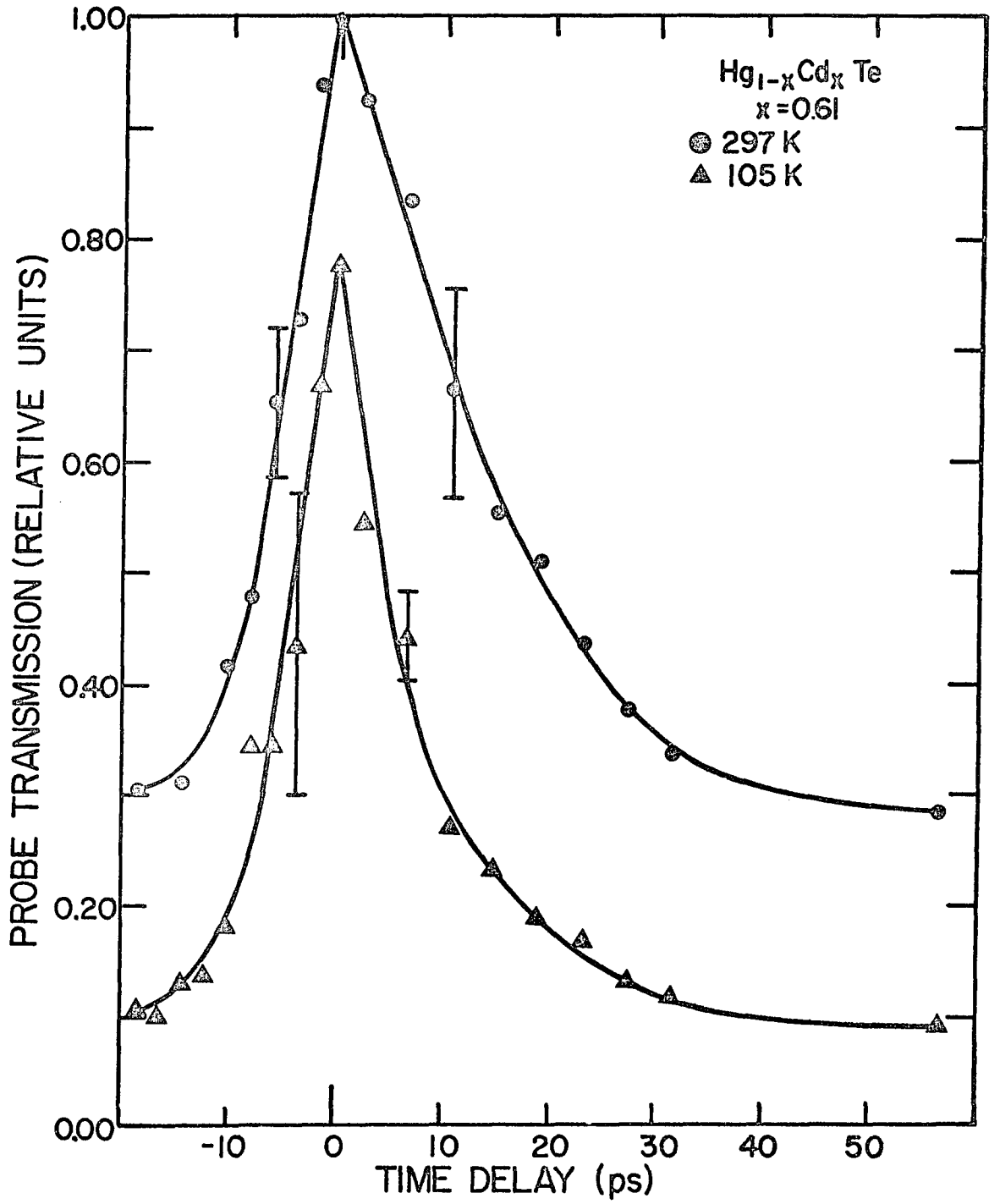

Fig. B3. Normalized Probe Pulse Transmission Versus Time Delay of Probe Pulse for Sample 6 at 297 K and 105 K.

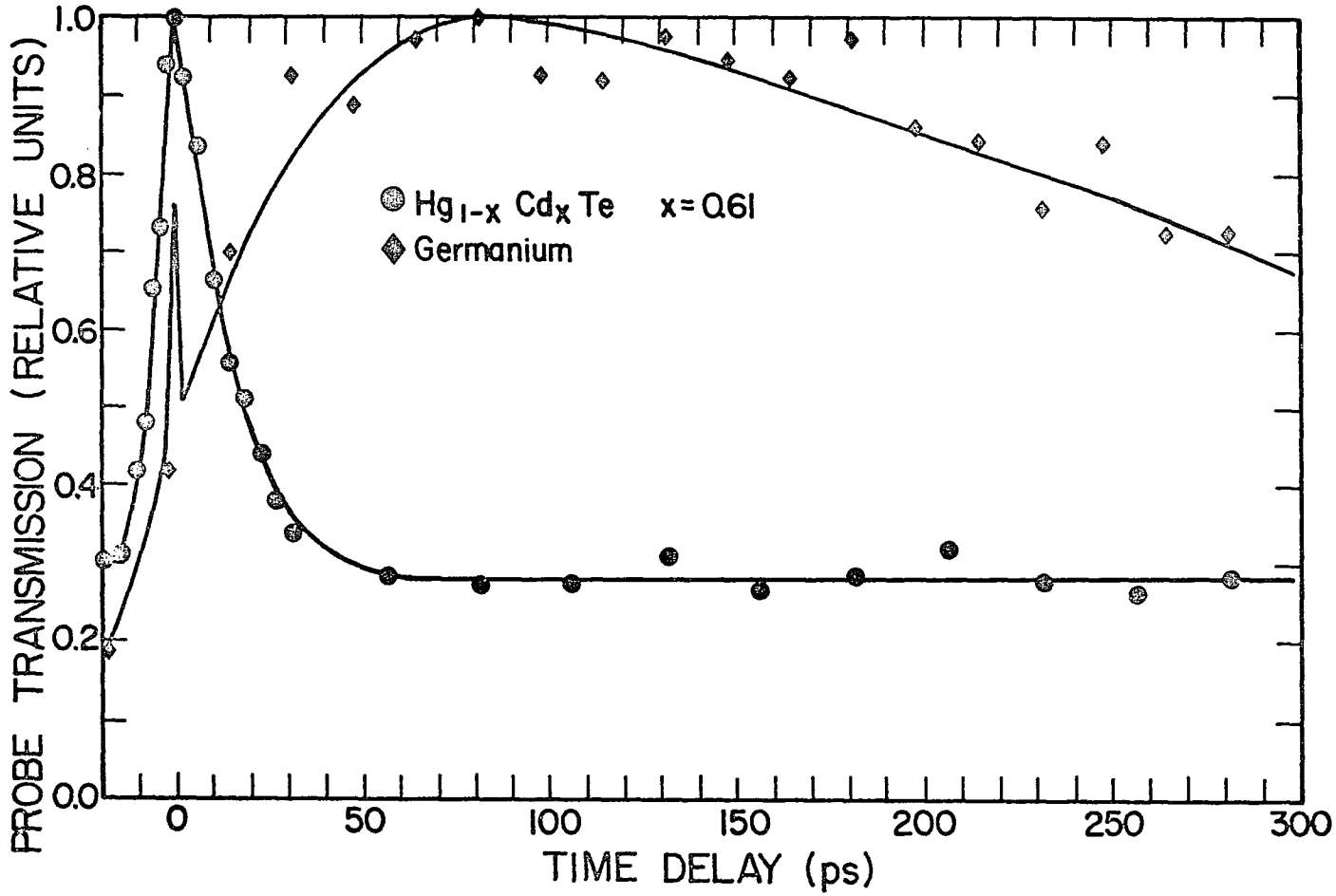

Fig. B4. Normalized Probe Pulse Transmission Versus Time Delay of Probe Pulse Comparing Sample 6 with Germanium.

versus delay was invariant for samples 6 and 9 and for repeated data runs.

Figure B5 is a plot (for sample 6) of normalized probe transmission versus time delay for two different excitation energies, both with the sample at 300 K. The ratios of 100:5 and 67:3 are the relative ratios of the excitation-to-probe energies. Again, each plotted point is the average of five data points, and the error bars indicate one standard deviation.

The observation that the saturation of the optical transmission depends on surface preparation makes interpretation of these data difficult. It is clear that etching of the surface allows a saturation of the transmission, but it is not obvious that etching removes the surface defects from consideration entirely. However, the data reported here do not absolutely determine whether the rise and fall times of the probe transmission are due to surface states or bulk material properties. The anomalous effects of surface layers on the electrical properties of $Hg_{1-x}Cd_xTe$ have been discussed by Scott and Hager (1971).

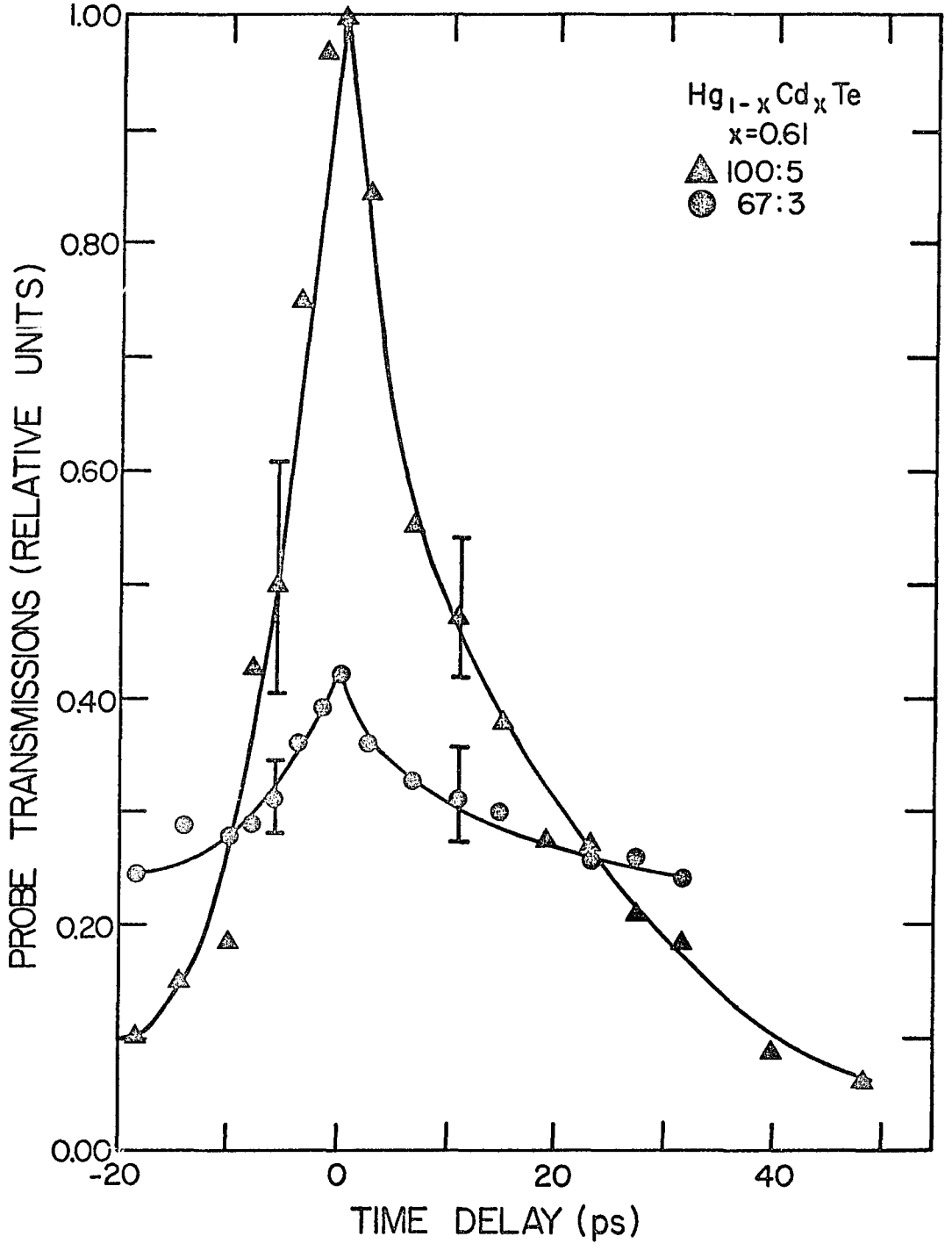

Fig. B5. Normalized Probe Pulse Transmission Versus Time Delay of Probe Pulse for Sample 6 as a Function of Two Different Excitation Energies.

Ratios are relative energies of excitation pulse to probe pulse.

APPENDIX C

PHONON-ASSISTED INTRAVALLEY RELAXATION

In this appendix, we consider the intraband relaxation of electrons and holes by means of phonon emission and absorption. In particular, starting from elementary perturbation theory, we will calculate the right-hand side of Eq. (69).

Perturbation Theory

We first find a general expression for the transition rate of a system from a state $|m\rangle$ to the state $|n\rangle$ under the influence of the perturbation V. The states $|m\rangle$ and $|n\rangle$ and their energies E_m and E_n are the eigenfunctions and eigenvalues of the unperturbed Hamiltonian operator H_0. The operator H_0 is the sum of the unperturbed Hamiltonian operators of the two subsystems, H_1 and H_2. We may then write

$$H_0|\ell\rangle = E_\ell|\ell\rangle \tag{C-1}$$

and

$$H = H_0 + V \tag{C-2}$$

where H is the total Hamiltonian operator. The state vector for the system may be written

$$|\psi\rangle = \sum_\ell a_\ell(t)\, \exp[-iE_\ell t/\hbar]|\ell\rangle. \tag{C-3}$$

We require that this state vector obey Schrödinger's equation:

$$i\hbar \frac{d|\psi>}{dt} = [H_0 + V]|\psi>. \tag{C-4}$$

Using Eq. (C-3) in (C-4) and projecting both sides of the resulting equation onto the bra vector $<j|$, we obtain the following expression for the probability amplitudes:

$$\frac{da_j(t)}{dt} = -\frac{i}{\hbar} \sum_{\ell} a_\ell(t)<j|V|\ell> \exp[i(\omega_j - \omega_\ell)t], \tag{C-5}$$

where $E_j/\hbar$ has been denoted by ω_j.

Suppose that prior to interacting, the two subsystems are in a state $|m>$. This implies that the only nonzero probability amplitude at the instant the systems are allowed to interact is a_m, that is

$$a_\ell(o) = \delta_{\ell m}. \tag{C-6}$$

Using this information in Eq. (C-5) and integrating with respect to time, we obtain the following first-order probability amplitude that the system will make a transition from an initial state $|m>$ to a final state $|n>$ after some time t

$$a_{nm}^{(1)}(t) = -\frac{i}{\hbar} <n|V|m> \int_0^t \exp[i(\omega_n - \omega_m)t']dt'. \tag{C-7}$$

Substituting Eq. (C-7) into Eq. (C-5) and integrating, we obtain an expression for the second-order contribution to a_{nm}

$$a_{nm}^{(2)}(t) = \frac{1}{\hbar^2} \sum_{f} <n|V|f> <f|V|m> \int_0^t dt'' \exp[i(\omega_n - \omega_f)t''] \cdot \int_0^{t''} dt' \exp[i(\omega_f - \omega_m)t']. \tag{C-8}$$

In Eqs. (C-7) and (C-8), we have removed terms of the form $\langle i|V|j\rangle$ from the time integration by recalling that in the Schrödinger representation the operator V does not depend on time.

If the initial time is taken as $-\infty$ and the final time as $t = \infty$, the matrix elements $\alpha_{nm}(\infty)$ are denoted by $\langle n|S|m\rangle$ and are called elements of the S-matrix. In this case, our first-order and second-order terms, Eqs. (C-7) and (C-8), may be explicitly evaluated to give

$$\langle n|S^{(1)}|m\rangle = -2\pi i\delta(E_n - E_m)\langle n|V|m\rangle \tag{C-9}$$

and

$$\langle n|S^{(2)}|m\rangle = -2\pi i\delta(E_n - E_m)\sum_f \frac{\langle n|V|f\rangle\langle f|V|m\rangle}{E_m - E_f}. \tag{C-10}$$

The S-matrix is given to second order by

$$\langle n|S|m\rangle = -2\pi i\delta(E_n - E_m)\langle n|T|m\rangle \tag{C-11}$$

where

$$\langle n|T|m\rangle = \langle n|V|m\rangle + \sum_f \frac{\langle n|V|f\rangle\langle f|V|m\rangle}{E_m - E_f}. \tag{C-12}$$

From Eq. (C-11) it follows that the probability of a transition during an infinite period of time is given by

$$W_{nm}(\infty) = |\langle n|S|m\rangle|^2 = 4\pi^2\delta^2(E_m - E_n)|\langle n|T|m\rangle|^2. \tag{C-13}$$

The square of the delta function may be transformed into

$$\delta^2(E_n - E_m) = \frac{\delta(E_n - E_m)}{2\pi\hbar}\lim_{T\to\infty}\int_{-T}^{T}\exp[i(E_n - E_m)t/\hbar]dt$$

$$= \frac{\delta(E_n - E_m)}{2\pi\hbar}\lim_{T\to\infty}\int_{-T}^{T}dt. \tag{C-14}$$

Thus, the transition rate may be written

$$P_{nm} = \frac{W_{nm}(\infty)}{\lim_{T\to\infty} \int_{-T}^{T} dt} = \frac{2\pi}{\hbar} \delta(E_n - E_m) |\langle n|T|m\rangle|^2. \qquad \text{(C-15)}$$

Using the probability of a transition per unit time given by Eq. (C-15) together with the T-matrix to second order given by Eq. (C-12), one may calculate any of the transition rates appearing in the equations of Chapter 4. The development of perturbation theory presented above is standard and may be found in many texts on quantum mechanics, for example Davydov (1966).

In this appendix, we use perturbation theory together with the electron-phonon interaction Hamiltonian to calculate the right-hand side of Eq. (69).

Intravalley First-Order Electron-Phonon Relaxation

The electron-phonon interaction Hamiltonian is given by Kittel (1963) as

$$H' = i \sum_{\vec{q},\mu} \left(\frac{\hbar}{2\rho\Omega_{q\mu}}\right)^{1/2} Q_\mu \sum_{n\vec{k}} \sum_{n'\vec{k}'} c^+_{n'k'} c_{nk}$$

$$\cdot \left[a_{q\mu} \langle n'k'| \exp(i\vec{q}\cdot\vec{r}) |nk\rangle \right.$$

$$\left. - a^+_{q\mu} \langle n'k'| \exp(-i\vec{q}\cdot\vec{r}) |nk\rangle\right], \qquad \text{(C-16)}$$

where Q_μ represents the phonon coupling constant (either optical or acoustic), ρ the density of the germanium sample, $\hbar$ Planck's constant

divided by 2π, $\vec{q}$ the phonon wave vector, μ the polarization of the phonon (longitudinal or transverse), and $\Omega_{q\mu}$ the circular frequency of a phonon of wavevector q with polarization μ. The symbols c^+ and c denote the electron creation and annihilation operators; a^+ and a denote the phonon creation and annihilation operators. In addition, $|nk\rangle$ represents the electron Bloch state $\exp[i\vec{k} \cdot \vec{r}]U_{n\vec{k}}(\vec{r})$.

The four ways in which an electron may be scattered by a phonon into or out of a state in the ℓth energy band with wavevector $\vec{p}$ are illustrated in the scattering diagrams of Fig. C1. We initially consider only optical phonons. This requires that $\Omega_{q\mu}$ be replaced by the single optical phonon frequency Ω_0, independent of polarization or wavevector. The interaction Hamiltonian of Eq. (C-16) when substituted into Eq. (C-15) yields the following transition rates for the diagrams of Fig. C1

$$\left(\frac{\partial f_\ell(\vec{p})}{\partial t}\right)_{(a)} = \sum_{\vec{q},\mu} \sum_{\ell'} \left(\frac{2\pi}{\hbar}\right) \left(\frac{\hbar}{2\rho\Omega_0}\right) D_0^2 [1 - f_\ell(\vec{p})] f_{\ell'}(\vec{p} - \vec{q}) N_{q\mu}$$
$$\cdot |\langle \ell, \vec{p}| \exp(i\vec{q} \cdot \vec{r}) |\ell', \vec{p} - \vec{q}\rangle|^2$$
$$\cdot \delta[E_\ell(\vec{p}) - E_{\ell'}(\vec{p} - \vec{q}) - \hbar\Omega_0], \qquad \text{(C-17)}$$

$$\left(\frac{\partial f_\ell(\vec{p})}{\partial t}\right)_{(b)} = -\sum_{\vec{q},\mu} \sum_{\ell'} \left(\frac{2\pi}{\hbar}\right) \left(\frac{\hbar}{2\rho\Omega_0}\right) D_0^2 [1 - f_{\ell'}(\vec{p} - \vec{q})] f_\ell(\vec{p})$$
$$\cdot (N_{q\mu} + 1) \cdot |\langle \ell', \vec{p} - \vec{q}| \exp(-i\vec{q} \cdot \vec{r}) |\ell, \vec{p}\rangle|^2$$
$$\cdot \delta[E_\ell(\vec{p}) - E_{\ell'}(\vec{p} - \vec{q}) - \hbar\Omega_0] \qquad \text{(C-18)}$$

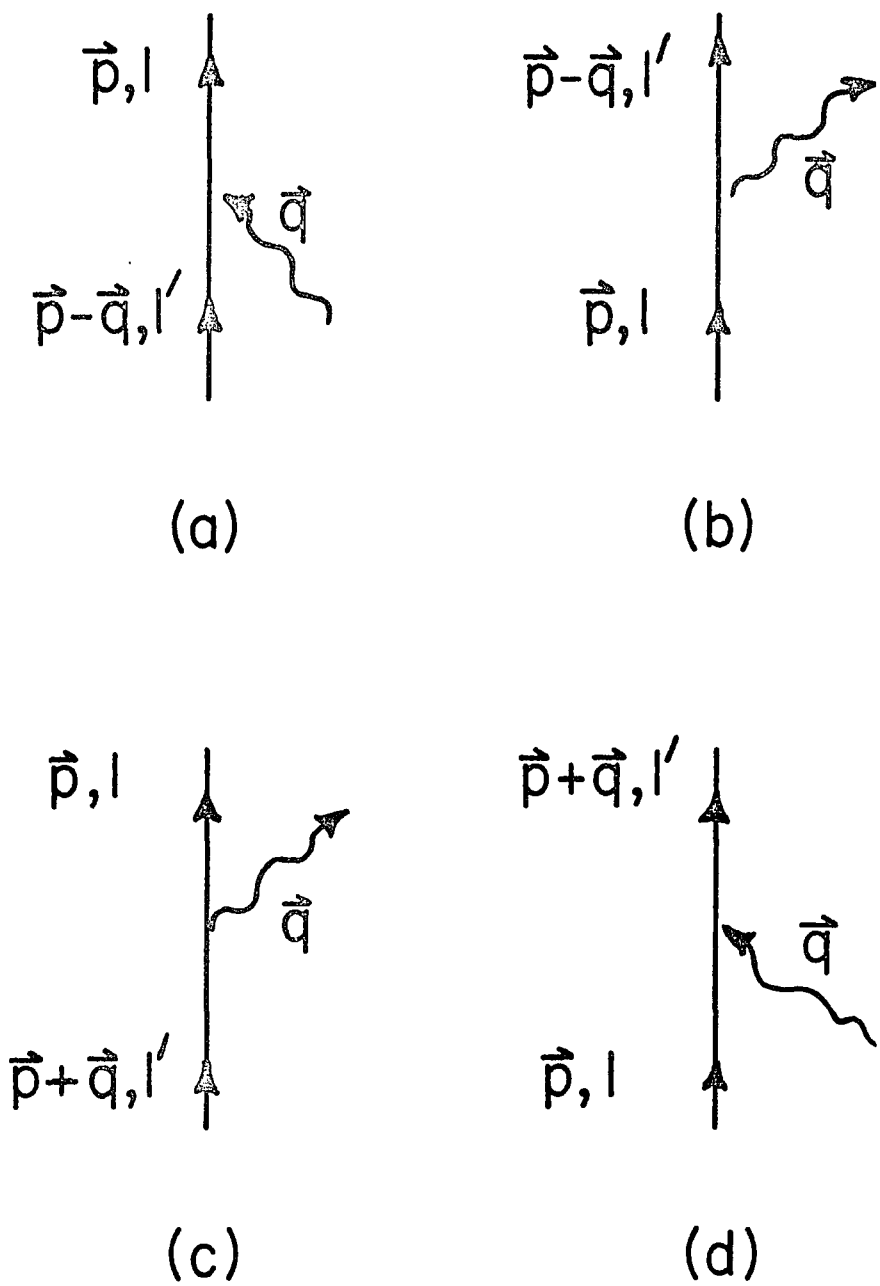

Fig. C1. Electron-Phonon Scattering Diagrams.

$$\left(\frac{\partial f_{\ell}(\vec{p})}{\partial t}\right)_{(c)} = \sum_{\vec{q},\mu}\sum_{\ell'}\left(\frac{2\pi}{\hbar}\right)\left(\frac{\hbar}{2\rho\Omega_0}\right) D_0{}^2[1 - f_{\ell}(\vec{p})]f_{\ell'}(\vec{p} - \vec{q})(N_{q\mu} + 1)$$

$$\cdot \left|\langle \ell, \vec{p}\right| \exp(-i\vec{q} \cdot \vec{r}) \left|\ell', \vec{p} + \vec{q}\rangle\right|^2$$

$$\cdot \delta[E_{\ell}(\vec{p}) - E_{\ell'}(\vec{p} + \vec{q}) + \hbar\Omega_0], \qquad \text{(C-19)}$$

$$\left(\frac{\partial f_{\ell}(\vec{p})}{\partial t}\right)_{(d)} = -\sum_{\vec{q},\mu}\sum_{\ell'}\left(\frac{2\pi}{\hbar}\right)\left(\frac{\hbar}{2\rho\Omega_0}\right) D_0{}^2[1 - f_{\ell'}(\vec{p} + \vec{q})]f_{\ell}(\vec{p})N_{q\mu}$$

$$\cdot \left|\langle \ell', \vec{p} + \vec{q}\right| \exp(i\vec{q} \cdot \vec{r}) \left|\ell, \vec{p}\rangle\right|^2$$

$$\cdot \delta[E_{\ell}(\vec{p}) - E_{\ell'}(\vec{p} + \vec{q}) + \hbar\Omega_0], \qquad \text{(C-20)}$$

where $N_{q\mu}$ denotes the number of phonons of wavevector $\vec{q}$ and polarization μ, and D_0 is the optical phonon-electron coupling constant. In addition, $E_i(\vec{p})$ represents the energy of the state in the ith band with wavevector $\vec{p}$; $f_i(\vec{p})$ denotes the probability of that state being occupied.

Adding the four equations written above, regrouping terms, and considering only <u>intraband</u> optical phonon-assisted transitions in the conduction band [$\langle \ell', \vec{p} + \vec{q}| \exp(i\vec{q} \cdot \vec{r}) |\ell, p\rangle \simeq \delta_{\ell\ell'}$], we find that the total electron transition rate for all four diagrams of Fig. C1 becomes

$$\left(\frac{\partial f_{cj}(p)}{\partial t}\right)^{op.}_{REL} = \frac{\pi D_0{}^2}{\rho\Omega_0}\sum_{\vec{q},\mu}\{N_{q\mu}\{[f_{cj}(\vec{p} + \vec{q}) - f_{cj}(\vec{p})]$$

$$\cdot \delta[E_{cj}(\vec{p} + \vec{q}) - E_{cj}(\vec{p}) - \hbar\Omega_0]$$

$$- [f_{cj}(\vec{p}) - f_{cj}(\vec{p} - \vec{q})]\delta[E_{cj}(\vec{p}) - E_{cj}(\vec{p} - \vec{q}) - \hbar\Omega_0]\}$$

$$+ \{f_{cj}(\vec{p} + \vec{q})[1 - f_{cj}(\vec{p})]$$

$$\cdot \delta[E_{cj}(\vec{p} + \vec{q}) - E_{cj}(\vec{p}) - \hbar\Omega_0]$$

$$- f_{cj}(\vec{p})[1 - f_{cj}(\vec{p} - \vec{q})]$$

$$\cdot \delta[E_{cj}(\vec{p}) - E_{cj}(\vec{p} - \vec{q}) - \hbar\Omega_0]\}), \qquad \text{(C-21)}$$

where cj represents the jth valley of the conduction band.

If we take the phonon distribution to be at equilibrium with the lattice temperature, the phonon distribution may be approximated by

$$N_{q\mu} = \frac{1}{\exp\left(\frac{\hbar\Omega_{q\mu}}{k_B T_0}\right) - 1} \simeq \frac{k_B T_0}{\hbar\Omega_{q\mu}} = \left(\frac{\hbar\omega_0}{\hbar\Omega_{q\mu}}\right) T_0, \qquad \text{(C-22)}$$

for lattice temperatures such that $\hbar\Omega_{q\mu} << k_B T_0$.

If the number of phonons is given by Eq. (C-22), then the stimulated and spontaneous parts of Eq. (C-21) may be put into similar forms by observing that

$$f_{cj}(\vec{p} + \vec{q})[1 - f_{cj}(\vec{p})] = f_{cj}(E_{cj}(\vec{p}) + \hbar\Omega_0)[1 - f_{cj}(E_{cj}(\vec{p})]$$

$$= \frac{1}{\exp\left(\frac{\hbar\Omega_0}{k_B T_L}\right) - 1} \{f_{cj}[E_{cj}(\vec{p})]$$

$$- f_{cj}[E_{cj}(\vec{p}) + \hbar\Omega_0]\}$$

$$\simeq \left(\frac{\hbar\omega_0}{\hbar\Omega_0}\right) T_0 \{f_{cj}[E_{cj}(p)] - f_{cj}[E_{cj}(p)$$

$$+ \hbar\Omega_0]\}. \qquad \text{(C-23)}$$

Also, by noticing that $\hbar\Omega_0$ is small compared to electron energies,

$$E_{cj}(\vec{p}) = \frac{\hbar^2 p^2}{2m_c} + E_G \equiv E + E_G >> \hbar\Omega_0, \tag{C-24}$$

we can make the following approximation

$$\{f_{cj}[E_{cj}(p)] - f_{cj}[E_{cj}(p) + \hbar\Omega_0]\} \simeq -\hbar\Omega_0 \frac{\partial f_c(E + E_G)}{\partial E} \tag{C-25}$$

Using Eqs. (C-22) to (C-25) and integrating over all possible phonon wavevectors and polarizations, we obtain

$$\left(\frac{\partial u_e}{\partial t}\right)^{op.}_{REL} = \sum_{\vec{p}} \sum_{j} \left(\frac{E_{cj}(p)}{\hbar\omega_0}\right) \left(\frac{\partial f_{cj}(p)}{\partial t}\right)^{op.}_{REL}$$

$$= \left(\frac{10 D_0^2 m_c^3 \omega_0}{\rho\pi^3 N_0 \hbar^4}\right) T(T - T_0) \ln\left[1 + \exp\left(\frac{E_F - E_G}{T}\right)\right], \tag{C-26}$$

where we have normalized the temperatures and energies as described in Chapter 4.

Equation (C-26) gives the contribution of the electrons to the optical phonon-assisted relaxation. The contribution of the holes may be obtained if we make the replacements $f_{cj}(\vec{p}) \rightarrow [1 - f_h(\vec{p})]$, $E_{cj}(\vec{p}) \rightarrow -E_h(\vec{p})$, and $m_c \rightarrow m_h$ in Eq. (C-21). The result is

$$\left(\frac{\partial u_h}{\partial t}\right)^{op.}_{REL} = -\left(\frac{2 D_0^2 m_h^3 \omega_0}{\rho\pi^3 N_0 \hbar^4}\right) T(T - T_0) \ln\left[1 + \exp -\left(\frac{E_h}{T}\right)\right] \tag{C-27}$$

The calculation for acoustic phonons proceeds similarly except that the optical phonon coupling constant D_0 is replaced by λq, where λ

is the electron-acoustic phonon coupling energy. In addition, Ω_0 is replaced by $c_A q$, where c_A is the speed of sound in germanium. Retracing the steps of the derivation of Eq. (C-26) and neglecting terms proportional to $m_c c_A^2$ and $m_h c_A^2$, we find

$$\left(\frac{\partial u_e}{\partial t}\right)_{REL}^{ac} = -\left(\frac{80\lambda^2 m_c^4 \omega_0^2}{\rho\pi^3\hbar^5 N_0}\right) T^2(T - T_0) \cdot \int_0^\infty dy \frac{y}{1 + \exp\left[y - \frac{E_F - E_G}{T}\right]} \tag{C-28}$$

and

$$\left(\frac{\partial u_h}{\partial t}\right)_{REL}^{ac} = -\left(\frac{16\lambda^2 m_h^4 \omega_0^2}{\rho\pi^3\hbar^5 N_0}\right) T^2(T - T_0) \cdot \int_0^\infty dy \frac{y}{1 + \exp\left[y + \frac{E_h}{T}\right]} . \tag{C-29}$$

The total intraband relaxation of carriers due to phonon emission and absorption (both optical and acoustic) is given by the sum of the last four equations, that is,

$$\left(\frac{\partial u}{\partial t}\right)_{REL} = \left(\frac{\partial u_e}{\partial t}\right)_{REL}^{ac} + \left(\frac{\partial u_e}{\partial t}\right)_{REL}^{op} + \left(\frac{\partial u_h}{\partial t}\right)_{REL}^{ac} + \left(\frac{\partial u_h}{\partial t}\right)_{REL}^{op} . \tag{C-30}$$

Thus, we have evaluated the right-hand side of Eq. (69).

APPENDIX D

PROBE PULSE TRANSMISSION EQUATIONS

This appendix presents the final equations obtained when one performs all of the calculations outlined in Chapter 4. These equations were programmed on a digital computer and evaluated numerically to obtain the results presented in Chapter 5.

Table D1 presents the notation to be used in these equations. In addition, several basic integrals occur often enough to justify our assigning them a symbol of their own. We define

$$\rho(E_F,T) = A\int_0^\infty dy y^{1/2}\frac{1}{1+\exp\left(y-\frac{E_F-E_G}{T}\right)} \tag{D-1}$$

$$\rho(E_h,T) = B\int_0^\infty dy y^{1/2}\frac{1}{1+\exp\left(y+\frac{E_h}{T}\right)} \tag{D-2}$$

$$\sigma_e(E_F,T) = A\int_0^\infty dy y^{1/2}\left[\frac{1}{1+\exp\left(y-\frac{E_F-E_G}{T}\right)}\right]^2 \tag{D-3}$$

$$\sigma_h(E_h,T) = B\int_0^\infty dy y^{1/2}\left[\frac{1}{1+\exp\left(y+\frac{E_h}{T}\right)}\right]^2 \tag{D-4}$$

$$\nu_e(E_F,T) = A\int_0^\infty dy y^{3/2}\frac{1}{1+\exp\left(y-\frac{E_F-E_G}{T}\right)} \tag{D-5}$$

Table D1. Probe Pulse Notation

c	speed of light in vacuum
c_A	speed of acoustic phonons ($\Omega = c_A q$)
$\overline{D}$	diffusion constant
D_0	electron-optical phonon coupling constant
e	charge on an electron
E_G	indirect energy band gap [$E_G = (8E_L + 6E_X)/14$]
E_0	direct energy band gap
E_F	normalized Fermi energy for electron distribution
E_G	normalized indirect energy band gap
E_h	normalized Fermi energy for hole distribution
E_0	normalized direct energy band gap
$\hbar$	Planck's constant divided by 2π
k_B	Boltzmann's constant
L	thickness of Ge sample
m	rest mass of electron
m_c	density of states effective mass for electrons in the X and L-valleys
m_h	density of states effective mass for holes in the valence band
m_0	density of states effective mass for electrons in the Γ-valley
n	total electron (hole) density
$n(0)$	total electron (hole) density at time $t = 0$
n_0	density of electrons in Γ-valley
r	radius of the focused optical beam on the sample
R	reflectance of sample

Table D1. (Continued)

t	time
T	distribution temperature for electrons and holes
T_0	lattice temperature
$\mathcal{T}$	normalized distribution temperature for electrons and holes
$\mathcal{T}_0$	normalized lattice temperature
u	normalized distribution energy of electrons and holes
u_e	normalized distribution energy of electrons
u_h	normalized distribution energy of holes
α	total absorption coefficient
α_{DA}	direct absorption coefficient
α_{FCA}	free carrier absorption coefficient
α_{FCA}^{ac}	acoustic phonon free carrier absorption coefficient
α_{FCA}^{op}	optical phonon free carrier absorption coefficient
α_0	linear absorption coefficient
ε_∞	high frequency dielectric constant
λ	electron-acoustic phonon coupling energy
ρ	density of Ge
τ	transmission
ω_p	plasma frequency
ω_0	circular frequency of light
Ω	circular phonon frequency
Ω_0	circular frequency of optical phonons

$$\nu_h(E_h;T) = B\int_0^\infty dy y^{3/2}\frac{1}{1+\exp\left(y+\frac{E_h}{T}\right)} \tag{D-6}$$

$$\rho_0(E_F,T) = C\int_0^\infty dy y^{1/2}\frac{1}{1+\exp\left(y-\frac{E_F-E_0}{T}\right)} \tag{D-7}$$

where

$$A = \frac{5}{\pi^2 N_0}\left(\frac{2m_c\omega_0}{\hbar}\right)^{3/2}, \tag{D-8}$$

$$B = \frac{1}{\pi^2 N_0}\left(\frac{2m_c\omega_0}{\hbar}\right)^{3/2}, \tag{D-9}$$

$$C = \frac{1}{2\pi^2 N_0}\left(\frac{2m_0\omega_0}{\hbar}\right)^{3/2}. \tag{D-10}$$

In terms of the above defined integrals the total electron density in the X-valleys and L-valleys is given by

$$n = \rho T^{3/2}, \tag{D-11}$$

and the electron density in the Γ-valley by

$$n_0 = \rho_0 T^{3/2}. \tag{D-12}$$

All of the γ's and ρ's defined in Chapter 4 may be written in terms of these integrals as

$$\rho_{FE} = T^{1/2}(\rho - \sigma_e) \tag{D-13}$$

$$\gamma_{HE} = \frac{\rho - \sigma_e}{\rho - \sigma_h} \tag{D-14}$$

$$\rho_{TE} = \frac{3}{2}\rho T^{1/2} - \frac{E_F - E_G}{\sqrt{T}}(\rho - \sigma_e) \tag{D-15}$$

$$\gamma_{HT} = \frac{E_h}{T} + \left(\frac{E_F - E_G}{T}\right)\left(\frac{\rho - \sigma_e}{\rho - \sigma_h}\right) \tag{D-16}$$

$$\rho_{UT} = \frac{5}{2}T^{3/2}(\nu_e + \nu_h) + \frac{3}{2}T^{1/2}\rho\left[(2E_G - E_F) - (E_F - E_G)\cdot\left(\frac{\rho - \sigma_e}{\rho - \sigma_h}\right)\right] - \frac{1}{\sqrt{T}}E_G(E_F - E_G)(\rho - \sigma_e). \tag{D-17}$$

$$\rho_{UF} = \frac{3}{2}T^{3/2}\rho\left(1 + \frac{\rho - \sigma_e}{\rho - \sigma_h}\right) + E_G T^{1/2}(\rho - \sigma_e) \tag{D-18}$$

$$\gamma_{FE} = -\frac{E_F - E_G}{T} + \frac{3}{2}\frac{\rho}{\rho - \sigma_e} \tag{D-19}$$

$$\gamma_{FH} = \frac{E_h}{T} + \frac{3}{2}\frac{\rho}{\rho - \sigma_h} \tag{D-20}$$

$$\gamma_{UE} = \frac{5}{2}\nu_e - \frac{9\rho^2}{4(\rho - \sigma_e)} \tag{D-21}$$

$$\gamma_{UH} = \frac{5}{2}\nu_h - \frac{9\rho^2}{4(\rho - \sigma_h)} \tag{D-22}$$

$$\gamma_{RD} = \frac{1}{\sqrt{T}(\rho - \sigma_e)} \tag{D-23}$$

$$\gamma_{HE} = \frac{\rho - \sigma_e}{\rho - \sigma_h} \tag{D-24}$$

$$\gamma_{HT} = \frac{E_h}{T} + \frac{E_F - E_G}{T}\frac{\rho - \sigma_e}{\rho - \sigma_h}. \tag{D-25}$$

The probe transmission is given by the following expression:

$$\tau_{probe} = (1 - R)^2 \exp\left(- \frac{\sqrt{\varepsilon_\infty}}{c} \alpha(t) \cdot L\right) \tag{D-26}$$

where

$$\alpha(t) = \alpha_{DA}(t) + \alpha_{FCA}(t). \tag{D-27}$$

Thus, the total absorption coefficient is the sum of the direct absorption coefficient and the free carrier absorption coefficient. The free carrier absorption coefficient may further be separated into the part involving acoustic phonons and the part involving optic phonons

$$\alpha_{FCA} = \alpha_{FCA}^{op} + \alpha_{FCA}^{ac}. \tag{D-28}$$

The expressions for the various absorption coefficients are obtained by carrying out the perturbation calculations indicated in Chapter 4 [see Eqs. (72) and (73)]. The direct absorption coefficient involves a first-order calculation, and the free carrier absorption coefficients involve two second-order calculations: one for the optical phonons and one for the acoustic phonons. The calculation for the free carrier terms may be found in Matter (1975). The acoustic phonon contribution to the free carrier absorption in terms of the Fermi energies, E_F, and E_h, and the temperature T is given by

$$\alpha_{FCA}^{ac} = (SC)T \int_0^\infty dx[(\sqrt{Tx+1} + \sqrt{Tx})^5 - (\sqrt{Tx+1} - \sqrt{Tx})^5]$$

$$\cdot \left\{\left[F\left(x + \frac{E_h}{T}\right) - F\left(x + \frac{E_h+1}{T}\right)\right]\right.$$

$$+ 5\left(\frac{m_c}{m_h}\right)^{5/2}\left[F\left(x + \frac{E_G - E_F}{T}\right) - F\left(x + \frac{E_G - E_F + 1}{T}\right)\right]\Bigg\}$$

$$+ (TC)T\int_0^\infty dx[(\sqrt{Tx+1} + \sqrt{Tx})^4 - (\sqrt{Tx+1} - \sqrt{Tx})^4]$$

$$\cdot \Bigg\{\left[F\left(x + \frac{E_h}{T}\right) - F\left(x + \frac{E_h + 1}{T}\right)\right.$$

$$\left. + 5\left(\frac{m_c}{m_h}\right)^2\left[F\left(x + \frac{E_G - E_F}{T}\right) - F\left(x + \frac{E_G - E_F + 1}{T}\right)\right]\right\} \qquad \text{(D-29)}$$

where

$$SC \equiv \frac{mm_h^2\omega_0^2\lambda^2\sqrt{2m_h\hbar\omega_0}}{15\pi^3\rho c_A\hbar^5 N_0} \qquad \text{(D-30)}$$

$$TC \equiv \frac{mm_h^2\omega_0^2\lambda^2(k_B T_0)}{6\pi^3\rho c_A^2\hbar^5 N_0} \qquad \text{(D-31)}$$

and

$$F(x) \equiv \frac{1}{e^x + 1}\,. \qquad \text{(D-32)}$$

The optical phonon contribution to the free carrier absorption is

$$\alpha_{FCA}^{op} = (RC)T\int_0^\infty dx[(\sqrt{Tx+1} + \sqrt{Tx})^4 - (\sqrt{Tx+1} - \sqrt{Tx})^4]$$

$$\left(1 + \frac{T_0}{174}\right)\Bigg\{\left[F\left(x + \frac{E_h}{T}\right) - F\left(x + \frac{E_h + 1}{T}\right)\right]$$

$$+ 5\left(\frac{m_c}{m_h}\right)^2\left[F\left(x + \frac{E_G - E_F}{T}\right) - F\left(x + \frac{E_G - E_F + 1}{T}\right)\right]\Bigg\}\,. \qquad \text{(D-33)}$$

where

$$RC \equiv \frac{mD_0^2 m_h^2 \omega_0^2}{12\pi^3 N_0 \rho \hbar^4 \Omega_0} \quad . \tag{D-34}$$

The direct absorption coefficient is

$$\alpha_D = \alpha_0 \left[1 - F\left(\frac{Z_3 - E_F}{T}\right) - F\left(\frac{Z_2 + E_h}{T}\right) \right] \tag{D-35}$$

where α_0 is the experimental linear absorption coefficient at the temperature T, and

$$Z_2 \equiv \left(\frac{m_0}{m_0 + m_h}\right) (1 - E_0) \tag{D-36}$$

$$Z_3 = E_0 + \frac{m_h}{m_0 + m_h} (1 - E_0). \tag{D-37}$$

Knowledge of the time behavior of the absorption coefficients requires a knowledge of the time behavior of the Fermi energies, E_F and E_h, and the temperature, T. The time rate of change of E_F, E_h, and T is given by Eqs. (68), (69), and (70) of Chapter 4. Rewriting these equations

$$\frac{dE_F}{dt} = \frac{\gamma_{FE}}{\gamma_{UE} + \gamma_{UH}} (\Gamma_E + \Gamma_H) - \gamma_{RD} (n\Gamma_{R2} + n_0\Gamma_{R1} + \Gamma_D) \tag{D-38}$$

$$\frac{dT}{dt} = - \frac{\Gamma_E + \Gamma_H}{\gamma_{UE} + \gamma_{UH}} \tag{D-39}$$

and

$$\frac{dE_h}{dt} = - \frac{\gamma_{HT} + \gamma_{HE}\gamma_{FE}}{\gamma_{UE} + \gamma_{UH}} (\Gamma_E + \Gamma_H) + \gamma_{HE}\gamma_{RD} (n\Gamma_{R2} + n_0\Gamma_{R1} + \Gamma_D) \tag{D-40}$$

where Γ_E represents the change in total carrier energy due to the phonon-assisted intravalley decay of the electrons and Γ_H represents the change due to the intravalley decay of the holes. Both optical and acoustic phonons contribute to Γ_E and Γ_H. In terms of Eq. (69), we have defined

$$\Gamma_E \equiv -\left(\frac{du_e}{dt}\right)_{REL} \tag{D-41}$$

and

$$\Gamma_H \equiv -\left(\frac{du_h}{dt}\right)_{REL}. \tag{D-42}$$

The indicated perturbation calculations are performed in Appendix C; the results are

$$\Gamma_E = GT(T - T_0)\ \ln\left[1 + \exp\left(\frac{E_F - E_G}{T}\right)\right] + DT^2(T - T_0) \cdot \int_0^\infty dy\ \ln\left[1 + \exp\left(-y + \frac{E_F - E_G}{T}\right)\right] \tag{D-43}$$

$$\Gamma_H = ET(T - T_0)\ \ln\left[1 + \exp\left(\frac{-E_h}{T}\right)\right] + FT^2(T - T_0) \int_0^\infty dy\ \ln\left[1 + \exp\left(-y - \frac{E_h}{T}\right)\right] \tag{D-44}$$

where

$$G \equiv \frac{10 D_0^2 m_c^3 \omega_0}{\rho \pi^3 \hbar^4 N_0}, \tag{D-45}$$

$$D \equiv \frac{80 \lambda^2 m_c^4 \omega_0^2}{\rho \pi^3 \hbar^5 N_0} \tag{D-46}$$

$$E \equiv \frac{2 D_0^2 m_h^3 \omega_0}{\rho \pi^3 N_0 \hbar^4}, \tag{D-47}$$

and

$$F \equiv \frac{16\lambda^2 m_h^4 \omega_0}{\rho\pi^3\hbar^5 N_0} . \tag{D-48}$$

Comparison of Eq. (D-38) and Eq. (70) shows that we have also separated the decrease in electron density due to the "other" terms into the following:

$$-\left(\frac{dn}{dt}\right)_{other} = n\Gamma_{R2} + n_0\Gamma_{R1} + \Gamma_D, \tag{D-49}$$

where Γ_{R2} represents the indirect plasma recombination rate; Γ_{R1}, the direct plasma plus radiative recombination rate; and Γ_D, the number of carriers diffusing out of the interaction volume.

Perturbation theory gives

$$\Gamma_{R1} = 10^9 + 6 \times 10^{14}\left(\frac{\hbar\omega_p \Delta}{E_0^2}\right) \cdot \left[\frac{E_0}{\left[(\hbar\omega_p - E_0) + \frac{\Delta^2}{4}\right]^{1/2} - (\hbar\omega_p - E_0)}\right]^{1/2} \tag{D-50}$$

and

$$\Gamma_{R2} = 10^{11} \cdot \left(\frac{\hbar\omega_p}{E_0}\right)\left(1 + \frac{T_0}{174}\right) \cdot \left[\frac{\Delta^2}{(E_0 - E_G)\left\{\left[(\hbar\omega_p - E_G)^2 - \frac{\Delta^2}{4}\right]^{1/2} - (\hbar\omega_p - E_G)\right\}}\right]^{1/2} \tag{D-51}$$

where

$$\Delta \equiv (\Gamma_E + \Gamma_H)\hbar \quad \text{and} \quad \hbar\omega_p \equiv (\hbar\omega_0)\sqrt{n}\left(\frac{m}{m_c} + \frac{m}{m_h}\right)^{1/2} . \tag{D-52}$$

The quantity Δ represents the coupling width for the plasmon recombinations.

The Boltzmann equation can be solved to obtain the diffusion term

$$\Gamma_D = \frac{r^2 D(t) n(0)}{4\left[\int_0^\infty dt' D(t')\right]^2} \exp\left[-\int_0^\infty \Gamma_{R2}(t')dt' - \frac{r^2}{4\int_0^\infty dt' D(t')}\right], \tag{D-53}$$

where

$$D(t) = \bar{D}T, \tag{D-54}$$

and

$$\bar{D} = \frac{2\hbar\omega_0 \tau_{collision}}{m_c + m_h} \quad . \tag{D-55}$$

The particle-particle collision time, $\tau_{collision}$, is estimated from perturbation calculations to be approximately 10^{-13} sec. This gives a diffusion constant, $\bar{D}$, on the order of 10^3 cm^2 sec^{-1}.

The equations presented above were programmed on a digital computer and numerically integrated. The results of this integration are presented in Chapter 5.

A final comment should be made concerning the numerical values of the constants used in these equations. The energy gaps and effective masses for germanium are given, and referenced in Chapter 4 for temperatures of 77 K and 297 K. The germanium sample thickness was measured to be 5.5 μm. Values of 5.4×10^5 cm/sec and 0.03 eV are taken for c_A and $\hbar\Omega_0$, respectively (Brockhouse and Iyengar, 1958). The density of germanium is taken as 5.3 g/cm^3 (Neuberger, 1971). The linear

absorption coefficient α_0 has a value of 1.46×10^4 cm^{-1} at room temperature and 1.11×10^4 cm^{-1} at 77 K (Dash and Newman, 1955). The acoustic phonon-electron coupling energy, λ, is taken as 1.33×10^{-11} ergs; the optical phonon-electron coupling constant, D_0, has a value in the range 2 to 3×10^{-3} erg/cm (Meyer, 1958).

REFERENCES

Alfano, R. R., and S. L. Shapiro, "Ultrafast phenomena," Physics Today p. 30 (July 1975).

Auston, D. H., and C. V. Shank, "Picosecond ellipsometry of transient electron-hole plasmas in germanium," Phys. Rev. Letters 32:1120 (1974).

Brockhouse, B. N., and P. K. Iyengar, "Normal modes of germanium by neutron spectrometry," Phys. Rev. 111:747 (1958).

Dash, W. C., and R. Newman, "Intrinsic optical absorption in single-crystal germanium and silicon at 77 K and 300 K," Phys. Rev. 99:1151 (1955).

Davydov, A. S., Quantum Mechanics (Ann Arbor, Michigan, NEO Press, 1966).

Graeme, J., "Peak detector advances increase measurement accuracy, bandwidth," EDN, p. 73 (5 Sept. 1974).

Kennedy, C. J., J. C. Matter, A. L. Smirl, H. Weichel, F. A. Hopf, and S. V. Pappu, "Nonlinear absorption and ultrashort carrier relaxation times in germanium under irradiation by picosecond pulses," Phys. Rev. Letters 32:419 (1974).

Kittel, C., Quantum Theory of Solids (New York, John Wiley and Sons, 1963).

Lax, M., and J. J. Hopfield, "Selection rules connecting different points in the Brillouin zone," Phys. Rev. 124:115 (1961).

Matter, J. C., "Interaction of picosecond pulses with intrinsic germanium," Ph.D. Dissertation, University of Arizona (1975).

Meyer, H. J. G., "Infrared absorption by conduction electrons in germanium," Phys. Rev. 112:298 (1958).

Neuberger, M., "Group IV semiconductor materials," Handbook of Electronic Materials, Vol. 5 (New York, Plenum Press, 1971).

Schmit, J. L., and E. L. Stelzer, "Temperature and alloy compositional dependences of the energy gap of $Hg_{1-x}Cd_xTe$," J. Appl. Phys. 40:4865 (1969).

Scott, W., and R. J. Hager, "Anomalous electrical properties of p-type HgCdTe," J. Appl. Phys. 42:803 (1971).

Shank, C. V., and D. H. Auston, "Parametric coupling in an optically excited plasma in Ge," Phys. Rev. Letters 34:479 (1975).

Shelton, J. W., and J. A. Armstrong, "Measurement of the relaxation time of the Eastman 9740 bleachable dye," IEEE JQE QE-3:696 (1967).

Shih, H., M. Scully, W. H. Louisell, and W. B. McKnight, "Interacting beams in a resonant medium," Appl. Opt. 12:2198 (1973).

Smirl, A. L., J. C. Matter, A. Elci, and M. O. Scully, "Ultrafast relaxation of optically excited nonequilibrium electron-hole distributions in germanium," Opt. Comm., accepted for publication (1975).

Smith, P. W., M. A. Duguay, and E. P. Ippen, Progress in Quantum Electronics, Vol. 3 (New York, Pergamon Press, 1974).

Von der Linde, D., "Mode-locked lasers and ultrashort light pulses," Appl. Phys. 2:281 (1973).

Von der Linde, D., O. Bernechker, and A. Laubereau, "A fast electro-optic shutter for the selection of single picosecond laser pulses," Opt. Comm. 2:215 (1970).

Weichel, Hugo, "Reliable generation of picosecond optical pulses and their application to the measurement of intraband relaxation times in semiconductors," Ph.D. Dissertation, University of Arizona (1972).